UNIVERSITY OF LONDON THESIS

Degree PhD Year 2005 Name of Author LIGHTWOOD, M. S.

Dijet Production and Multiscale QCD at HERA.

Matthew S. Lightwood

University College London

2004

Thesis submitted to the University College London
in accordance with the requirements of the degree of
Doctor of Philosophy in the Faculty of Science.

ProQuest LLC
789 East Eisenhower Parkway
P.O. Box 1346
Ann Arbor, MI 48106-1346

Abstract

This thesis describes the analysis of dijet production in photoproduction and DIS, using the ZEUS detector at HERA. At ZEUS, positrons and protons were collided with a centre of mass energy of $\sqrt{s} =$ 300 GeV during the 1996-1997 running period and $\sqrt{s} =$ 318 GeV thereafter. Dijet production is studied for the all-flavours case and for the case when a charm quark is demanded.
In the all-flavours analysis, the dependence of dijet production on the virtuality of the exchanged photon, Q^2, was studied by measuring dijet cross sections in the range $0.0 < Q^2 < 2000$ GeV^2, using data from the 1996-1997 running period corresponding to an integrated luminosity of 38.6 pb^{-1}. Dijet cross sections were measured in the photon-proton centre-of-mass frame for jets with transverse energy $E_{\mathrm{T}}^{\mathrm{jet}} > 7.5$ and 6.5 GeV and pseudorapidity in the range $-3.0 < \eta^{\mathrm{jet}} < 0.0$. The variable x_γ^{OBS}, a measure of the fractional photon momentum entering the hard process, was used to enhance the sensitivity of the measurements to the photon structure. The Q^2 dependence of the ratio of low to high x_γ^{OBS} events was measured. Next-to-leading-order QCD predictions were found to generally underestimate the low x_γ^{OBS} contribution relative to that of high x_γ^{OBS}. Leading-logarithmic parton-shower Monte-Carlo predictions which use a partonic structure for the photon, falling smoothly with increasing Q^2 provide a qualitative description of the data.
The all-flavours dijet analysis was repeated with the demand that a $D^*(2010)$ meson was identified in the decay channel $D^* \to D^0\pi_s \to (K\pi)\pi_s$ with $p_{\mathrm{T}}(D^*) >$ 3.0 GeV and $|\eta(D^*)| < 1.5$. The charm data were collected from the running period 1996-2000, corresponding to an integrated luminosity of 120.4 pb^{-1}, and cover the range of photon virtualities $0.0 < Q^2 < 5000$ GeV^2. The measurements were compared to next-to-leading-order QCD predictions which were generally found to give a good description of the data. Leading order pQCD models with parton shower simulation which include a parameterisation of the virtual photon were found to give a good description of the DIS data. Such models were found to be consistent with the photoproduction data only when the non-perturbative vector meson like component of the resolved photon is removed. When no parameterisation of the hadronic component of the virtual photon was used DGLAP evolution was found to lie below the data, and CCFM evolution generally closer to the data.

To My Family and Friends

Acknowledgements

In the past four years I have been extremely fortunate to work with an exceptional group of people, without whom this thesis would not have been possible. Foremost of those people is my supervisor Jon Butterworth, who I would like to thank for much intellectual input, pointing me in interesting and relevant directions and always fighting my corner. A close second must be given to Richard Hall-Wilton for day to day advice over the past three years, for your considerable knowledge of heavy quark production, and for all the work on the analysis, as well as proof reading this thesis. Also I must thank Ben West, for getting me started when I knew nothing and for teaching me the basics. Dorian Kcira I gratefully thank for all the hard work on the paper and allowing me to collaborate on it. For advice given in and out of heavy flavour meetings I thank Matthew Wing. For sharing his knowledge of QCD, even when it wasn't asked for, I must thank Mark Sutton. I acknowledge Prof. Tegid Jones for much advice and many humorous asides. I also thank my office mate Chris Targett-Adams who endured my writing up period nobly. Many people on the ZEUS collaboration have helped me in smaller ways, if your name is not mentioned here then I apologise and thank you.
Personally I have been very fortunate to retain close friends and meet many new wonderful people along the dark road to doctorhood. My girlfriend Natascha Geberin deserves special thanks for unwavering love and support over the past two years, and just for being my north, south, east and west even when I lost the compass. My long standing partners in crime and best friends "the boys" Chris Gallagher, Damian Green and Paul Sewell I thank for much needed debauchery and good old fashioned laddish humour often fuelled by dangerous amounts and types of alcohol, and for making my life fun. "The girls", Karen "kaz" Tromans, Gillian Franklin, Claire Benbow and Amanda Green I thank for your friendship and loyalty over the years. I thank my big brother Dan for being more of a best mate than a brother, and for the many laughs. From the Manchester years I acknowledge Jay Cox, Jon Lovell, Rich Thompson and Paul Pritchett-Brown for much insanity. The Leicester connection taking the form of Sam Leighton (and Guinness the dog), Lynn Catterall and John Harrison I thank for their friendship and hospitality over many interesting weekends. In Hamburg I wish to thank Peter for many interesting conversations over a pint and the "Finnighans crowd" most notably Damon, Sarah Menzies, Sonia Elmquist and Emma Quirke for introducing me so intensively to the pubs and clubs of HH city in my first four months, and for making my early days as an ex-pat so much fun. Also thanks very much to Andy McKinna and the Particle Physics and Astronomy Research Council (PPARC) who funded this research.
This work would simply not have been possible without the continual love and support of my parents whose significance in producing this thesis warrants a separate paragraph.

Contents

List of Figures

List of Tables

Part I

Introduction

Chapter 1

HERA and the ZEUS Detector

1.1 HERA

HERA, the Hadron Elektron Ring Anlage shown in figure 1.1, is the world's only electron-proton collider. Building of the ring began at the DESY (Deutsches Elektronen-SYnchrotron) laboratory in Hamburg, Germany in 1984 and data taking started in 1992. It was envisaged that the data would primarily give an insight into the fundamental structure of the proton. Bunches of electrons[1] and protons are stored in two separate 6.3km circumference rings, lying 10-30m underground. The energy of these particles separates the lifetime of HERA into two distinct running periods. The first between 1992-1997, when the electrons had an energy of 27.5 GeV and the protons 820 GeV with a centre-of-mass energy upon collision of $\sqrt{s} \sim 300$ GeV, and the second between 1998-2000 when the proton beam energy was increased to 920 GeV with the electron energy remaining unchanged, giving $\sqrt{s} \sim 318$ GeV. The data analysed and presented in this thesis encompass data from both periods, specifically between 1996-2000.
Achieving these high centre of mass energies requires a complicated chain of pre-acceleration and injection. Initially proton injection is performed by accelerating H^- ions to 50 MeV using a linear accelerator. The electrons are then stripped off, yielding protons which are passed to the DESY III proton synchrotron, where they are bunched into 11 bunches separated by 96ns and accelerated to 7.5 GeV. From here they are passed to the PETRA accelerator, where they are accelerated to 40 GeV before finally being injected into the HERA proton machine. Final

[1] Hereafter electron and positron are used interchangeably to describe the lepton beam and e^-p and e^+p are assumed to give identical results.

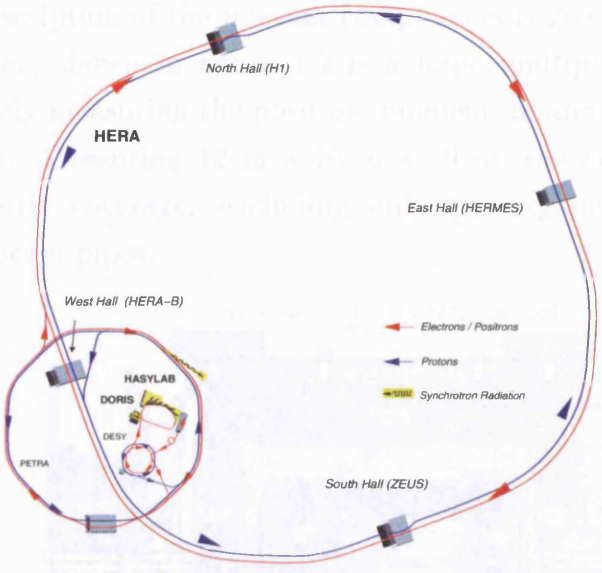

Figure 1.1: *The HERA ep collider and its experiments, shown also is the smaller pre-acceleration ring, PETRA.*

acceleration of the beam to 820(920) GeV is performed when HERA contains 180 bunches of protons, the full capacity of the ring.

Lepton beam production is initiated in LINACS's I and II which accelerate the beam to 220 and 450 MeV respectively. The beam energy is then stepped up to 7.5 GeV in the DESY II synchrotron, and injected in bunches into the PETRA II storage ring, where they are accelerated to 14 GeV with the same bunch separation as the protons. The lepton beam is injected into the HERA lepton machine at a slightly reduced energy of 12 GeV, where they are ramped to 27.52 GeV. At four interaction positions lepton bunches can be steered so that they collide with the proton beam at zero crossing angle. In reality this only happens at two of the four positions.

At each of the four interaction positions detector experiments monitor and record the aftermath of these collisions. Two general purpose physics detectors, ZEUS and H1, are operational on the HERA ring, located in the south and north halls respectively. A fixed target experiment, HERMES is located in the east hall, and is used to study spin physics and the west hall houses the HERA-B experiment. The data presented in this thesis were all collected using the ZEUS detector.

1.2 The ZEUS Detector

A more detailed description of the ZEUS detector can be found elsewhere [1], however a brief description of the relevant components is given here.
The ZEUS detector, shown in figure 1.2 is a large multipurpose experiment, capable of accurately measuring the position, momentum and energy of particles passing through it. Measuring 12 m × 10 m × 19 m, the detector has almost hermetic calorimetric coverage, excluding only the regions surrounding the forward and rear beam pipes.

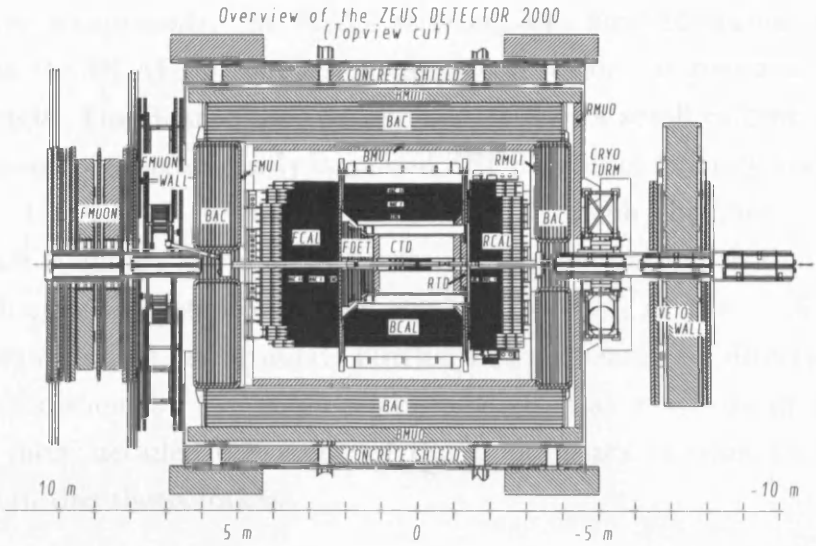

Figure 1.2: CAD Drawing of the ZEUS detector in cross section from above.

The ZEUS coordinate system is a right-handed Cartesian system with its origin at the nominal interaction point. The z-axis of the system points in the direction of the proton beam, with the x-axis towards the centre of HERA. The proton direction (+z) is referred to as the forward direction, with the polar angle, θ, defined relative to it such that the proton beam travels in the direction defined by $\theta = 0$ and the lepton beam in that defined by $\theta = \pi$. Azimuthal angles, ϕ, are measured with respect to the x-axis.
In practice polar angles are measured in terms of pseudorapidity, $\eta = -\ln(\tan\theta/2)$, where the lepton now travels in the direction of $\eta = -\infty$, and the proton $\eta = +\infty$. Defining polar angles in this way has the advantage that boosts along the z-axis only modify η by an additive constant, such that differences in η are longitudinally invariant. The asymmetric energies of colliding particles in ep interactions

means that many frames of interest require such a boost, making η a convenient choice.

Moving radially outward from the interaction point the innermost operational component during the running period 1996-2000 was the central tracking detector (CTD). Tracking in the forward and rear regions is performed with the FTD, and RTD, lying at each end of the CTD. In addition to these the Small angle Rear Tracking Detector (SRTD) gives improved positron recognition at low scattering angles. Calorimetry is performed with a combination of a high resolution Uranium CALorimeter (UCAL) and a Backing CALorimeter. The UCAL is in fact constructed of three components, the FCAL covering the forward region, the RCAL the rear and the BCAL encompassing the barrel region, to give near 4π coverage in solid angle. The Beam Pipe Calorimeter (BPC), A small calorimeter installed near the beam pipe significantly increased ZEUS's ability to study events at low x and Q^2. Outside of the UCAL lie a series of muon chambers. At $z = -3.15$ m the C5 counter monitors synchrotron radiation and bunch timing, this information along with that provided by the VETOWALL at $z = -7.5$ m, is used to reject beam related background. Further down stream ($-z$ direction) the luminosity is monitored by two small lead scintillators at $z = -34$ m and $z = -104$ m. A more detailed discussion of the components relevant to the analyses presented in this thesis follows.

1.3 The Central Tracking Detector

The Central Tracking Detector (CTD) [2] is a cylindrical wire drift chamber, which tracks the paths and measures the momenta of charged particles passing through it to a high degree of precision. It operates in a magnetic field of 1.43 T supplied by a superconducting solenoid. A gas mixture of argon($\sim$ 85%), ethane ($\sim$ 10%) and carbon dioxide ($\sim$ 5%) acts as the ionisation medium. A total of 24192 wires constitute the CTD, 4608 of which are sense wires, with the remaining acting as field and ground wires, making the electric field between sense wires uniform.

Figure 1.3 shows how these wires are organised firstly into cells, each containing 8 sense wires orientated at 45° to the radial axis, and then into nine concentric superlayers. For readout purposes the superlayers are further separated diametrically into 16 sectors.

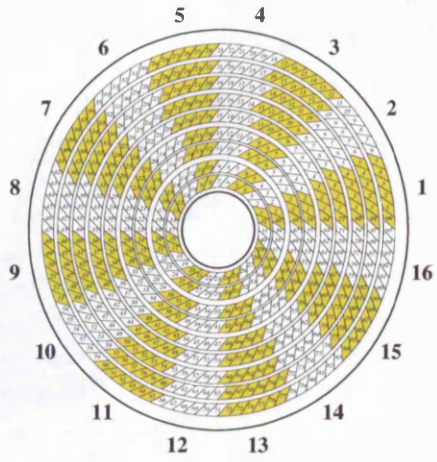

Figure 1.3: *x-y view of the CTD showing the layout of the wires in the 9 superlayers of the detector.*

Sense wires are positioned parallel to the beam axis in odd numbered superlayers, and are referred to as the axial layers. Sense wires in the remaining layers are orientated at a small angle ($\pm 5°$) to the z axis, and are referred to as stereo layers. The stereo layers enable reconstruction of the z position of a track with a resolution of ± 2 mm, with the nominal resolution of a full length track of 180 μm in $r - \phi$. The total polar angle acceptance region of the CTD is $11° < \theta < 168°$, however this coverage is slightly reduced ($\pm 7°$) by the common requirement that tracks pass through three superlayers or more to enhance track quality.
As a charged particle moves through the chamber it ionises the gas along its path, leaving electrons and positively charged ions in its wake. As each cell is orientated at 45° to the radial axis, and the Lorentz angle of the drift field in each cell is also at 45°, the drift electrons follow radially transverse paths through the cells, as illustrated in figure 1.4. This fact helps resolve the ambiguity between whether an electron came from the right or left of the sense wire.
The CTD measures the momentum of tracks passing through it with a resolution of $\sigma(p_T)/p_T = 0.0058 p_T \oplus 0.0065 \oplus 0.0014/p_T$ [3].

1.4 The Uranium Scintillator Calorimeter

The ZEUS calorimeter (CAL) [4] is a high resolution compensating calorimeter essential for the studies of jet production presented in this thesis. Hadronic showering differs significantly from electromagnetic showering, as is shown in the schematic diagram, figure 1.5. This is due to the fact that electromagnetic

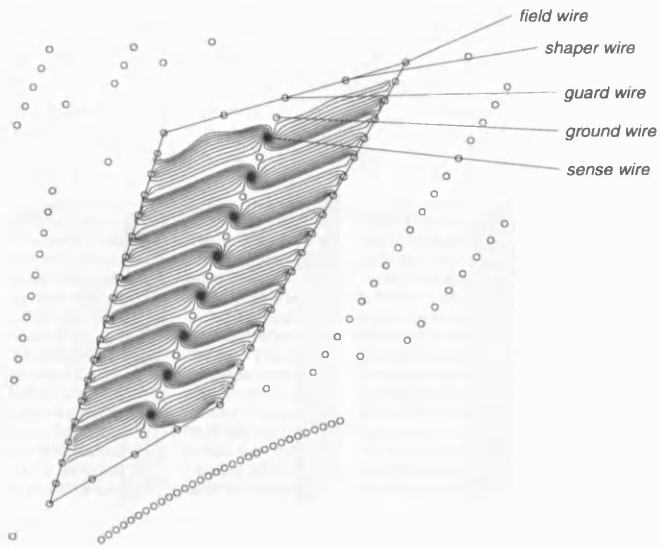

Figure 1.4: *CTD drift cell showing the complex arrangement of wires and their functions.*

showers produce more photons than a hadronic shower of the same energy. The construction of the calorimeter is such that it compensates for these differences allowing accurate reconstruction of the energy of both hadronic and electromagnetic matter passing through it. This is achieved by using alternate layers of an absorber, in this case 3.3mm plates of depleted uranium (DU), and polystyrene scintillator of thickness 2.6mm. The uranium absorbs neutrons from hadron showering, and emits photons, which can be amplified by photomultipliers. The thickness of the DU layer is fixed such that equal energy hadronic and electromagnetic showers give an approximately equal response at the photomultipliers.

The calorimeter is composed of many of these alternating layers, separated into 20 cm $\times$ 20 cm towers, arranged vertically in the case of the FCAL and RCAL and radially in the case of the BCAL. Figure 1.6 shows how each tower is segmented into an electromagnetic calorimeter (EMC) and a hadronic calorimeter (HAC). The EMC section consists of four 5 cm $\times$ 20 cm cells in the FCAL and BCAL, and as two 10 cm $\times$ 20 cm cells in the RCAL, enough to fully contain most purely electromagnetic showers. The EMC makes up the inner section of a tower, with in the FCAL and BCAL, two hadronic sections (HAC1 and HAC2) lying directly behind, towards the outside of the detector, and in the RCAL one HAC. This difference is due to the absorption requirements in the forward and rear directions, due to the asymmetric electron and proton beam energies.

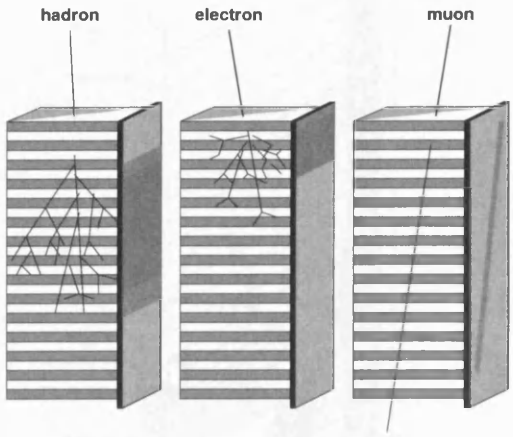

Figure 1.5: *Typical showering characteristics of different types of matter in the ZEUS calorimeter.*

The relative energy resolution of the calorimeter is $\frac{0.18}{\sqrt{E}} \oplus 0.01$ for electrons and $\frac{0.35}{\sqrt{E}} \oplus 0.02$ for hadrons. In total the CAL provides 99.7% coverage of the total solid angle, facilitating complete containment of jets and particles produced in collisions at HERA.

1.4.1 Presampler

A particle moving from the interaction region to the CAL encounters dead material, for instance the CTD end plates and superconducting solenoid. This material reduces the energy of the particle before it is measured by the CAL. The Presampler (PRES) [5], a thin segmented layer of scintillator on the inner face of the CAL, acts as a particle multiplicity counter. As the particle may have prematurely showered in any dead material, the multiplicity can be used to estimate the energy lost, and hence correct for it on an event by event basis.

1.4.2 Small Angle Rear Tracking Detector

The Small angle Rear Tracking Detector (SRTD) [6], is designed to measure electrons scattered at small angles with a better energy and position resolution, than is possible with RCAL. Positioned on the face of the RCAL, surrounding the beam pipe, the SRTD has polar angle coverage of $162° < \theta < 176°$, encompassing the region where most low Q^2 and DIS electrons are scattered. The SRTD consists

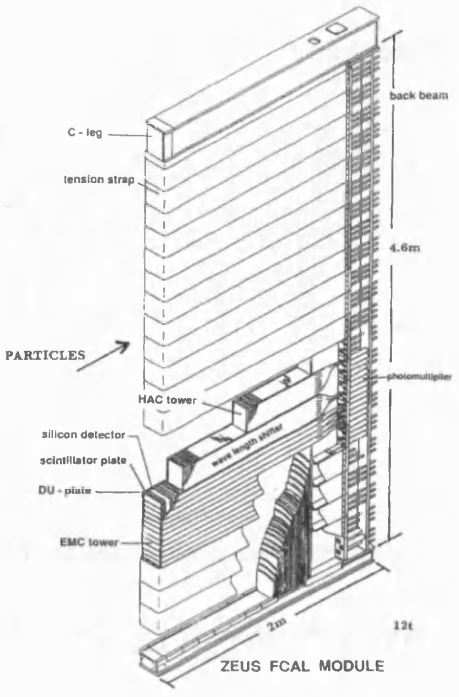

Figure 1.6: *Structure of an FCAL module.*

of four quadrants of double layered silicon giving a position resolution of ~ 3 mm, compared to 1cm for the calorimeter. By analogy with the PRES, the SRTD can be used to correct the electron energy for losses due to showering in the inactive material in front of the RTD.

1.5 Luminosity Monitoring at ZEUS

In any cross section measurement an accurate determination of the integrated luminosity is essential. The ZEUS luminosity monitor [7] uses the rate of the Bremsstrahlung process,

$$ep \rightarrow e'\gamma p$$

which has a known and relatively high cross section (~ 15 mb), to measure the luminosity. In this process the photon is emitted at a very low angle to the incident electron. By tagging the photon the rate can be determined. In practice this is performed by the LUMI-γ detector situated close to the beam pipe between $z = -104$ m and $z = -107$ m, as shown in 1.7. The detector is a lead-scintillator sandwich calorimeter, with energy resolution $\sigma(E)/E = 0.18\sqrt{E}$, and is capable of measuring the luminosity to an accuracy of $1.1\% - 2.25\%$.

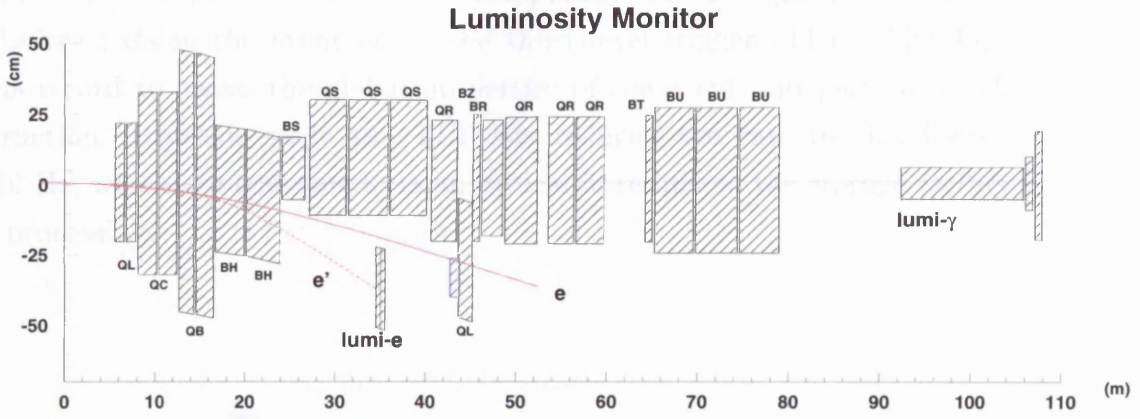

Figure 1.7: *The ZEUS luminosity monitor shown with the beam magnets near the interaction region.*

1.6 The ZEUS Trigger System

With a bunch crossing rate of $\sim$ 10 MHz, and an interaction rate of $\sim$ 10 – 100 kHz, consisting mainly of proton beam gas, data acquisition (DAQ) at HERA presents a significant challenge. To reduce this high rate to the few Hz of interesting physics events, ZEUS employs a three level trigger and DAQ system [8], shown schematically in figure 1.8, to select probable physics events in the time available.

The rate is initially reduced to $\sim$ 1 kHz at the First Level Trigger (FLT), a set of programmable hardware triggers. The time available to the FLT between bunch crossings is not long enough for a decision to be made, as such the data are pipelined until a trigger decision is made $\sim 2\ \mu s$ later. Each component used at the FLT has its own trigger. The decision from each is passed to the Global First Level Trigger (GFLT) separately, and a final accept or reject decision is made within 4.4 μs.

Events passing at the FLT are passed to the Second Level Trigger (SLT), a software trigger operating on a transputer network. More stringent requirements are made on the events than at the FLT, with the aim of further rejecting background events. The SLT decisions from the individual components (CTD-SLT,CAL-SLT), used are passed to the Global Second Level Trigger (GSLT) where a final decision is made on the event, at which point the rate has been further reduced by approximately a factor of 10, giving an output rate < 100 Hz.

The EVB compiles the data from each component into a single record of the event, before passing the event on to the third level trigger (TLT). The TLT uses this record to assess the global properties of the event and perform a full reconstruction. By this stage the TLT has reduced the rate to the desired $\sim 1 - 10$ Hz, which are transfered via an optical fibre link to the storage facility for full processing.

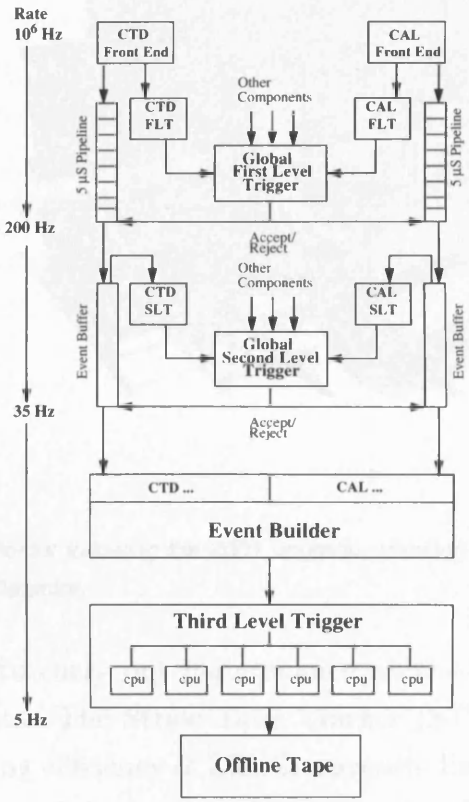

Figure 1.8: *Schematic diagram of the ZEUS Trigger and data acquisition system.*

1.7 The HERA Upgrade

The annual integrated luminosity of HERA has steadily increased from 33 nb^{-1} in 1992, to 67 pb^{-1} in 2000. Whilst this luminosity has given insights into many areas of particle physics, detailed studies of heavy flavour production are as yet

restricted by low statistics and poor tagging of heavy meson decays. Motivated by this and other factors the HERA ring and its experiments were shutdown at the end of 2000, to undergo major upgrades [9].
HERA's goal was to reduce the cross sectional area of the beams by a factor four in the interaction region , in order to deliver an integrated luminosity of 1 fb^{-1} by 2005. This was achieved by installing new superconducting magnets close to the IP, moving the focus of the beams into the centre of the detectors.

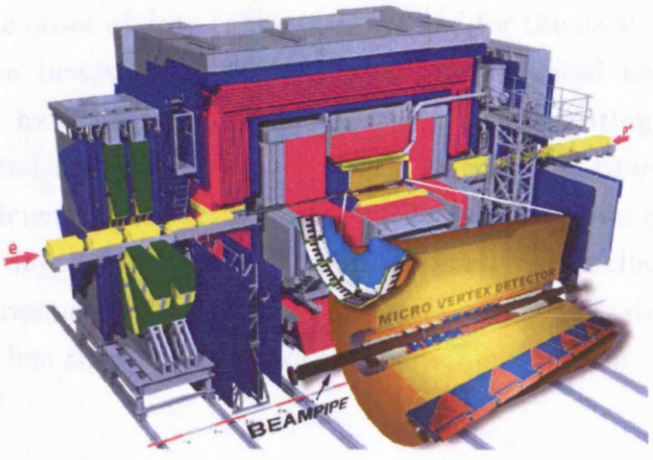

Figure 1.9: *The ZEUS detector following the 2001 upgrade, showing a blowup of the central region containing the Micro-Vertex Detector.*

ZEUS used this time to carry out maintenance on the detector, and to install several new components. The Straw Tube Tracker (STT) [10] was installed to improve the track finding efficiency of ZEUS, currently limited by high occupancy in the forward region and limited resolution in the FTD. The Micro-Vertex Detector (MVD) [11], figure 1.9, a silicon strip detector, was installed at the heart of the detector to improve the tagging of heavy meson decays. Such tagging is currently limited by the spatial resolution and angular coverage of the CTD. The trajectories of charged particles moving through the MVD can be measured with a resolution of $10\mu m$, allowing the measurement of heavy quark production with minimal background.
After the upgrade average rates of up to $\approx$ 400 Hz are expected at the GFLT at peak luminosity, compared to $\approx$ 150 Hz in the year 2000 [12], at the GSLT

rates of $\approx$ 120 Hz are expected compared to $\approx$ 50 Hz in HERA I. Dealing with these high rates, and the need to improve heavy flavour triggering motivated the development of an improved tracking trigger. The Global Tracking Trigger (GTT) aims to supplement the CTD-SLT [13] by the addition of a PC farm with improved software and hardware architecture. The GTT also utilises information from the MVD, giving improved track and primary vertex resolution. Early studies of the GTT are promising and suggest many advantages over the CTD-SLT.
High rates of synchrotron radiation in the ZEUS detector and other technical problems, delayed the onset of data taking in 2002 and for the early part of 2003. These problems were investigated and solutions implemented and somewhat improved conditions have been achieved. At the time of writing HERA had delivered an integrated luminosity of 34.8 pb^{-1}. During this time ZEUS took data with a 45 % efficiency, gating 15.62 pb^{-1} of data. Efforts are continuing to understand the new data which is not of sufficient quality to include in physics analyses. Results presented in this thesis therefore encompass data from the periods 1996-2000, when the above components were unavailable.

Chapter 2

QCD and ep Interactions

In QED the electric charge of an electron is reduced when observed from a distance because of screening. This phenomena arises as a consequence of the fact that a flux of virtual photons is constantly emitted from the electron which can fluctuate into e^+e^- pairs. The electron is then effectively surrounded by a cloud of e^+e^- pairs, screening its charge at large distances. As the electron is probed at smaller scales the effect is reduced and the electromagnetic coupling constant, α, becomes larger.

In hadronic interactions an analogous situation exists, with partons carrying an additional "colour charge", described by Quantum Chromo-Dynamics (QCD), a non-Abelian gauge theory of the SU(3) symmetry group. In QCD the strong nuclear force is propagated by a chargeless, massless, spin 1 particle called the gluon. Unlike photons, gluons are able to couple to one another, and therefore $g \rightarrow gg$ pair production is possible. The process $g \rightarrow gg$ is typified by a stronger coupling, a stronger colour field and a field which varies less rapidly than that for the process $g \rightarrow q\bar{q}$ and as such glue-glue pair production dominates. At small momentum scales (large distances) the strong nuclear coupling constant, α_s is observed to be large, and to reduce with increasing momentum scale due to the anti-screening effect of the gluon cloud. This running of the coupling constant, α_s, means that at large momentum scales the parton is effectively observed in isolation, an effect known as asymptotic freedom.

At small momentum scales the partons interact strongly, and are bound together into colour neutral states called hadrons. Without a sufficiently hard scale, α_s is large and a perturbative calculation in terms of weakly interacting partons is no longer possible. To compare experimental data to such perturbative calculations then requires the probing of hadrons at a sufficiently hard scale, when individual partons within the hadron are quasi-free.

2.1 Electron Proton Scattering

At HERA the structure of the proton is studied in deep inelastic lepton-hadron scattering. This process, mediated by the exchange of either a $W^{\pm}$ or a Z^0 in the case of weak interactions, or a photon (γ) in the case of electromagnetic interactions, is shown in figure 2.1. These interactions are commonly labelled neutral current (NC) when the exchanged boson is an electrically neutral γ or Z^0, and charged current (CC) when a $W^{\pm}$ is exchanged.

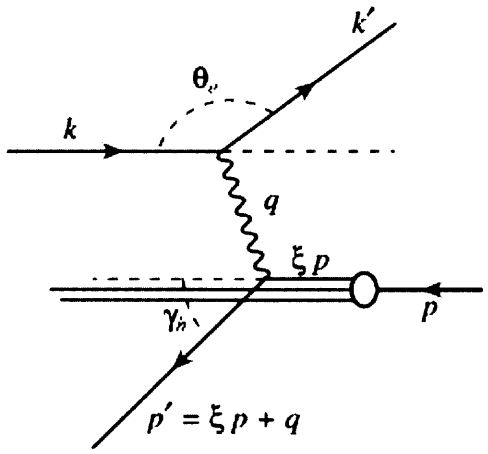

Figure 2.1: *The kinematic variables of deep inelastic ep scattering at HERA.*

The kinematics of the above process can be completely described by three variables. The negative of the four momentum transfer squared, Q^2, the Bjorken scaling variable x, and the amount of energy transferred between the hadronic and leptonic systems y, given by

$$Q^2 = -q^2 = -(k - k')^2 \tag{2.1}$$

$$x = \frac{Q^2}{2p.q} \tag{2.2}$$

$$y = \frac{p.q}{p.k}, \tag{2.3}$$

where $Q^2 \geq 0$ and has units GeV^2,and x and y are positive dimensionless quantities satisfying $x \leq 1$ and $y \leq 1$. The invariant mass, s, of such a colliding

system is given by

$$s = (k+p)^2 \approx 2p.k = \frac{Q^2}{xy}, \tag{2.4}$$

such that at fixed s only two of the three invariant quantities, Q^2, x and y are independent.

2.1.1 Proton Structure

In leading order perturbative QCD the NC and CC scattering cross sections in DIS can be described in terms of "structure functions", parameterising the structure of the proton resolved by the incoming virtual boson. For the NC interaction $e^{\pm}p \to e^{\pm}X$, the double differential cross section can be expressed as

$$\frac{d^2\sigma^{ep}}{dxdQ^2} = \frac{4\pi\alpha^2}{xQ^4}\left[\frac{y^2}{2}2xF_1 + (1-y)F_2 \mp \left(y - \frac{y^2}{2}\right)xF_3\right], \tag{2.5}$$

where α is the fine structure constant and F_1, F_2, and F_3 are the dimensionless structure functions of the proton, discussed in more detail later. It is clear from equation 2.6 that the cross section falls rapidly ($\sim 1/Q^4$), with increasing Q^2, a consequence of the form of the virtual photon (γ^*) propagator.

2.2 The Simple Quark Parton Model

Solving the above form of the NC scattering cross section is then dependent on our ability to accurately describe the structure of the proton. In Feynman's parton model [14] the constituents of the proton are free, point-like objects called partons. The ep scatter is no longer considered as an inelastic lepton-proton scatter, but as an elastic scatter off a single parton.
In the infinite momentum frame of the proton the partons can be considered to be travelling collinearly in the proton direction, each carrying negligible transverse momentum. If the struck parton carries a fraction of the proton's whole momentum, ξ, and the parton mass is ignored, conservation of 4-momentum implies:

$$\begin{aligned} 0 \approx m^2 = (\xi p + q)^2 &= \xi^2 p^2 - Q^2 + 2\xi p.q \\ &\Rightarrow \xi = \frac{Q^2}{2p.q} = x\ . \end{aligned}$$

The Bjorken scaling variable x can then be associated with the fractional longitudinal momentum of the struck parton, ξ.
In 1969, Bjorken predicted "scaling", i.e the structure functions of equation 2.5, should only depend on x, and not on the virtuality of the probing photon. From the quark parton model (QPM) this is intuitively what might be expected, as only a single parton is probed regardless of the virtuality of the photon. The structure functions F_1 and F_2 can be written as,

$$F_2(x) = \sum e_q^2 x f_q(x) \tag{2.6}$$

$$F_1(x) = \frac{1}{2}\sum e_q^2 f_q(x), \tag{2.7}$$

where e_q are the charges of the partons and $f_q(x)$ are parton distribution functions (PDFs) describing the probability of finding a parton of flavour q with momentum fraction x in the proton. F_1 and F_2 are connected by the Callan-Gross Relation,

$$F_1(x) = \frac{1}{2x}F_2(x), \tag{2.8}$$

a consequence of the fact that partons in the QPM are massless spin $\frac{1}{2}$ particles that do not interact with one another. The longitudinal structure function F_L, can be defined as

$$F_L(x) = F_2 - 2xF_1(x) \tag{2.9}$$

and with the Callan-Gross relation implies that the cross section for longitudinally polarised photons vanishes. The presence of a non-zero F_L hints at the need for a refinement to this simple model.
The structure function F_3 of equation 2.5 describes parity violating Z^0 exchange which is negligible for $Q^2 \ll M_Z^2$, and as such can be ignored in the kinematic region of the analyses presented in this thesis. The cross section can then be written as

$$\frac{d^2\sigma^{ep}}{dxdQ^2} = \frac{2\pi\alpha^2}{xQ^4}[Y_+F_2 - y^2F_L], \tag{2.10}$$

where the helicity dependence is contained within

$$Y_\pm = (1 \pm (1-y)^2). \tag{2.11}$$

These partons were eventually associated with the quarks of Gell-Mann and Zweig, through observations at SLAC and of μN scattering [15], and the model became known as the quark parton model.

2.3 The Improved Quark Parton Model

A proton consisting only of charged quarks would have total momentum equal to the sum of all quark momenta,

$$\sum_i \int_0^1 dx f_i(x) x = 1. \tag{2.12}$$

Experimentally this value was determined to be ≈ 0.5 [16], implying that just half of the proton's whole momentum is carried by charged partons. The remaining momentum is then carried by a neutral parton, the gluon, direct evidence for which was provided in 1979 at DESY via the observation of three-jet events in e^+e^- annihilation [17].

In the QCD improved quark parton model the emission of gluons must be accounted for. The assumption that the partons carry negligible transverse momentum in the infinite momentum frame, is no longer reasonable. A quark emitting a gluon can acquire a large transverse momentum, and the structure functions no longer just depend on x_p. A scaling violation is introduced, with contributions proportional to $\alpha_s \ln Q^2$, giving the structure functions a logarithmic dependence with Q^2 at fixed x_p. Observations have confirmed this behaviour, with a recent measurement of the x and Q^2 dependence of F_2 from ZEUS [18] shown in Figure 2.2.

At large values of x, the emission of gluons by valence quarks dominates and the quark densities are seen to fall with Q^2. The low x region is more heavily populated by "sea" quarks and gluons from $g \to q\overline{q}$ and $g \to gg$ splittings and much stronger scaling violations are observed, with F_2 increasing rapidly with Q^2

.

2.4 Evolution Schemes

The presence of this scaling violation implies that the momentum distribution of quarks and gluons within the proton evolve with increasing scale. In order to describe this requires first a suitable theoretical treatment of the splitting $q \to qg$. The probability of a quark emitting a gluon such that the quark has reduced momentum fraction z, $P_{q\to qg}(z,\tau)$, is calculated from Compton scattering to be,

$$P_{q\to qg}(z,\tau) = \delta(1-z) + \frac{\alpha_s}{2\pi} P_{qq}(z)[\tau - \tau_0] \tag{2.13}$$

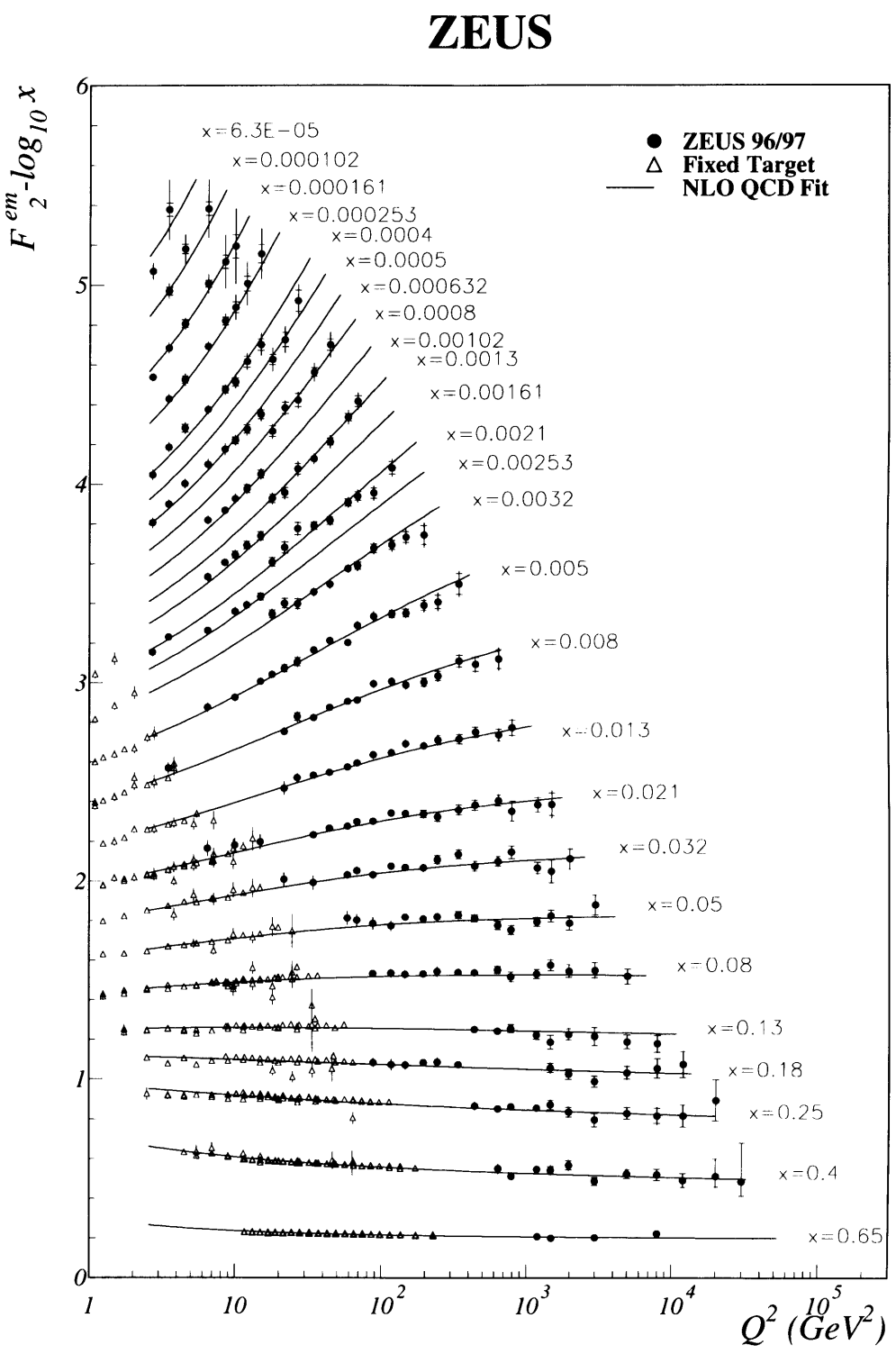

Figure 2.2: $\mathrm{F}_2^{\mathrm{em}}$ *as a function of* Q^2 *in bins of x. The ZEUS data together with that of the fixed target experiments NMC, BCDMS, and E665 are shown along with the ZEUS NLO fit.*

Where τ and τ_0 are scale dependent factors and P_{qq} is the *splitting function* given by,

$$P_{qq} = \frac{4}{3}\left(\frac{1+z^2}{1-z}\right) \tag{2.14}$$

leading to a divergence as $z \to 1$. Integrating over the transverse momentum, k_T, of P_{qq} results in a further divergence arising from collinear emissions with $k_T \to 0$. The first "soft singularities" cancel against infra-red singularities from one-loop corrections to the quark propagators and virtual photon quark scattering, $\gamma^* q \to q$. The factorisation theorem of collinear singularities [19] allows for collinear emissions to be factorised into universal parton densities if the scale Q^2 is greater than some cutoff Λ. The scale dependence of the quark and gluon densities can then be calculated perturbatively, leading to the QCD parton evolution equations discussed below.

2.4.1 DGLAP Evolution

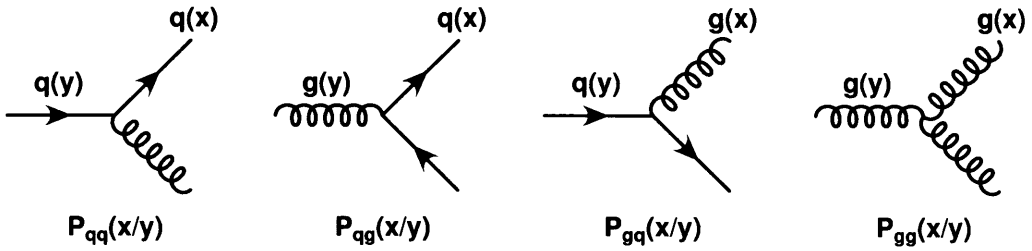

Figure 2.3: *The Altarelli-Parisi splitting functions to first order, used in the DGLAP evolution equations.*

The Dokschitzer-Gribov-Lipatov-Altarelli-Parisi (DGLAP) evolution equations [20] are given by

$$\frac{dq_i(x,Q^2)}{dlogQ^2} = \frac{\alpha_s}{2\pi}\int_x^1 \frac{dy}{y}\left[q_i(y,Q^2)P_{qq}\left(\frac{x}{y}\right) + g(y,Q^2)P_{qg}\left(\frac{x}{y}\right)\right] \tag{2.15}$$

$$\frac{dg(x,Q^2)}{dlogQ^2} = \frac{\alpha_s}{2\pi}\int_x^1 \frac{dy}{y}\left[\sum_i q_i(y,Q^2)P_{gq}\left(\frac{x}{y}\right) + g(y,Q^2)P_{gg}\left(\frac{x}{y}\right)\right] \tag{2.16}$$

and describe the evolution of the quark densities, $q_i(x,Q^2)$ and gluon densities $g_i(x,Q^2)$ with changing scale, in the leading log approximation where dominant

logarithmic terms at intermediate x and large Q^2 were summed to all orders. They are given in terms of the four splitting functions $P_{jk}(\frac{x}{y})$, shown to first order in figure 2.3, and represent the probability of a parton k with momentum fraction y emitting a parton j with momentum fraction x as the scale changes.
In practice the amplitude of ep scattering in the deep inelastic limit ($Q^2 \gg \Lambda$) is obtained by the addition of successive gluon emissions, represented by the ladder diagram of figure 2.4. In the DGLAP approximation the ladder is ordered strongly in transverse momentum, such that $k_{t_1}^2 \ll k_{t_2}^2 \ll .... \ll k_{t_{n-1}}^2 \ll k_{t_n}^2 < Q^2$.

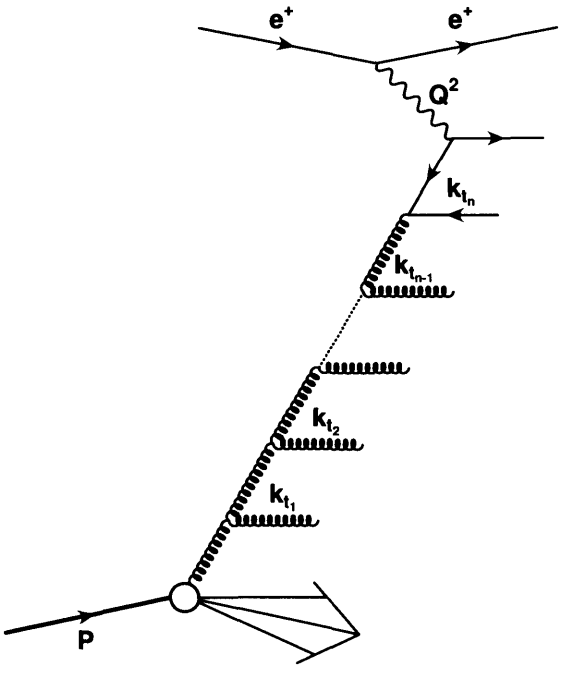

Figure 2.4: *A ladder diagram illustrating the production of initial state parton showers.*

The solutions to 2.15 and 2.16 give the evolution of the partonic densities with increasing Q^2 but says nothing about the evolution with x_p. Solving them then requires the determination of the structure functions at some suitable experimentally determined fixed scale Q_0^2.
In the applicable region the DGLAP equations have been shown to describe the scaling violations data (figure 2.2) to a high degree of accuracy. The validity of the DGLAP approach relies upon the neglected terms, particularly those in $\ln(1/x)$, being small. At small momentum fraction x these terms can be large and the DGLAP equations may break down and another approach is necessary.

$P_{jk}(\frac{x}{y})$	DGLAP	BFKL($z \to 0$)
$P_{qq}(\frac{x}{y})$	$\frac{4}{3}[\frac{1+z^2}{(1-z)_+}] + 2\delta(1-x)$	$\frac{4}{3}$
$P_{qg}(\frac{x}{y})$	$\frac{1}{2}[z^2 + (1-z)^2]$	$\frac{n_f}{2}$
$P_{gq}(\frac{x}{y})$	$\frac{4}{3}[\frac{1+(1-z)^2}{z}]$	$\frac{2}{z}$
$P_{gg}(\frac{x}{y})$	$6[\frac{1-z}{z} + z(z-1) + \frac{z}{(1-z)_+} + \frac{11}{12}\delta(1-z)] - \frac{n_f}{3}\delta(1-z)$	$\frac{6}{z}$

Table 2.1: *The AP splitting functions in the high Q^2 and x region (DGLAP) and in the very small x limit of BFKL.*

2.4.2 BFKL Evolution

The approach of Balitsky-Fadin-Kuraev-Lipatov (BFKL) [21] differs from that of DGLAP in a number of important respects. A modified leading log approximation is applied in which the leading terms in ln(1/x) are summed to all orders. This leads to a ln(1/x) dependence to the evolution of the parton densities in the very low x limit. A further implication is that very low x implies very low z, and in the limit $z \to 0$ the AP splitting functions are simplified. A comparison of the AP splitting functions applied in DGLAP and those of BFKL in the limit of $z \to 0$ are shown in table 2.1. The $1/z$ dependence of the gluon splittings lead to a dominant contribution at low x from gluons, and only gluon emissions ordered strongly in fractional momentum x, such that $x_1 \gg x_2 \gg ..... \gg x_{n-1} \gg x_n$, contribute to the ladder (figure 2.4). The BFKL scheme predicts that the structure function F_2 will show a steep rise at very low x, which is also accommodated by DGLAP in it's range of applicability. Confirmation of this behaviour was later provided through observations at HERA.

The leading order solutions to the BFKL evolution equations have no Q^2 dependence, however at intermediate values of x terms in $\alpha_s(Q^2)$ ln1/x become important. A unified approach covering more of the $x - Q^2$ plane of figure 2.5 would clearly be useful, but is theoretically challenging.

2.4.3 CCFM Evolution

A modified approach, in which the leading logs in both $1/x$ and Q^2 are taken as the dominant terms, can be applied as long as Q^2 is relatively large.

This Double Leading log Approximation (DLLA) leads then to strong ordering in both k_t^2 and x. A generalised treatment of the gluon ladder in the DLLA is given by Ciafaloni-Catani-Fiorani-Marchesini (CCFM) [22], with angular ordering such that $\eta_0 < \eta_1 < .... < \eta_n$, with the scale, $\overline{q}$ of the evolution being determined by some cutoff, Ξ, representing the maximum angle at which partons can be emitted.

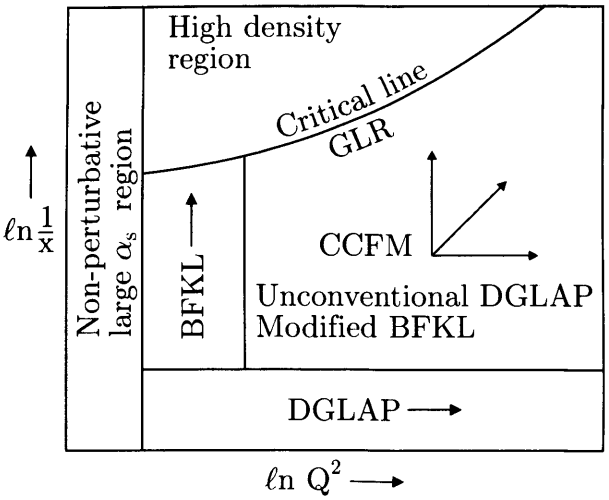

Figure 2.5: *The kinematic regions of applicability for DGLAP, BFKL and CCFM evolution.*

The ln(1/x) and $\ln(Q^2)$ terms are resummed into the parton densities to give an evolution which is potentially valid at all values of x and Q^2. The final evolution is given in terms of the unintegrated gluon density $\mathcal{A}(x, k_t^2, Q^2)$, which is scale dependent. As $x \to 0$ the logarithms in Q^2 become small and the integral of $\mathcal{A}(x, k_t^2, Q^2)$ can be reasonably assumed to be that of BFKL. At larger x ordering in k_t^2 is restored and the integrated gluon distribution of DGLAP $g(x, Q^2)$ is recovered. The final CCFM equation of the unintegrated gluon density $\mathcal{A}(x, k_t^2, Q^2)$ is written in differential form as,

$$\overline{q}\frac{d}{d\overline{q}^2}\frac{x\mathcal{A}(x, k_t, \overline{q}),}{\Delta_s(\overline{q}, Q_0)} = \int dz \frac{d\phi}{2\pi}\frac{\tilde{P}(z, \overline{q}/z, k_t)}{\Delta_s(\overline{q}, Q_0)} x' \mathcal{A}(x', k_t', \overline{q}/z), \tag{2.17}$$

where Δ_s is the Sudakov form factor, and $\tilde{P}$ is the splitting function with $z = x/x'$. The CCFM formalism allows for a number of different solutions of the unintegrated gluon density $\mathcal{A}(x, k_t, \overline{q})$ depending on the choice of Δ_s and $\tilde{P}$. In order to solve equation 2.17 a suitable form of $\mathcal{A}(x, k_t, \overline{q})$ must be predetermined. This approach, as implemented in leading order parton shower Monte Carlo generators, has been shown to be very successful in describing a large range of HERA data.

2.5 The Weizsacker-Williams Approximation

The dominant contribution to the total ep cross section is from the exchange of very low virtuality photons. In such exchanges the electron may be pictured as

emitting a photon of virtuality, Q^2, with a lifetime of $\sim yE_e/Q^2$. It is useful then to calculate the total ep cross section, σ_{tot}^{ep}, in two stages, effectively the product of the γp cross section $\sigma_{tot}^{\gamma p}$, and a photon flux factor, $f_{e\to\gamma e}(y)$, describing the probability of an electron emitting a photon with energy yE_e.
In the photoproduction region the photons are massless, transversely polarised bosons emitted collinear to the beam line. However a virtual photon with large Q^2 , $Q^2 \gg 0$ acquires a significant longitudinal polarisation. The total ep cross section can then be rewritten in terms of the individual longitudinal and transverse cross sections, $\sigma^{\gamma_L p}$, $\sigma^{\gamma_T p}$, and flux factors $f_{e\to\gamma_L e}(y)$, $f_{e\to\gamma_T e}(y)$,

$$\sigma^{ep} = \int [f_{e\to\gamma_T e}(y)\sigma^{\gamma_T p} + f_{e\to\gamma_L e}(y)\sigma^{\gamma_L p}]. \tag{2.18}$$

From the DIS proton structure functions we obtain

$$\frac{d^2\sigma^{ep}}{dydQ^2} = \frac{\alpha}{2\pi}\frac{1}{Q^2}[\left(\frac{1+(1-y)^2}{y} - 2\frac{(1-y)}{y}\frac{{Q^2}_{min}}{Q^2}\right)\sigma^{\gamma_T p}(y,Q^2)$$

$$+f_{e\to\gamma_L e}(y)\sigma^{\gamma_L p}(y,Q^2)], \tag{2.19}$$

where ${Q^2}_{min} = m_e^2 y^2/(1-y)$ and is the kinematic lower band. As we have previously mentioned in the limit $Q^2 \to 0$ the longitudinal flux, $f_{e\to\gamma_L e}(y)$, disappears, leaving only the first half of the above equation, such that

$$\frac{d^2\sigma^{ep}}{dydQ^2} = f_{e\to\gamma e}(y,Q^2)\sigma_{tot}^{\gamma p}(y,Q^2), \tag{2.20}$$

with

$$f_{e\to\gamma e}(y,Q^2) = \frac{\alpha}{2\pi}\frac{1}{Q^2}\left(\frac{1+(1-y)^2}{y} - 2\frac{(1-y)}{y}\frac{{Q^2}_{min}}{Q^2}\right). \tag{2.21}$$

This is the equivalent photon approximation (EPA), which in the low Q^2 range of photoproduction can be integrated over to give the Weizsacker-Williams Approximation [23],

$$f_{e\to\gamma e}(y) = \frac{\alpha}{2\pi}\left[\frac{1+(1-y)^2}{y} ln\frac{{Q^2}_{max}}{{Q^2}_{min}} - 2\frac{(1-y)}{y}\left(1-\frac{{Q^2}_{min}}{{Q^2}_{max}}\right)\right], \tag{2.22}$$

used widely in theoretical calculations of ep scattering.
So far only "soft" photon interactions have been dealt with, in which the four momentum transfer of the photon is too small to act as a hard scale for perturbative calculations. Low virtuality photon exchange can however have a large associated momentum transfer, in which high transverse energy jets of hadrons can be produced, even though the virtuality of the photon is small. This is referred to as hard photoproduction and is discussed in more detail later.

2.6 Photon Structure

The concept of "photon structure" may at first glance appear paradoxical, the photon has no mass, does not couple to itself and has no intrinsic structure, at least not in the way that a proton has a definite set of valence quarks. The photon can however couple to charged particles, and as such can fluctuate to fermion-antifermion pairs. The photon then acts as a source of partons, which at high energies and low photon virtualities can have a long lifetime on the scale of the hard subprocess. The long lifetime of these fluctuations allows for the partons to participate in the hard interaction. This behaviour can be conveniently described as "photon structure", and modelled in a way analogous to the treatment of proton structure.

The uncertainty principle allows for the splittings $\gamma \rightarrow q\overline{q}$, to exist for a time $\Delta t \leq h/2\pi\Delta E$, where ΔE is the difference in energy between the photon and the $q\overline{q}$ pair. For a sufficiently long lived fluctuation QCD allows for the $q\overline{q}$ pair to radiate gluons, which in turn can act as a source of partons. At low Q^2 (long-lived fluctuations) a cloud of soft gluons can form around the $q\overline{q}$ pair, forming a hadronic state with the same quantum numbers as the photon. The vector meson dominance model (VMD) attempts to describe this process by taking a coherent sum of the lowest lying vector meson states, with spin of unity and neutral charge. It is expected, however, that at higher values of Q^2 the VMD component is suppressed, as the lifetime of the fluctuation becomes too short for the bound hadronic state to evolve. The cross section is however generally dominated by processes involving a single quasi-free quark from the photon splitting taking part in the hard process. The contribution such processes make to the total resolved cross section are referred to as the anomalous photon contribution, and are perturbatively calculable for large enough scales.

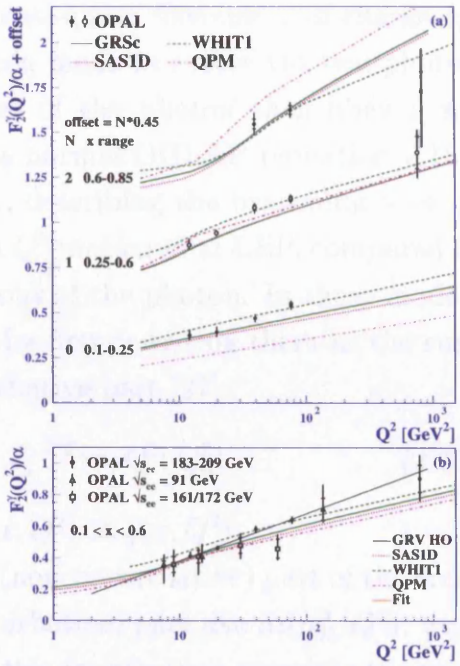

Figure 2.6: *Measurement of the photon structure function F_2^γ from LEP compared to the predictions of various virtual photon PDFs.*

The photon structure functions are measured directly in deep inelastic $e\gamma$ scattering [25]. Such measurements take advantage of the F_2^γ proportionality of the $e\gamma$ cross section. This cross section for a virtual photon of virtuality Q^2 scattering off an on shell real photon, resulting in a final state eX can then be written in terms of the photon structure functions F_2^γ and F_L^γ.

$$\frac{d^2\sigma_{e\gamma\to eX}}{dx_\gamma dQ^2} = \frac{2\pi\alpha^2}{x_\gamma Q^4}[(1+(1-y)^2)F_2^\gamma(x_\gamma,Q^2) - y^2F_L^\gamma(x_\gamma,Q^2)] \tag{2.23}$$

Here we see that the F_3 term is neglected as we are not considering Z^0 exchange. At leading order we can express the photon structure function F_2^γ as a charge weighted sum of the quark densities of the photon, in exactly the same way as we did for the proton.

$$F_2^\gamma(x_\gamma,Q^2) = 2x\sum e_i^2[q_i^\gamma(x_\gamma,Q^2) + \overline{q_i}^\gamma(x_\gamma,Q^2)] \tag{2.24}$$

where again the sum runs over all quark and anti-quark flavours, i, of charge e_i^2. For a restricted range of Q^2 attempts have been made to evolve the real photon PDFs in Q^2. The quark and gluon densities of the photon then obey a set of evolution equations, essentially the same as normal DGLAP (equation 2.15), with the addition of an anomalous term, a(x), describing the branching $\gamma \to q\overline{q}$ [26]. Figure 2.6 shows the evolution of F_2^γ with Q^2 measured at LEP, compared to the predictions of a number of parameterisations of the photon. In these models the parton densities of the photon are solved by first rewriting them as the sum of two terms, a perturbative and a non-perturbative part [27].

$$f_a^\gamma(x,Q^2) = f_a^{\gamma,NP}(x,Q^2;Q_0^2) + f_a^{\gamma,PT}(x,Q^2;Q_0^2) \tag{2.25}$$

where a =q_i,g, $f_{q_i}^\gamma(x,Q^2) \equiv q_i(x,Q^2)$, and $f_g^\gamma(x,Q^2) \equiv g(x,Q^2)$.
Such treatments predict the vector meson like (non-perturbative) part of the cross section to fall as Q^{-4} and the anomalous (perturbative) part like $ln(\mu_R^2/Q^2)$, with increasing photon virtuality, Q^2. To interpret this we can then associate the non-perturbative part with fluctuations of the type $\gamma \to V$ in accordance with the previously described vector meson dominance (VMD) model. The perturbative part is then associated with the anomalous photon component. The discrete spectrum of vector mesons is then combined with the continuous spectrum of quark anti-quark fluctuations to give,

$$f_a^\gamma(x,Q^2) = \sum \frac{4\pi\alpha_{em}}{f_V^2} f_a^{\gamma,V}(x,Q^2;Q_0^2) +$$

$$\frac{\alpha_{em}}{2\pi}\sum 2e_q^2\int_{Q_0^2}^{Q^2}\frac{dk^2}{k^2}f_a^{\gamma,q\bar{q}}(x,Q^2;k^2) \tag{2.26}$$

Determining the exact parameterisations of the photon parton density is however problematic. Large errors on the measurement of F_2^γ mean additional assumptions are required. It is still unclear how to correctly treat the heavy quark content of the photon, the scale Q_0^2 and the form of the parton densities. The parameterisation of Schuler and Sjöstrand (SaS) [28] attempts a general description of the evolution of the perturbative and non-perturbative parts of equation 2.28, for a photon of virtuality P^2. The fact that the various models deal with these assumptions (and the treatment of the non-perturbative term) differently, accounts for the differences between predictions.

2.7 Virtual Photon Structure

The virtual photon can be parameterised by evolving (in Q^2) the PDF's of the real photon, in an analogous way to the evolution of proton PDFs (i.e DGLAP evolution). The evolution equations of the photon can be calculated exactly in pQCD for the restricted range of four momentum transfer ${Q^2}_0 < \mathrm{P}^2 < Q^2$. More challenging is the region $\Lambda_{\mathrm{QCD}} < \mathrm{P}^2 < {Q^2}_0$, where the evolution equations are not determined exactly within the bounds of perturbative QCD. A generalised form of the photon PDF of equation 2.26 was derived using a modified form of the DGLAP evolution equations in [28],

$$f_a^{\gamma^*}(x,Q^2,P^2) = \sum_V \frac{4\pi\alpha_{em}}{f_V^2}\left(\frac{m_V^2}{m_V^2+P^2}\right)^2 f_a^{\gamma,V}(x,Q^2;{Q^2}_0)$$

$$+\frac{\alpha_{em}}{2\pi}\sum_q 2e_q^2\int_{Q^2}^{{Q^2}_0}\frac{dk^2}{k^2}\left(\frac{k^2}{k^2+P^2}\right)^2 f_a^{\gamma,q\bar{q}}(x,Q^2;k^2). \tag{2.27}$$

Where the anomalous and VMD parts of the virtual photon are again parameterised separately.

2.8 Hard Photoproduction

Hard photoproduction is only possible because the outgoing quark may carry significant tranverse momentum which acts as a hard scale for the interaction.

At leading order, two high transverse energy jets are produced which reflect the general properties of the struck parton. Figure 2.7 shows some of the processes giving rise to dijet production at leading order.

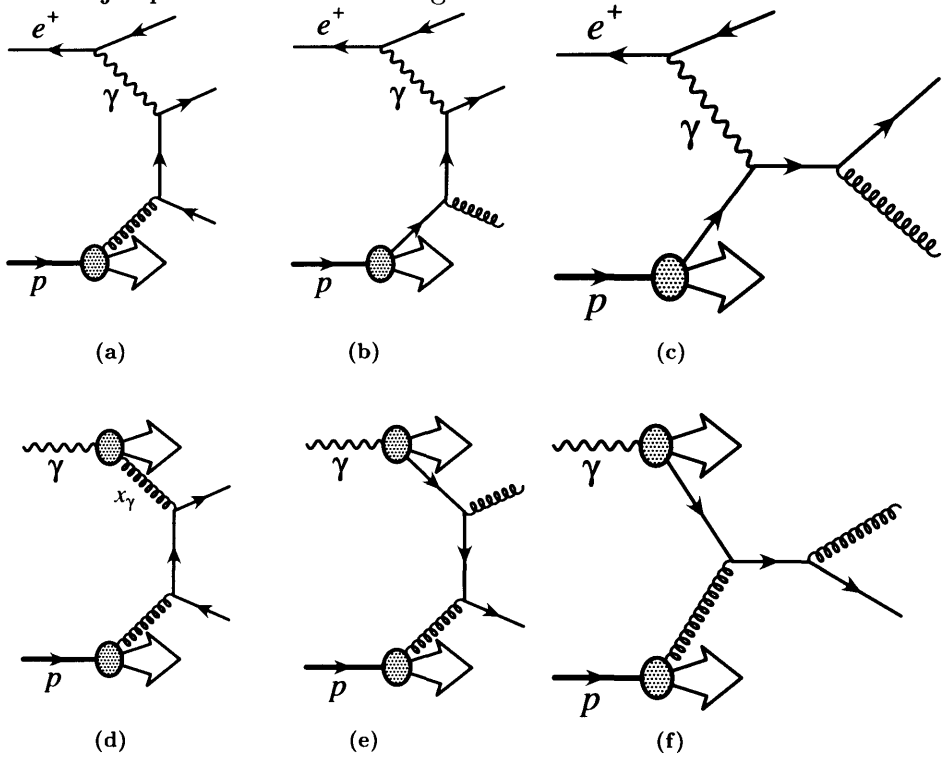

Figure 2.7: *Some of the leading order photoproduction processes. Direct processes (top) - (a) boson-gluon fusion, (b) initial state radiation and (c) compton scattering. Resolved processes (bottom) (d) gluon-gluon fusion, (e and f) flavour excitation from the photon.*

Figures 2.7a,b and c show processes in which the photon interacts as a point-like object coupling to sea (a) and valence (b and c) quarks from the proton. In these "direct" interactions the entire photon energy, E_γ, enters the hard process resulting in jets that are hard in transverse energy. Dijets are also produced in "resolved" photon interactions, shown in figures 2.7d,e and f. Resolved interactions are driven by the splitting of the photon into a $q\bar{q}$ pair, one of which may go on to take part in the "hard" interaction. Since the quark only carries a fraction of the photon's momentum, x_γ, resolved events are generally much softer than direct.

At leading order the fractional photon momentum taking part in the hard interaction, x_γ^{LO} is related to the tranverse energy and pseudorapidity of the

final state partons by,

$$x_\gamma^{LO} = \frac{\sum_{part} E_T^{part} e^{-\eta^{part}}}{E_\gamma}. \tag{2.28}$$

Where E_γ is the photon energy previously defined as yE_e. Experimentally the observable quantity, x_γ^{OBS}, is defined, which is obtained by running the sum over the two highest E_T jets,

$$x_\gamma^{\mathrm{OBS}} = \frac{\sum E_T^{jet} e^{-\eta^{jet}}}{yE_e}. \tag{2.29}$$

This then provides a simple way of differentiating between the two classes of events, with $x_\gamma^{\mathrm{OBS}} \approx 1$ for direct events and $x_\gamma^{\mathrm{OBS}} < 1$ for resolved [24]. In measurements however it is not possible to make an exact distinction between direct and resolved events, because x_γ^{OBS} for a direct event may be less than unity due to higher order emissions and non-perturbative effects such as parton showering and hadronisation, and resolved interactions can have x_γ^{OBS} approaching unity in some circumstances. Instead the term "direct enriched" is often used to describe the region $x_\gamma^{\mathrm{OBS}} > 0.75$ and "resolved enriched" for the region $x_\gamma^{\mathrm{OBS}} < 0.75$.

2.8.1 Jet Finding on the Hadronic Final State

Having accurately reconstructed the hadronic final state a suitable treatment must be applied to assign the hadrons to jets. The jets should be well defined at all orders, define quantities invariant under longitudinal boosts and result in jets which closely resemble the properties of the primary parton. This task is performed by a jet finding algorithm. In simulated events the algorithm can be made to run over partons emerging from the hard scatter, final state hadrons subsequent to hadronisation, or objects derived from the detector simulation.
The issues of collinear and infrared safety are also important factors in the design of an effective jet algorithm [38]. For an algorithm to be considered collinear and infrared "safe" it must satisfy the following requirements:

- **Collinear Safe** algorithms treat two collinear particles with momentum p_1 and p_2 identically to a single particle with momentum $p_3 = p_1 + p_2$. In theoretical calculations this implies insensitivity of the algorithm to the

collinear emission of partons. This is usually achieved by integrating over both the initial parton and the emission, thus treating the two as a single body. In real data the point is largely irrelevant since the detector is not able to resolve the collinear emission, instead the energy it deposits in the CAL is just counted with that of its "mother hadron".

- **Infrared Safe** algorithms are insensitive to soft emissions, which in theoretical calculations lead to large divergences as discussed earlier. Again the problem is less severe in real data, because low energy calorimeter deposits are removed from the final energy sum as they are indistinguishable from the uranium background noise.

A range of jet finders exist, notably the EUCELL [40] cone algorithm, and the longitudinally invariant k_T-clustering algorithm [41]. Whilst in some circumstances the cone algorithm may be a preferable choice, problems of infrared safety, and its inability to deal with overlapping jets [42], mean that the k_T-clustering algorithm is more widely used, and is the choice for all analyses presented in this thesis.

2.8.2 The Longitudinally Invariant k_T Clustering Algorithm

The k_T clustering algorithm compares each object (either a parton, final state hadron or EFO) with every other object and assigns them to the same jet if they lie close to one another in phase space. The exact method can be thought of as a six step procedure:

1. For each object, i, the distance parameter, d_i is calculated, where;

$$d_i = E_{T,i}^2. \tag{2.30}$$

2. The separation of each pair of objects i and j, d_{ij} is then calculated;

$$d_{ij} = min[E_{T,i}^2, E_{T,j}^2](\Delta\eta_{ij}^2 + \Delta\phi_{ij}^2). \tag{2.31}$$

3. The smallest value of all d_i's and d_{ij}'s is kept and assigned to d_{min}.

4. If d_{min} is a d_{ij} then the objects i and j are combined to form a new object k, with physical properties determined from the k_T recombination scheme, such that;

$$E_{T,k} = E_{T,i} + E_{T,j} \tag{2.32}$$

$$\eta_k = \frac{E_{T,i}\eta_i + E_{T,j}\eta_j}{E_{T,i} + E_{T,j}} \tag{2.33}$$

$$\phi_k = \frac{E_{T,i}\phi_i + E_{T,j}\phi_j}{E_{T,i} + E_{T,j}} \tag{2.34}$$

5. In the event that d_{min} is a d_i, the object i is no longer merged with other objects and is removed from the list of objects to be clustered. The removed object is referred to as a "protojet".

6. The procedure is repeated until all objects have been assigned to a protojet and removed from the list.

The final list of protojets are then sorted according to there transverse energy, E_T. Protojets with E_T below a user defined cut are removed, resulting in the final list of jets.

Chapter 3

Reconstruction of Event Kinematics

3.1 Reconstruction of the Hadronic Final State

Partons emerging from the hard scatter cannot be observed directly, therefore jets in the hadronic final state must be used to perform measurements. Whilst these jets do not exactly reflect the scattered parton they have properties largely determined by the hard process. Accurately reconstructing the jets gives a good approximation of the primary parton [29], which can be corrected for hadronisation effects and directly compared to theoretical predictions. The reconstruction relies primarily upon our ability to reconstruct the momentum and position of individual particles which form the jet. Once this is achieved a jet algorithm is used to group the final state particles into jets. A more detailed discussion of the reconstruction of the hadronic final state is given below.

3.1.1 Tracking Reconstruction

Tracks in the CTD are reconstructed using pattern recognition software, which initially runs over all hits in the detector. The information is used to perform a fit to the primary event vertex. Once determined all tracks originating from the vertex are refitted to determine which are likely to truly belong to the ep scatter. The track recognition software operating in this way performs with high efficiency.

3.1.2 Calorimeter Reconstruction

The energy of each cell in the calorimeter is unpacked and considered only if it meets the requirements detailed in [30]. A number of permanently noisy cells are removed prior to unpacking, according to lists of such cells in each given year [31]. As stated before, the calorimeter is largely composed of uranium which produces a background signal from simple β-decay. Therefore only cells containing energy, E, greater than some noise related threshold are reconstructed offline. Each cell is read out by two photomultiplier tubes (PMT), which logically should have approximately the same values. However, malfunctioning PMTs may fire randomly or continuously giving spurious readings. Against this a cut is applied, whereby cells are rejected if there is a large difference in measured energy between the two PMTs.

3.1.3 Calorimeter Energy Scale Uncertainty

Differences exist in the calorimeter response between data and Monte Carlo [34]. This is largely due to discrepancies in the description of showering in the ZEUS detector simulation. Calorimetric cells in real data require scaling up by some factor, determined from neutral current DIS studies [32] and dependent on where they lie in the detector. A factor of 2.5% is applied to all cells in the RCAL, and 5% to those in the BCAL and FCAL [33]. The scattered positron of DIS is dealt with separately, and no scaling factor is applied to these cells.

3.1.4 Energy Flow Objects (EFOs)

Both neutral and charged particles are measured by the CAL, however a large proportion of the charged particles are also measured by the CTD and associated tracking detectors. For low energy tracks, and for tracks traversing large volumes of dead material between the CTD and CAL (e.g. the CTD solenoid), the tracking information often provides a better measurement of the particle's momentum. Combining the CTD and CAL information into an energy flow object (EFO) [36] gives a more accurate reconstruction of the hadronic final state than either could in isolation.

At ZEUS combining the tracking and CAL information in this way is performed by the ZUFOs package [37], and any given energy flow object is referred to as a ZUFO. The reconstruction of EFOs at ZEUS is a three step procedure,

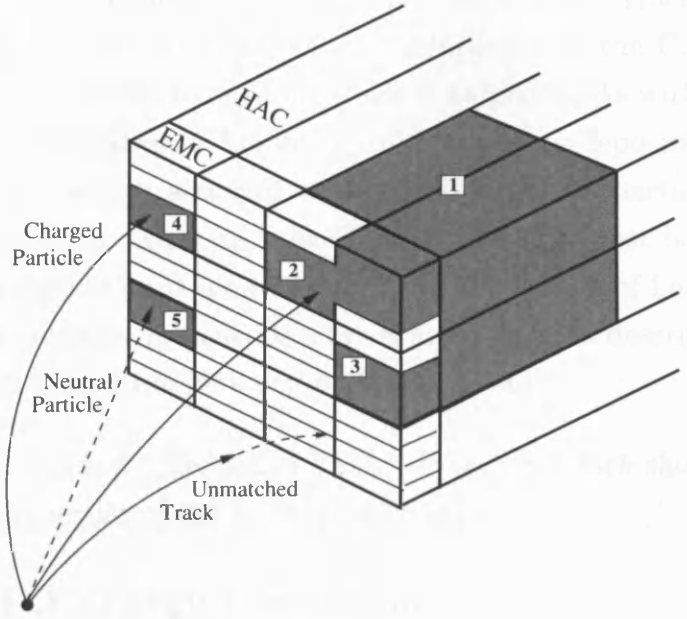

Figure 3.1: *Schematic representation of the main components used for calculating ZUFOs from calorimeter and tracking quantities.*

- **Clustering** is initiated by combining adjacent cells in the EMC, HAC1 and HAC2 separately as shown in figure 3.1. Information from both layers of the CAL are then combined to produce a three dimensional "cone island" [39], by considering the angular separation of the cell islands.
- **Matching** of tracks to cone islands begins by extrapolating all charged tracks in the CTD to the CAL surface. A number of track quality requirements must first be satisfied and only "good tracks" are matched. A good track is one that passes through at least 4 superlayers of the CTD with transverse momentum in the range $0.1 < p_T < 20$ GeV, with the upper limit being increased to 25 GeV for tracks passing through more than 7 superlayers. Finally tracks are excluded if they cannot be fitted to the primary vertex. A track is deemed to match if it passes within 20cm of a cone island.
- **A Decision** as to whether the CTD or CAL information should be used is only required for tracks which are matched to islands. The momentum resolution for each track in the CTD and the energy resolution of the

matching cone island in the CAL is calculated. Tracking information is used when the CTD has better resolution than the CAL, and the island energy is matched to only one track. Charged tracks with no energy deposit are all assumed to be low energy pions. Energy deposits not matched with any track are all assumed to come from neutral particles. Again in this case no choice exists and the CAL information must be used. Finally the CAL information is used to determine the energy of hadronic islands with more than three matched tracks. A more detailed description of the precise method than given here can be found in [36].

The result of this is a collection of EFO four-vectors which should better describe the overall properties of the hadronic final state.

3.1.5 EFO Energy Corrections

The inclusion of tracking information means that low energy charged particles that do not reach the CAL can be measured and included in the hadronic energy sum. However for hadrons with $E_T > 15$ GeV the fraction of tracking EFOs is negligible. The majority of EFOs are calorimeter EFOs which are subject to energy losses in dead material in front of the CAL, and a correction factor must be applied to better reflect the "true" hadronic energy.
The correction factor is determined in high Q^2 NC interactions, where the momentum of the scattered positron is well measured. The four-momentum of the hadronic shower is required to balance that of the positron through conservation of momentum. A minimisation procedure has been used to quantify the size of the correction. These factors are then applied to the CAL EFOs, with the magnitude of the correction depending on the polar angle, θ, and the uncorrected island energy of the EFO. The performance of this method is discussed in detail in [37].

3.2 Electron Identification

In DIS the scattered lepton is deflected through a significant angle, and even for relatively low values of Q^2 ($Q^2 > 1.5$ GeV^2) leaves a deposit in the RCAL.[1] These

[1] > 90% of scattered leptons are measured in the RCAL, however at very high Q^2 a significant number may be found in the BCAL.

electrons must be identified primarily because they can be used to reconstruct the kinematics of the event, but also so that they may be removed before jet finding. A number of "electron finders" are available, however the most widely used is SINISTRA [43].
SINISTRA is a neural network based electron finder which compares energy deposits in the electromagnetic calorimeter (EMC) with the total CAL energy deposit for a given particle. The ratio E_{EMC}/E_{TOT} is taken, and provides an efficient way of separating leptonic matter from hadronic, particularly at high energies. At lower energies the proportion of hadronic matter contained in the EMC rises rapidly and the purity of the selected electron sample falls accordingly. The efficiency is thus impaired for energies of < 5 GeV, and so a cut is usually applied to restrict electron finding to a suitable range of energies.

3.3 Electron Variable Reconstruction

The electron, once identified can be used to reconstruct the kinematics of the event, namely the kinematic variables Q^2 and y [44]. A number of methods are available, two of which are of relevance for analyses presented here.

3.3.1 Electron Method

The electron method relies upon the assumption that the lepton enters the hard scatter with the full electron energy E_e and leaves with the full measured energy $E_e^{'}$, i.e. that initial and final state radiative (ISR and FSR) corrections are small. The value of y and Q^2 then only depend upon the energy of the scattered lepton, $E_e^{'}$, and the angle at which it is scattered, θ_e. The relationship between these two quantities and the required kinematic variables according to the electron method are given by;

$$Q^2{}_e = 2E_eE_e^{'}(1 + cos\theta_e), \tag{3.1}$$

$$y_e = 1 - \frac{E_e^{'}}{2E_e}(1 - cos\theta_e). \tag{3.2}$$

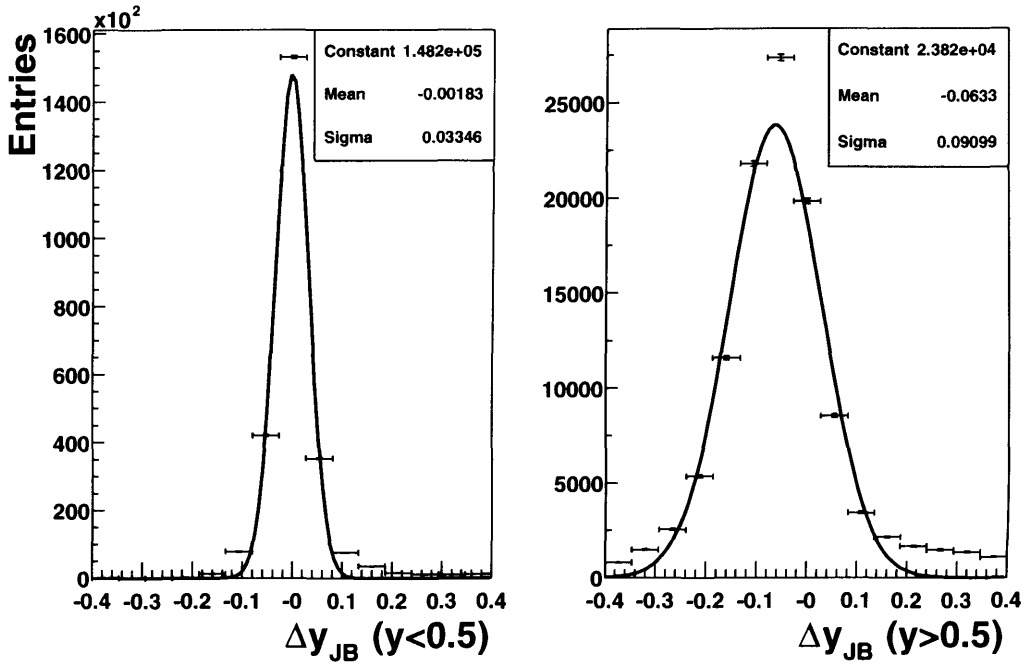

Figure 3.2: *The resolution of the variable y estimated from the Jacquet-Blondel method in two regions of true y for photoproduction events generated using the HERWIG MC generator. Here the quantity* $\Delta y = y_{\mathrm{JB}} - y$.

3.3.2 Jacquet-Blondel Method

At very low Q^2 and in photoproduction events, the electron angle θ_e is large ($> 176.5°$) and no electron is found in the CAL. At ZEUS, the absence of a scattered lepton is used as the definition of a photoproduction event, and whilst this can yield events with $Q^2 < 4.0$ GeV^2, studies have shown a mean $Q^2 \sim 10^{-3}$ GeV^2. The variables y and Q^2 must now be reconstructed from the final state. In practice this is done by summing over all final state particles, excluding the electron if it is present, giving the Jacquet-Blondel variables [45],

$$Q^2{}_{JB} = \frac{(\Sigma_h p_T)^2}{1 - y_{JB}} \tag{3.3}$$

$$y_{JB} = \frac{\Sigma_h (E - p_z)}{2E_e} \tag{3.4}$$

The sums can be made to run over either CAL cells or EFOs, with the latter giving better resolution. The overall resolution of the variables calculated using the Jacquet-Blondel method is generally not as good as for the electron method. Figure 3.2 shows the resolution of y_{JB} in two regions of y_{true}. It can be seen that

y_{JB} performs well with a mean at approximately zero. The resolution of ${Q^2}_{JB}$ (not shown) is very poor, and as such is only used in high-Q^2 studies where no electron is identified, e.g. CC DIS, and no other method is available.

3.4 Reconstruction of x_γ^{OBS}

The variable x_γ^{OBS}, defined in equation 2.29 is reconstructed from the two highest E_T jets found with the kt-clustering algorithm and y_{JB}. All variables are calculated using the corrected EFOs discussed previously.

Figure 3.3 shows the difference between x_γ^{OBS} calculated in this way and the "true" fraction of the photon momentum entering the hard scatter, x_γ. The resolution of the variable is observed to be excellent, with a mean centred very close to zero. This study was performed using a photoproduction sample from the HERWIG MC generator, however similar performance has been observed in DIS. This approach also has the advantage that both the jet variables and y are calculated from hadrons, and so the individual sensitivity of these to energy losses before the CAL largely cancel.

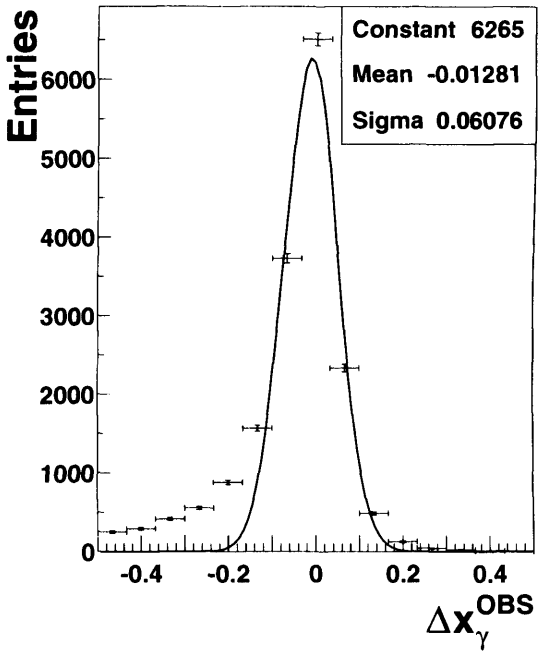

Figure 3.3: *The resolution of x_γ^{OBS} for events estimated using photoproduction events generated with the HERWIG MC generator.*

3.5 The Photon-Proton Centre of Mass Frame

So far the reconstruction of the event kinematics have been discussed only in terms of laboratory frame quantities, i.e. those quantities measured directly in the detector. This approach is perfectly valid for the electron variables discussed above, however caution must be exercised when calculating jet variables. At high Q^2 the transverse energy of the outgoing partons is balanced by that of the outgoing lepton, implying that the photon was not emitted collinear to the incoming proton. The jet transverse energy measured in the laboratory frame,

E_T^{lab}, then no longer represents the hard scale of the partonic interaction, and a boost is required to a frame where the incoming photon and proton are once again collinear. Such a frame is referred to as the photon-proton hadronic centre of mass (HCM) frame or the $\gamma^* p$ frame. For the general case a particle with four-momentum $\mathbf{P} = (\epsilon, \underline{\mathbf{p}})$ in the frame $\mathbf{S}$ can be boosted to another frame $\mathbf{S}'$ by the Lorentz transformations [46],

$$\underline{\mathbf{p}}' = \underline{\mathbf{p}} + \underline{\beta}\gamma(\frac{\gamma}{\gamma+1}\underline{\beta}.\underline{\mathbf{p}} - \epsilon) \tag{3.5}$$

$$\epsilon' = \gamma(\epsilon - \underline{\beta}.\underline{\mathbf{p}}) \tag{3.6}$$

such that the four-momentum of the particle in the frame S', is given by $\mathbf{P}' = (\epsilon', \underline{\mathbf{p}}')$. The problem is then to calculate the variables γ and $\underline{\beta}$ in the required frame. This is done by first defining an "auxiliary particle" with four-momentum $\mathbf{B} = (E, \underline{\mathbf{B}})$, whose rest frame is S', i.e. $\mathbf{B}' = 0$. The required variables are then found via the relationships,

$$\underline{\beta} = \frac{\underline{\mathbf{B}}}{E} \tag{3.7}$$

$$\gamma = \frac{1}{\sqrt{1-\underline{\beta}^2}} \tag{3.8}$$

The challenge then is to calculate the four-vector $\mathbf{B}$ on an event by event basis. The different approaches in photoproduction and DIS are now discussed in some detail.

3.5.1 Photoproduction

Photoproduction ($Q^2 < 1.0$ GeV^2) is a special case, in that the photon is still emitted approximately collinear to the incoming proton and no transverse boost is required. The asymmetry of the beam however means that a longitudinal boost in the photon (-z) direction is required. The transverse energy of the jets, E_T, is not changed by such a boost, neither is the distance between the jets in $\eta - \phi$ space. The boost is then trivial, being equivalent to a constant shift in η along the photon direction. For photoproduction the relationship between E_T and η in the lab frame and those in the photon-proton centre of mass frame are given by

$$E_{T,\gamma^* p} = E_{T,LAB} \tag{3.9}$$

$$\eta_{\gamma^* p} = \eta_{LAB} - ln\frac{2E_p}{E_\gamma} \tag{3.10}$$

Where E_p is the energy of the incoming proton and E_γ is the photon energy given by yE_e. The Jacquet-Blondel method was again used for estimating the variable y prior to performing the boost.

3.5.2 Deep Inelastic Scattering

In DIS the four-vector **B** can be calculated explicitly by reconstructing the outgoing electron four-momentum. The required four-vector is simply that of the photon-proton system in the laboratory frame, which is the sum of the photon and proton four-momenta, $\mathbf{P}_\gamma$ and $\mathbf{P_p}$,

$$\mathbf{B} = \mathbf{P}_\gamma + \mathbf{P_p} \tag{3.11}$$

where the photon four-momentum is reconstructed from the incoming and outgoing lepton four-momenta $\mathbf{P_e}$ and $\mathbf{P_{e'}}$ such that,

$$\mathbf{P}_\gamma = \mathbf{P_e} - \mathbf{P_{e'}}. \tag{3.12}$$

The vectors $\mathbf{P_p}$ and $\mathbf{P_e}$ are constant at HERA and given trivially by,

$$\mathbf{P_p} = (E_p, 0, 0, E_p) \tag{3.13}$$

$$\mathbf{P_e} = (E_e, 0, 0, -E_e), \tag{3.14}$$

where the proton and electron energies are 820 GeV and 27.52 GeV respectively.

3.5.3 Studies in the $\gamma^* p$ Frame

The effect of the boost on the jet variables E_T and η can be seen in figure 3.4. Each two dimensional plot contains the same number of events, to ensure any differences are not due to statistical effects. Figures 3.4 a-d show the effect on E_T of the boost in four regions of Q^2. The effect is not strong for $Q^2 < 10.0$ GeV^2 (Figures 3.4a and b), with most of the events lying on or near to the $E_T^{LAB} = E_T^{\gamma^* p}$ line. As Q^2 is increased however it can be seen that the effect is more marked, with an increased number of events lying away from this line.
Figures 3.4 e and f show the effect on η of the boost in both photoproduction and DIS, where the boost was performed using the methods described in sections

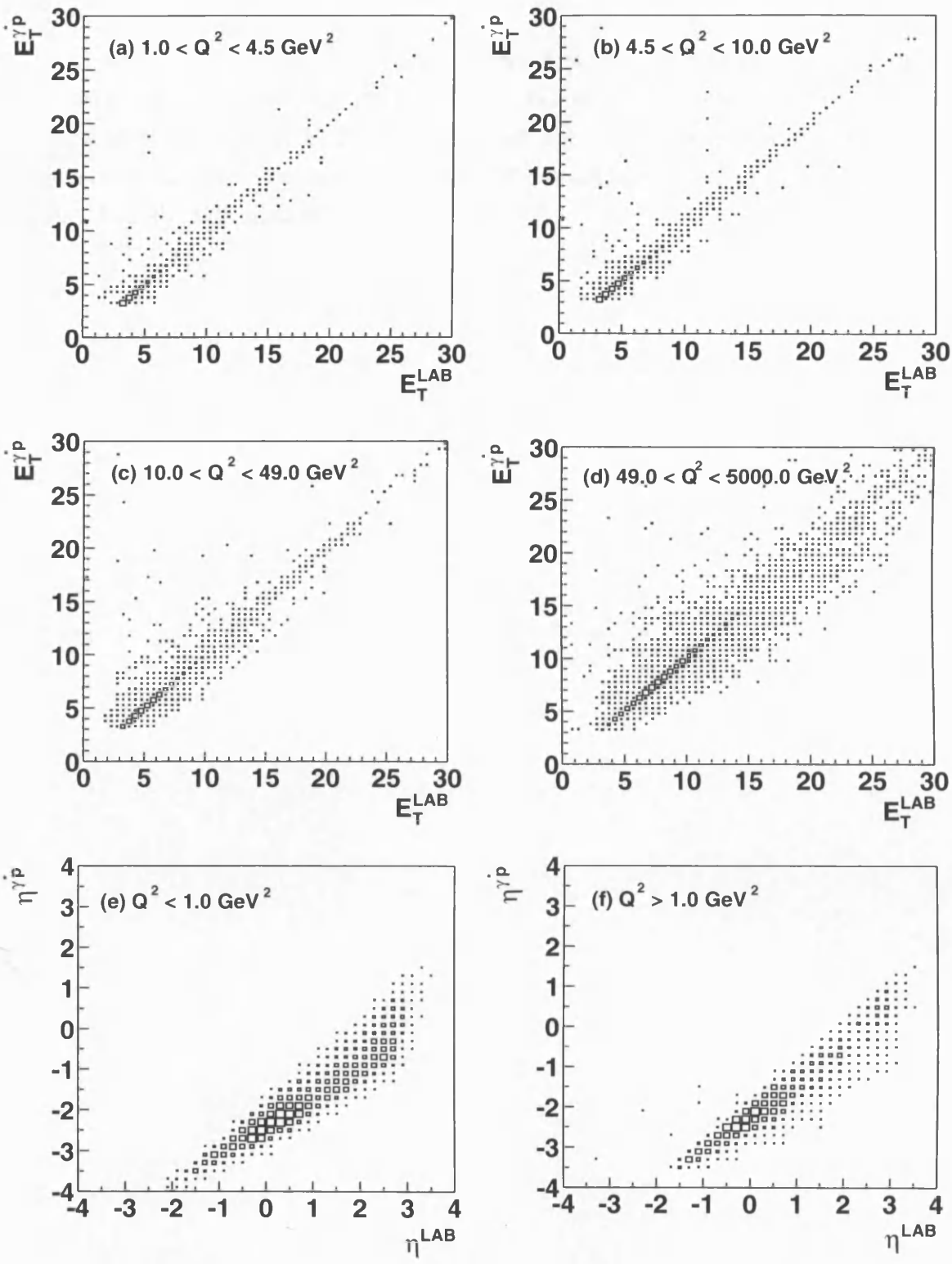

Figure 3.4: *The effect of a Lorentz boost to the photon-proton centre of mass frame, on the jet transverse energy, E_T,(a-d) and pseudorapidity, η (e and f). Figures a) through d) show the effect on E_T with increasing photon virtuality, Q^2. Figures e) and f) show the shift in η due to the boost in photoproduction and DIS separately. Each plot contains an equal number of events generated with the HERWIG MC generator.*

3.5.1 and 3.5.2 respectively. In both cases a strong shift in the -z direction is clearly visible, in line with expectations. Whilst the contrast between the two regimes is not as clear as in figures 3.4 a-d, the photoproduction distribution is generally confined to a narrower band and lies slightly closer to the $\eta^{LAB} = \eta^{\gamma^* p}$ line than the DIS distribution.

Part II

Inclusive Dijet Production

Chapter 4

Event Selection

In this chapter the criteria used to select data are explained, and a kinematic region in which all cross section measurements are carried out is defined. The data presented were collected with the ZEUS detector in the 96-97 running period, a data set corresponding to an integrated luminosity of 38.6 pb^{-1}. Beam conditions and the experimental apparatus during this period were stable and well understood. A combination of online trigger selection, and offline cuts designed to enhance the quality of the data sample were used to perform this analysis. In this chapter a detailed account of these procedures is given. Detailed information regarding the analysis is only given for the photoproduction measurement ($Q^2 < 1.0$ GeV^2) performed by the author. The photoproduction measurement was combined with measurements spanning a wider range of photon virtualities in order to draw conclusions, and as such it is necessary to give some details of the DIS analysis here.

4.1 Definition of Measured Cross Sections

All cross sections are defined in a region of phase space favourable for performing theoretical calculations reliably, and free of large uncertainties or divergences, and in a region where good experimental acceptance is expected. Inclusive dijet cross sections were measured for a wide range of photon virtualities, $0.0 < Q^2 < 2000.0$ GeV^2. Jets were reconstructed with the k_T-cluster algorithm running over the hadronic final state boosted in to the photon-proton centre of mass frame, in the longitudinally invariant mode [47]. At least two jets were required to lie in the region defined by,

- $E_T^{\mathrm{jet1,jet2}} > 6.5, 7.5$ GeV;
- $-3.0 < \eta^{\mathrm{jet}} < 0.0$.

The asymmetric cut on the jet transverse energies was chosen to avoid regions of phase space where next-to-leading order (NLO) calculations are unreliable [48]. A symmetric cut at 6.5 GeV would limit the phase space available for the emission of a gluon in the region of phase space near to $E_T^{\mathrm{jet1}} = E_T^{\mathrm{jet2}} = 6.5$ GeV. The positive contributions from the $2 \rightarrow 3$ body processes would then be suppressed in theoretical calculations, whilst the negative $2 \rightarrow 2$ body virtual contributions would not be suppressed, as no final state gluon is required, making the calculations infrared sensitive. The asymmetric cut avoids this sensitive region, with the higher transverse energy cut removing the singular region.
Additionally a y range is defined, limiting measurements to the region $0.2 < y < 0.55$. This selection is motivated by experimental considerations, with the lower limit removing beam gas events and the upper confines the measurement to a region of good experimental acceptance.
Cross sections differential in Q^2, transverse energy of the hardest jet, E_T^{jet1}, and pseudorapidity of the most forward or leading jet, η^f, have been measured. The contribution from resolved processes was enhanced by taking the ratio, R, of cross sections at low and high x_γ^{OBS} where,

$$R = \frac{d\sigma(x_\gamma^{\mathrm{OBS}} < 0.75)}{dQ^2} \Big/ \frac{d\sigma(x_\gamma^{\mathrm{OBS}} > 0.75)}{dQ^2}. \tag{4.1}$$

It should be noted that for simplicity x_γ^{OBS} is calculated from quantities in the laboratory frame. However x_γ^{OBS} can be redefined as an invariant quantity,

$$x_\gamma^{\mathrm{OBS}} = \frac{\sum_{jets}(E^{jet} - p_z^{jet})}{\sum_{hadrons}(E - p_z)}. \tag{4.2}$$

4.2 Online Event Selection

The three level trigger system, the general operation of which was described in section 1.6, was employed for the selection of dijet events online. Events containing two high transverse energy jets were selected by a complex chain of trigger logic, the precise details of which are given below.

4.2.1 First Level Trigger (FLT)

The first level trigger exploits the expected large energy deposited in the calorimeter in jet production. Events are required to satisfy at least one of the following energy sum requirements to pass FLT slot 42:

- The total energy in the calorimeter, E^{CAL}, excluding the three innermost rings of the FCAL, and the innermost ring of the RCAL, must satisfy $E^{CAL} > 15.0$ GeV.
- The electromagnetic calorimeter (EMC), excluding the same portions of the calorimeter as above, must have total energy, $E^{CAL}_{EMC} > 10$ GeV.
- The energy deposits in the EMC portion of the BCAL, $E^{BCAL}_{EMC} > 3.4$ GeV.
- The energy deposits in the EMC portion of the RCAL, $E^{RCAL}_{EMC} > 2.0$ GeV.

Additionally an event is vetoed if:

- The timing in the C5 counter is consistent with beam gas.
- Timing in the SRTD is consistent with beam gas.
- The proton bunch does not pass the veto wall in a time frame consistent with physics events.
- The proportion of vertex to total tracks is lower than the threshold value ($\sim 25 - 30\%$).

Finally a tracking requirement is made where the event is rejected if at least one track cannot be found originating from a region close to the nominal interaction region defined by,

- -50 cm $< z_{vtx} < 80$ cm.

4.2.2 Second Level Trigger (SLT)

Larger latency at the second level trigger means that more information is available for decision making. The entire range of calorimeter information is by this stage accessible (including transverse energies and precise timing from calorimeter photomultiplier tubes), as well as a greater range of tracking information. The selection at the second level is more stringent than at the first, and all of the following criteria must be satisfied:

- Beam gas events are further reduced by the requirement, -60 cm $< z_{vtx} <$ 60 cm.
- At least one track is associated with this vertex.
- $\sum E - p_z > 8.0$ GeV, where the sum runs over all calorimeter cells.
- If $\sum E - p_z > 12.0$ GeV then $\sum p_z/E < 0.95$.
- The total calorimeter transverse energy sum, E_T^{BOX}, excluding the previously mentioned FCAL and RCAL rings must satisfy $E_T^{\mathrm{BOX}} > 8$ GeV.

Also choices are made based upon timing in the calorimeter, where an event occurring at the nominal interaction position is timed at t=0. Events are excluded if:

- Cosmic ray events entering the detector from above are excluded if the response from the upper and lower halves of the BCAL have a delay such that, $t_{BCAL}^{\mathrm{low}} - t_{BCAL}^{\mathrm{high}} > 10$ ns.
- Events arising from the interaction of proton beam gas are removed if $t_{FCAL} - t_{RCAL} > 8$ns.
- $t_{RCAL} > 8$ns or $t_{FCAL} > 8$ns.

4.2.3 Third Level Trigger (TLT)

At the third level trigger $\sim$ 100 ms are available for decision making, and the full event information is available from all detector components. Both the calorimeter and tracking information have by this time been fully reconstructed, and a modified version of the EUCELL [40] algorithm is used to identify jets, and make a dijet requirement at this level. An event is selected if;

- At least two jets are found with $E_T^{jet} > 4.0$ GeV and $\eta < 2.5$, in the laboratory frame.
- $E - p_z < 75.0$ GeV.

- Less than six bad tracks are found. Bad tracks are defined as those which possess any of the following properties:

  $p_T < 0.2$ GeV.

  Hits in axial superlayers of the CTD ≤ 5.

  Hits in stereo superlayers of the CTD ≤ 5.

  Less than 20 degrees of freedom.

  Distance of closest approach to the vertex in z is > 75 cm.

Again calorimeter timing information is used to veto events from unwanted processes, in a similar way to the second level trigger.

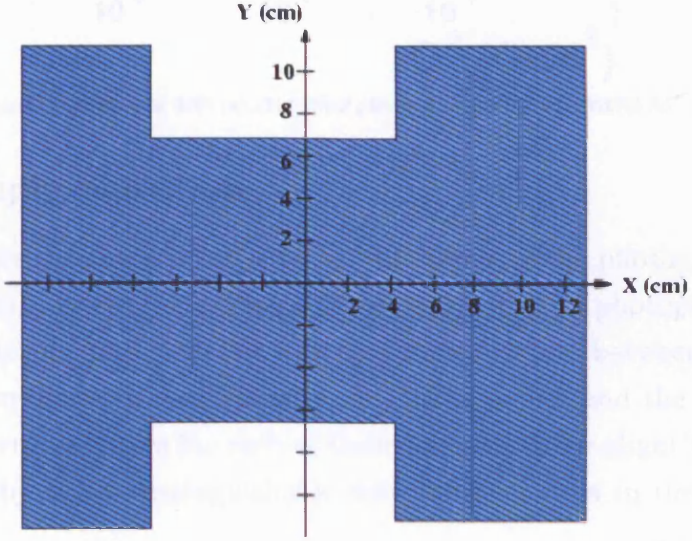

Figure 4.1: H-shaped box cut applied to the scattered electron in DIS.

4.3 Offline Event Selection

Further cuts were applied offline to improve the purity of the data sample before cross section measurements were made. The procedure used is described below.

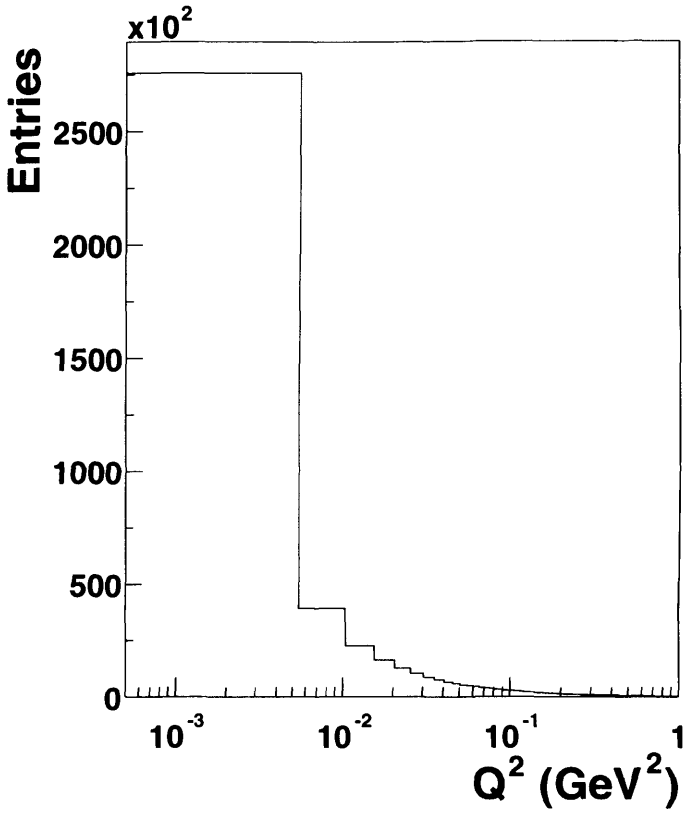

Figure 4.2: Q^2 distribution for events with no identified electron from the HERWIG MC generator.

4.3.1 Subsample Selection

The analyses presented in this section cover a wide range of the photon virtuality Q^2. Three distinct subsamples were separated corresponding to photoproduction, deep inelastic scattering and the low Q^2 transition region between the two regimes. This is convenient in part because the cuts applied, and the kinematic reconstruction of event variables for each of these samples differ slightly, but also they are separated by easily distinguishable detector responses in the following way:

- Photoproduction events were selected offline by requiring that no scattered positron was detected in the calorimeter. Events were also selected as photoproduction if a scattered positron with $E'_e < 5$ GeV or $y_e > 0.8$ was detected. Electrons are identified by the SINISTRA electron finder with efficiency approaching 100% above 5 GeV, and so the above veto recovers any photoproduction events with misidentified positrons. Figure 4.2 shows the final sample contains events with $Q^2 < 1.0$ GeV^2, and that the Q^2 distribution has its median at $Q^2 \sim 10^{-3}$ GeV^2.

- Events in the low Q^2 region defined by $0.15 < Q^2 < 0.55$ GeV^2 were selected by first requiring a scattered positron measured in the beam pipe calorimeter (BPC). The energy of the scattered positron was required to satisfy $E_e^{'} > 12.5$ GeV, removing misidentified electrons, and those that may have pre-showered before the BPC.

- Deep Inelastic Scattering (DIS) events were identified by the presence of a scattered positron in the main calorimeter. The positron is required to lie in an area of the calorimeter where the electron energy deposit is fully contained. This was achieved by requiring that the electron lie outside of an area around the rear beam pipe. The shape and dimensions of this "box cut" are shown in figure 4.1. This area was also chosen in such a way as to remove poorly simulated regions of the calorimeter. The final sample consisted of events in the range $1.5 < Q^2 < 2000$ GeV^2, which were further split into five subsamples corresponding to the Q^2 ranges $1.5 < Q^2 < 4.5$ GeV^2, $4.5 < Q^2 < 10.5$ GeV^2,$10.5 < Q^2 < 49.0$ GeV^2,$49.0 < Q^2 < 120.0$ GeV^2 and $120.0 < Q^2 < 2000.0$ GeV^2.

4.3.2 General Selection

Additional cuts were applied offline to enhance the purity of the sample. To minimise the loss of hadronic material down the forward and rear beam pipe, the event vertex was required to satisfy, $|z_{vtx}| < 40cm$, where z_{vtx} is measured from the nominal interaction point. A cut on the Jacquet-Blondel variable, y_{JB}, was made in order to further reject beam gas events. Events were selected lying in the range $0.2 < y_{JB} < 0.55$.
When a well reconstructed electron was available, the energy corrected EFOs were boosted into the photon-proton centre of mass frame prior to jet finding. The k_T cluster algorithm was then applied to the boosted EFOs to reconstruct jets in the photon proton centre-of-mass frame. In photoproduction the k_T-cluster algorithm was applied to the corrected EFOs in the laboratory frame, and the boost was calculated later using the method described in section 3.5.1.
Dijet events were then selected in the photon-proton centre of mass frame, by demanding the presence of at least two jets satisfying;

- $E_T^{jet1,jet2} > 6.5, 7.5$ GeV

- $-3 < \eta < 0$

These cuts remove low energy jets which are not measured accurately by the detector, and also confine the jets to a well understood region of the detector. In both photoproduction and DIS the jets were boosted back to the laboratory frame, and the variable x_γ^{OBS} was calculated from these quantities and y_{JB}. Defining x_γ^{OBS} in the laboratory frame in this way was found to give better resolution of the variable than defining it in the photon-proton centre of mass frame.

Chapter 5

Monte Carlo Simulation and Theoretical Calculations

The physical properties of a measured particle are obscured by finite resolving power, as well as regions of low efficiency and acceptance in the detector. Cross sections must be corrected back to the level of the emerging hadrons if comparisons between theory and data are to be made. In this chapter the methods and models used are discussed, and an overview is given of the leading-order and next-to-leading-order theoretical predictions used. Again the discussion concentrates on the authors contribution, namely the acceptance correction of the photoproduction measurement, all leading order theoretical predictions (photoproduction and DIS) and the next to leading order (NLO) photoproduction prediction. A brief description is also given of the DIS NLO calculations.

5.1 Event Simulation

The Monte Carlo method was used for generating events which describe the underlying physics processes. The physics simulation of jet production events was performed with a three step procedure. Leading order matrix elements are first used to calculate the hard scattering cross section giving rise, at leading order, to two partons. These partons then undergo "parton showering", where the colour potential between the two partons is used to derive further daughter partons, creating an emissions ladder described by some evolution scheme (see section 2.4). Finally these partons are combined in the "hadronisation" process, to produce the final state, colour neutral hadrons equivalent to those produced in *ep* scattering.

The generated events were passed through a modified version of the GEANT 3.13 [49] package called MOZART (Monte Carlo for ZEUS Analysis Reconstruction and Trigger). This package simulates the response of the ZEUS detector by accurately modelling its geometry and composition. The simulation by MOZART also incorporates information from a large number of studies of the ZEUS detector, including the effects of dead material (such as cables and cooling pipes), signal noise and the uranium background from the calorimeter. The trigger chain is then simulated by a separate package, ZGANA, before the event is reconstructed offline by the ZEPHYR program. At this stage the event is written to tape in the same format as a real event, except that in the case of a Monte Carlo generated event the full information about the "true" hadronic final state is also available.

5.2 Monte Carlo Generators

The cross sections were unfolded back to the hadron level using two leading-order Monte Carlo event generators. The primary sample was generated using the HERWIG [50] generator, a second sample was generated with PYTHIA [51] which was used to estimate systematic uncertainties arising from the choice of Monte Carlo program. A detailed discussion of each is given.

5.2.1 HERWIG

HERWIG [50] (Hadron Emission Reactions with Interfering Gluons) is a general purpose leading-order parton shower Monte Carlo event generator for the simulation of, among other processes, lepton-proton scattering. In this analysis samples of direct and resolved events were generated separately. The GRV-LO [52] paramaterisiation of the photon PDFs was used, with the flux of virtual photons from the lepton beam being calculated from the Weizsacker-Williams approximation [23]. The MRSA [53] set was used to parameterise the proton PDFs.

Parton showers are used to simulate initial and final state QCD radiation with the DGLAP evolution scheme. A cutoff in the angular ordered emissions is made, terminating the showering process. For a splitting $i \rightarrow jk$ the variable $\xi_{jk} = (p_j.p_k)/(E_j E_k)$ is defined and showering terminated when the value of $\xi < {Q^2}_i/E_i^2$. Fragmentation into hadrons is performed using the cluster model [54].

Final state gluons from parton showering are initially split into $q\bar{q}$ pairs. Quarks are then combined via colour connections formed during parton showering, into colour-neutral clusters. Light clusters are fragmented to a single hadron, whilst heavier clusters are decayed to two lighter hadrons. A soft underlying event (S.U.E.) model was implemented in order to simulate the presence in the final clusters of "spectator partons" from the proton.

5.2.2 PYTHIA

PYTHIA shares many similarities with HERWIG. The hard scattering cross section is again calculated from the LO QCD matrix element. The subsequent parton showering proceeds almost identically to that of HERWIG, except consecutive emissions are ordered according to their virtuality and the factorisation scale is chosen to be that of the transverse mass of the two outgoing partons, m_T given by,

$$\mu_{\mathrm{f}}^2 = m_T^2 = \frac{1}{2}(m_1^2 + p_{T1}^2 + m_1^2 + p_{T1}^2). \tag{5.1}$$

The treatment of hadronisation differs significantly between the two models. PYTHIA uses the Lund Symmetric String Fragmentation Model [55], implemented in the JETSET routine [56] [57], to produce hadrons. In this model partons are connected via colour strings, the energy potential of which increases as the partons move away from one another. New $q\bar{q}$ pairs are produced when it is energetically favourable to do so, removing energy from the colour string. Partons are combined into hadrons when it becomes no longer possible to produce further $q\bar{q}$ pairs from the available energy of the colour string. A large number of parameterisations of the photon and proton PDFs are available for use with PYTHIA, however for this analysis the GRV-LO and MRSA sets were again chosen.

5.2.3 Multi-Parton Interactions

The Monte Carlo description of x_γ^{OBS} is known not to describe the low x_γ^{OBS} tail present in the data distribution. The inclusion of Multi-Parton Interactions (MPI) [58] has been shown to soften the Monte Carlo x_γ^{OBS} distribution, and improve the description of the data [33]. Both samples were generated with MPI when generating resolved processes. These arise as a consequence of the

high parton densities, particularly in the small x limit, present at HERA. The primary hard scatter of a parton from the photon with a parton from the proton is accompanied by a softer secondary interaction. If the secondary scatter gives rise to two partons of sufficient transverse momentum a greater jet multiplicity is observed. Lower transverse momentum partons will contribute to make the final state hadronic jets appear harder in p_T than would otherwise be the case. The inclusion of MPI can lead to significant differences in predicted dijet cross sections, and models including a treatment of the phenomenon are generally favoured by measurements at HERA. HERWIG used the program JIMMY [59] and PYTHIA used the model described in [60] to randomly produce MPI and model the effects thereof.

5.2.4 Event Filters

In order to produce a Monte Carlo sample statistically high in events containing the physics under investigation, several filters were applied prior to the detector simulation. These prefilters serve to optimise event generation and processing, by removing from the sample those events which do not satisfy some loose, analysis specific, criteria.
A jet filter was applied to all generated events in the Q^2 range under investigation. The EUCELL jet finder was used to isolate jets at the hadron level in the laboratory frame, and events containing at least two jets with $E_T^{jet} > 3$ GeV and $\eta < 3.0$ were passed to the detector simulation for inclusion in the final sample. A second filter was applied only to Monte Carlo events inside the intermediate transition region between photoproduction and DIS, i.e those events which in the data would yield a scattered electron in the Beam Pipe Calorimeter (BPC). A loose cut on the azimuthal angle, $\phi_{e'}$, of the scattered electron is made such that electrons outside of the acceptance of the BPC are removed.

5.3 Direct and Resolved Processes

Direct and resolved events were generated independently in both the HERWIG and the PYTHIA samples. The fraction of direct to resolved events is not, however, known. The expected suppression of the resolved photon contribution also means that this proportion should change with increasing Q^2. The GRV-LO photon PDF has no such suppression included, as it is intended to describe real

Q^2 (GeV^2)	RESOLVED	DIRECT
$Q^2 < 1$	1.411	0.301
$0.1 < Q^2 < 0.55$	1.644	1.691
$1.5 < Q^2 < 4.5$	0.288	0.909
$4.5 < Q^2 < 10.5$	0.197	0.845
$10.5 < Q^2 < 49.0$	0.127	0.874
$49.0 < Q^2 < 120.0$	0.047	0.932
$120.0 < Q^2 < 2000.0$	0.047	0.932

Table 5.1: *Reweighting factors applied to resolved and direct Monte Carlo samples in different regions of Q^2.*

photons. In order to improve the agreement between Monte Carlo and data, direct and resolved samples were mixed according to a reweight factor determined from a two parameter chi-squared fit to the acceptance-uncorrected $x_\gamma^{\rm OBS}$ distributions from the real data. This was done for each of the Q^2 regions separately, effectively introducing a Q^2 suppression into the GRV-LO real photon PDF which matches that of the data. The reweight factors used are shown in table 5.1.

5.4 Description of data

In order for a Monte Carlo description to be used for acceptance corrections it must describe the main quantities used in the analysis. Figure 5.1 shows a comparison of the data and reweighted Monte Carlo distributions of the jet quantities E_T^{jet} and η^{jet}, and the quantity $y_{\rm JB}$. The jet quantity E_T^{jet1} is well described by the MC, as is E_T^{jet2}. The latter transverse energy however falls off more rapidly in the data than MC, but the effect is not large. η^{jet1} and η^{jet2} are both described well by HERWIG, although a slight enhancement in the forward direction is observed in the data. The distribution of y_{JB} is also described well by the model.

5.5 Leading Order Theoretical Predictions

HERWIG 6.4 [61] was used for the prediction of cross sections at leading order across the whole Q^2 range studied in this analysis including the region $0.15 < Q^2 < 0.55$ GeV^2 not covered by current NLO calculations. The details of the calculation are the same as those described in section 5.2.1, however the exact

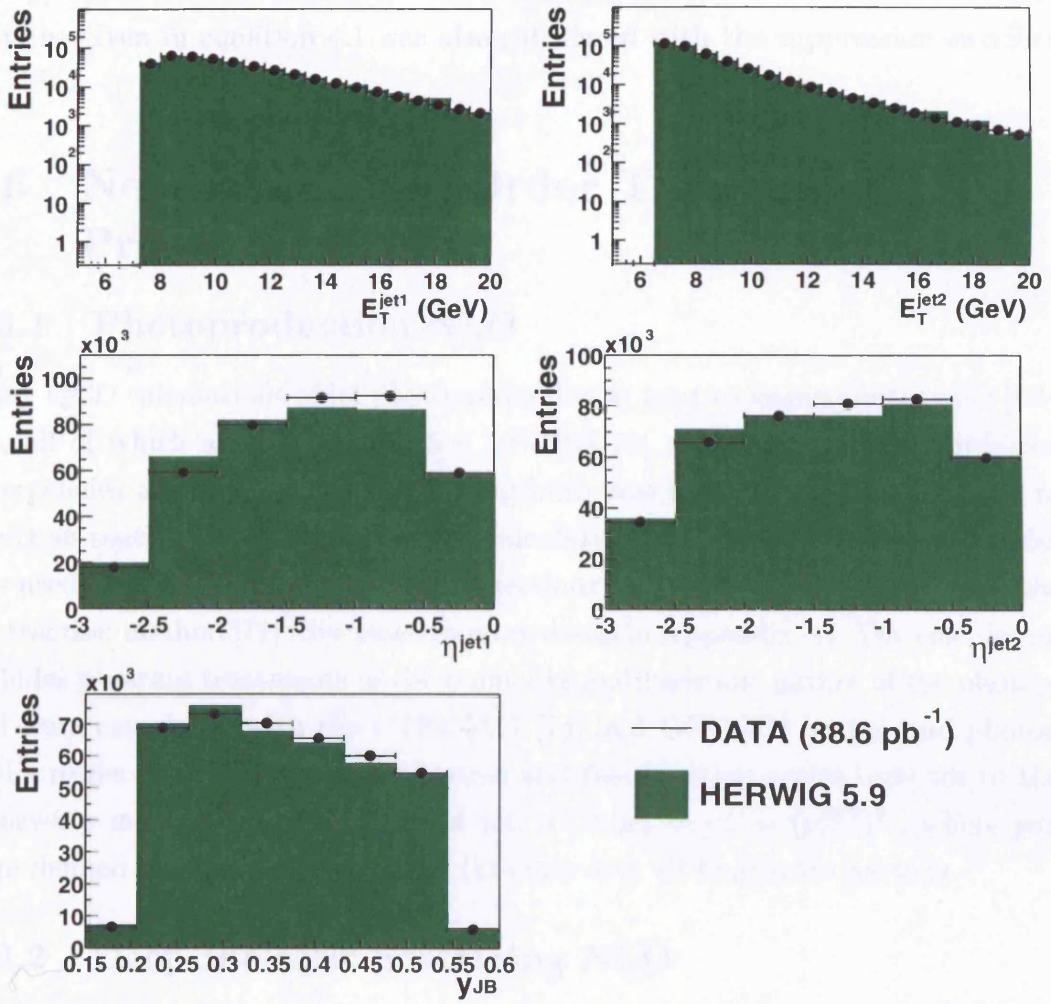

Figure 5.1: *Comparison of the distributions of data (points) and Monte Carlo (histogram) for jet quantities E_T^{jet} and η^{jet}, and the variable y_{JB}, for photoproduction events passing all data selection criteria.*

parameters used were tuned to many previous HERA and LEP measurements using the HZTOOL package [62]. The SaS2D and CTEQ5L parameterisations of the photon and proton PDFs were used respectively. Comparisons of all cross sections to these predictions are presented for the case where the photon PDF is suppressed with increasing Q^2, as discussed in section 2.7. The ratio of cross sections given in equation 4.1 was also calculated with the suppression switched off.

5.6 Next to Leading Order Theoretical Predictions

5.6.1 Photoproduction NLO

Many QCD calculations of jet photoproduction at next to leading order exist [63-69], all of which agree to within $5 - 10\%$ [69, 70]. A large number of infrared divergencies are found when calculating both real and virtual contributions to the cross section. In this analysis the calculation of Frixione and Ridolfi [63, 64] was used to produce infrared safe cross sections using a formalism based upon the subtraction method [71] (discussed in more detail in Appendix A). The calculation includes separate treatments of the point-like and hadronic nature of the photon, and were calculated with the CTEQ5M1 [74] and GRV [52] proton and photon PDFs respectively. The renormalisation and factorisation scales were set to the transverse momentum of the hardest jet, $\mu^2 = \mu_R^2 = \mu_F^2 = (p_T^{\mathrm{JET}})^2$, where jets were defined by running a jet finder (kt-clus) over all final state partons.

5.6.2 Deep Inelastic Scattering NLO

The NLO QCD calculations of the programs DISASTER++ [72] and DISENT [73] were used to compute jet production cross sections at NLO in DIS. DISENT and DISASTER++ make use of the subtraction method [71] and are performed in the massless $\overline{\mathrm{MS}}$ renormalisation and factorisation schemes. In these programs, the photon is treated as a point-like probe of the proton, and no partonic structure is explicitly assigned to the photon. A comparison between DISASTER++ and DISENT was made and they were found to agree to within $\pm 3\%$. The predictions presented here, had the number of flavours set to 5, the renormalisation and factorisation scales were $\mu^2 = \mu_R^2 = \mu_F^2 = Q^2 + (p_T^{\mathrm{JET}})^2$ and

Q^2 and $\alpha_s(\mu_R)$ was calculated at two loops using $\Lambda^{(5)}_{\overline{\rm MS}} = 226$ MeV, which corresponds to $\alpha_S(M_Z) = 0.118$. The CTEQ5M1 [74] set was used for the proton PDF.

5.7 Hadronisation Corrections

The next to leading order cross sections are calculated at the parton level, with no consideration of parton showering and hadronisation, which can effect the shape and absolute normalisation of the predicted cross sections. The effect was estimated using the HERWIG leading order Monte Carlo program in photoproduction, and a combination of the ARIADNE and LEPTO programs in DIS. A bin-by-bin correction factor, $C^{\rm HAD}$ was applied to the NLO cross sections, where $C^{\rm HAD}$ is given by,

$$C^{\rm HAD} = d\sigma^{\rm parton}_{\rm LO} / d\sigma^{\rm hadron}_{\rm LO}, \tag{5.2}$$

where $d\sigma^{\rm parton}_{\rm LO}$ and $d\sigma^{\rm hadron}_{\rm LO}$ are the leading order parton level and hadron level cross sections respectively. In the case of DIS $C^{\rm HAD}$ was taken to be the mean of the values from ARIADNE and LEPTO. The corrected cross section is then given by,

$$d\sigma^{\rm hadron}_{\rm NLO} = d\sigma^{\rm parton}_{\rm NLO} / C^{\rm HAD} \tag{5.3}$$

The values of the hadronisation corrections obtained in this way are given in chapter 6.

5.8 Theoretical Uncertainties

The uncertainties on theoretical predictions are difficult to precisely quantify. Three sources of uncertainty have been studied and estimates of their effect made (with typical values given in brackets).

- Uncertainties due to higher order terms beyond NLO were estimated by varying μ by the factors 0.5 and 2.0 (20% at low Q^2 falling to 7% at high Q^2).

- Uncertainties in the hadronisation corrections were estimated as half the spread between the values of $C^{\rm HAD}$ obtained using HERWIG and PYTHIA in the case of photoproduction and ARIADNE and LEPTO in DIS (2−3%).

- Uncertainties arising from the choice of proton PDF and the calculation of α_s were estimated by using the MRST parameterisation in place of CTEQ5M1 [74] ($\sim 5\%$).

These uncertainties were added together in quadrature to give the total uncertainty on the predicted cross section.

5.9 Systematic Uncertainties

A detailed study of the sources contributing to the systematic uncertainties of the measurement was performed. This study includes (a typical value is indicated in parentheses):

- using PYTHIA generator to evaluate the acceptance corrections to the observed dijet distribution (6%);
- using different parameterisations of the photon (GRV-LO and GRS) and proton (MRSA and CTEQ5M1) PDFs for the generation of HERWIG MC samples (2%);
- varying each selection cut by the resolution of the variable at the nominal cut value ($< 2\%$ except for the variation in the E_T^{jet} cut which contributed $7 - 9\%$);
- add the contributions from direct and resolved processes according the the default cross sections as predicted by HERWIG (3%);
- Monte Carlo calorimeter quantity E_T^{jet} varied by $\pm 5\%$. This is the upper limit on the uncertainty in the calorimeter energy scale between data and Monte Carlo [34] (9% at low Q^2 and 6% at high Q^2).

All the above systematics were added in quadrature, except for the jet energy scale uncertainty which is highly correlated and is shown on all plots separately as a shaded band.

Chapter 6

Results and Conclusions

6.1 Comparisons to Leading Order pQCD

6.1.1 Differential Cross sections

The leading order predictions of HERWIG [50] implementing the SaS 2D virtual photon PDF, compared to the measured differential cross section $d^2\sigma/dQ^2dE_T^{jet1}$ is shown in figure 6.1. The predictions are area normalised to the data, with normalisation factors ranging from ~ 1.2 to ~ 3. Two predictions are shown, one for the case when the SaS 2D virtual photon PDF is evolved in Q^2 according to the modified DGLAP approach of [28], and one without this suppression.

For the case where the photon PDF is suppressed with Q^2 the photoproduction measurement ($Q^2 < 1.0$ GeV^2) of $d^2\sigma/dQ^2dE_T^{jet1}$ is well described by the predictions, falling roughly logarithmically with increasing E_T^{jet1}. As Q^2 increases the data exhibits a turnover in the lowest bin of E_T^{jet1} ($7.5 < E_T^{jet1} < 10$ GeV) which is also described well by HERWIG. Generally the measured DIS cross sections fall off more steeply than those predicted by HERWIG. For $Q^2 > 1.5$ GeV^2 only the low E_T^{jet1} data are well described by the predictions. Discrepancies between the data and theory exist in the highest bin of E_T^{jet1} for $Q^2 > 1.5$ GeV^2 becoming more pronounced as Q^2 increases. These observations indicate that the predictions agree with the data only in the presence of a single well defined scale, and that the relationship between the two scales Q^2 and E_T^{jet1} is not well understood.

When the suppression of the photon PDF with increasing Q^2 is switched off the predictions fall off more rapidly as E_T^{jet1} becomes larger than in the case with the suppression switched on. The two predictions are consistent for

$Q^2 < 1.0$ GeV^2, and deviate as Q^2 increases, with the differences between the two models becoming larger at higher Q^2. The predictions generally describe the data well, for $E_T^{jet1} < 17$ GeV and for $E_T^{jet1} > 29$ GeV, however fail in the intermediate region between these values. The differences between data and Monte Carlo in the highest bin of E_T^{jet1} largely disappear at high Q^2 suggesting a greater contribution from resolved processes is required at high Q^2 and high E_T^{jet1}.
Figure 6.2 shows the cross sections $d\sigma/dQ^2d\eta^f$ compared to the LO predictions of HERWIG. Again the photoproduction cross sections are described well by the prediction with the virtual photon PDF suppressed with increasing Q^2, as are those of the BPC measurement, ($0.1 < Q^2 < 0.55$ GeV^2). For $Q^2 > 1.5$ GeV^2 differences are observed, particularly in the most forward bin of η^f where the data lies consistently above the prediction. The forward region is where effects from photon structure are expected to be most significant, and the excess in the data may indicate the need for a larger resolved contribution in this region.
With the suppression of the photon PDF switched off the photoproduction predictions are again consistent and describe the data well. The predictions also describe the BPC data and the region $1.5 < Q^2 < 4.5$ GeV^2 well. For $Q^2 > 4.5$ GeV^2 the predictions no longer describe the data, and differences between the two predictions become more pronounced, particularly for $\eta^f > -0.8$. Whilst the measured cross sections in this region of Q^2 exhibit a rise between $-3.0 < \eta^f < -0.8$, and fall thereafter, the predictions continue to rise with increasing η^f, except in the highest bin of Q^2, ($120.0 < Q^2 < 2000.0$ GeV^2) where the predicted cross section is roughly flat for $\eta^f > -1.8$. Neither of the predictions describe the most forward bin, $\eta^f > -0.8$, with the data lying between the two for $Q^2 > 4.5$ GeV^2.

6.2 Comparisons to Next-to-Leading Order pQCD

The Next-to-leading order (NLO) photoproduction predictions are those of Frixione and Ridolfi [63, 64]. NLO predictions of DIS cross sections were made with the DISASTER++ [72] and DISENT [73] programs, which were found to agree within ±3%. Only the cross sections calculated with DISASTER++ are shown here, because of the larger parameter selection available with this program. Details of the parameters selected for all three of these programs are given in section 5.6. The measurements and the predictions were performed in the region

$E_T^{\text{jet1}} > 7.5\text{GeV}$, $E_T^{\text{jet2}} > 6.5\text{GeV}$, $-3.0 < \eta^{\text{jet}} < 0.0$, $0.2 < y < 0.55$ and $0.0 < Q^2 < 2000.0\text{GeV}^2$ in the photon-proton centre of mass frame.

6.2.1 Differential Cross sections

Figures 6.3 and 6.4 show the differential dijet cross section, $d\sigma/dQ^2$, split into direct enhanced ($x_\gamma^{\text{OBS}} \geq 0.75$) and resolved enhanced ($x_\gamma^{\text{OBS}} < 0.75$) regions, as well as the total, in bins of Q^2. The measurements cover a wide Q^2 range including the low Q^2 transition region from photoproduction to DIS. The data points are plotted at the median value of Q^2 for each bin determined from a Monte Carlo study using the HERWIG MC generator.

The total measured cross sections are observed to fall by approximately five orders of magnitude over the whole Q^2 range. Figure 6.3 also shows the NLO predictions of Frixione and Ridolfi, with $\mu_F^2 = \mu_R^2 = (p_T^{\text{JET}})^2$ (photoproduction) and those of DISASTER++ with $\mu_F^2 = \mu_R^2 = Q^2 + (p_T^{\text{JET}})^2$ (DIS). The factor p_T^{JET} is defined here as the mean of the parton transverse momenta, although other definitions are valid (e.g. highest p_T parton). In photoproduction the total cross section prediction is in good agreement with the measurement. At higher Q^2 (i.e. in DIS) the NLO predictions describe the shape of the measured total cross section well, however underestimate the magnitude by around 30%. In figure 6.4 the measured DIS cross sections are compared to the prediction of DISASTER++ with $\mu_F^2 = \mu_R^2 = Q^2$. The photoproduction measurement was omitted, as clearly Q^2 does not represent a hard enough scale to perform perturbative calculations reliably. The calculations are generally in good agreement, although large theoretical uncertainties, particularly for $Q^2 < 100$ GeV^2, are present. For $Q^2 < 100$ GeV^2 the predicted cross sections are heavily scale dependent due to the softness of the scale Q^2 relative to the square of the transverse momentum of the partons p_T^2. The large uncertainties at low Q^2 are drastically reduced when using the scale $\mu_F^2 = \mu_R^2 = Q^2 + (p_T^{\text{JET}})^2$ as in figure 6.3. At low Q^2 the absolute value of the NLO cross section overestimates the measurement by $\approx 20\%$ when using Q^2 as the renormalisation and factorisation scales, and tends towards the prediction with $\mu_F^2 = \mu_R^2 = Q^2 + (p_T^{\text{JET}})^2$ as Q^2 increases.

The cross section for $x_\gamma^{\text{OBS}} \geq 0.75$ falls less rapidly than the total as direct photon processes become increasingly dominant at high Q^2. The NLO prediction with $\mu_F^2 = \mu_R^2 = Q^2 + (p_T^{\text{JET}})^2$ describes the measured cross section well in both photoproduction and DIS. The calculation shown in figure 6.4 describes the data

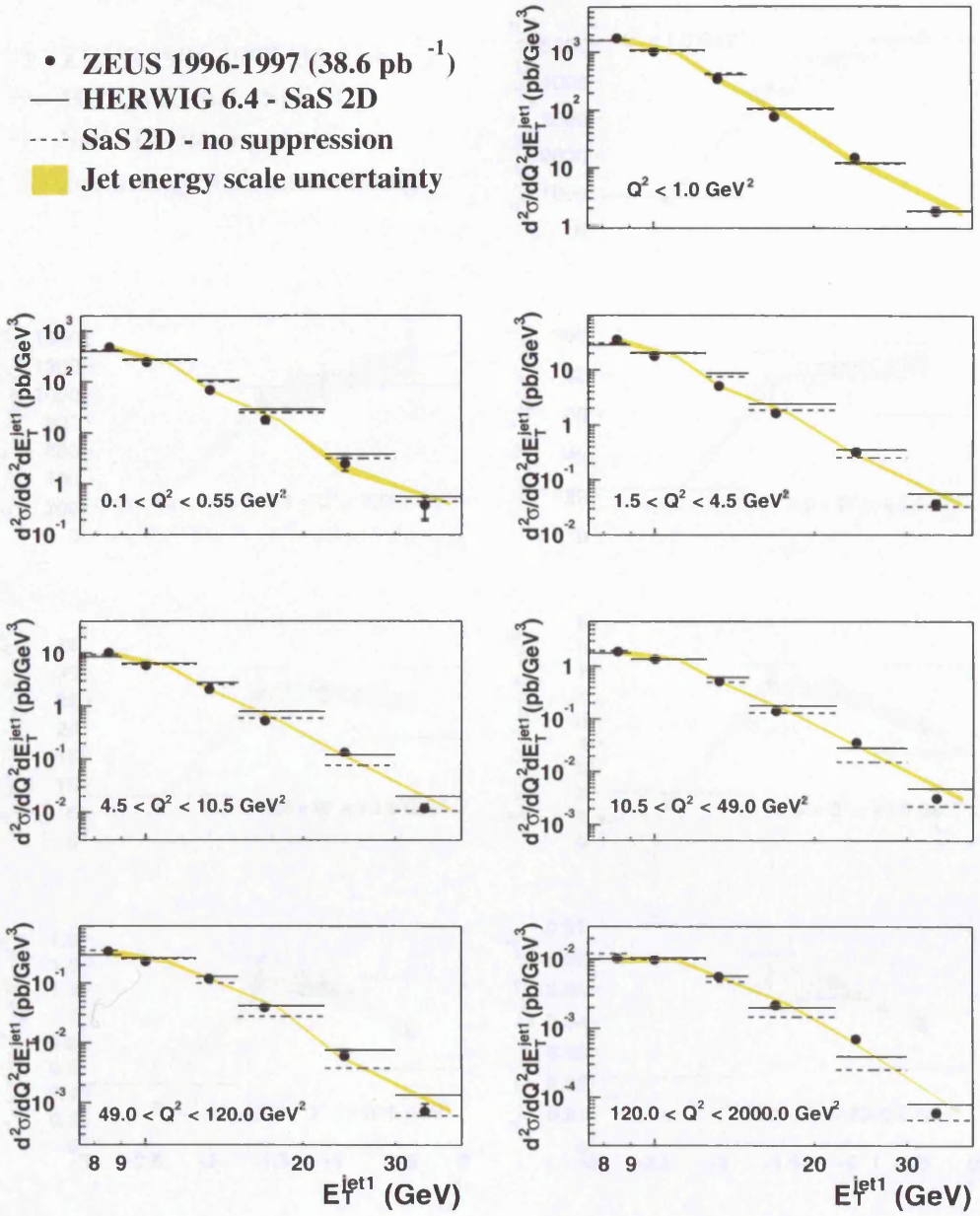

Figure 6.1: *Measured dijet cross-section $d^2\sigma/dQ^2dE_T^{jet1}$ (dots). The inner vertical bars represent the statistical uncertainties of the data, and the outer bars show the statistical and systematic uncertainties added in quadrature, except for that associated with the uncertainty in the absolute energy scale of the jets (shaded band). The data are compared to the area normalised predictions of the leading order parton shower Monte Carlo HERWIG, implementing the SaS 2D virtual photon PDF suppressed with increasing Q^2 (solid lines), and with the suppression switched off (dashed lines).*

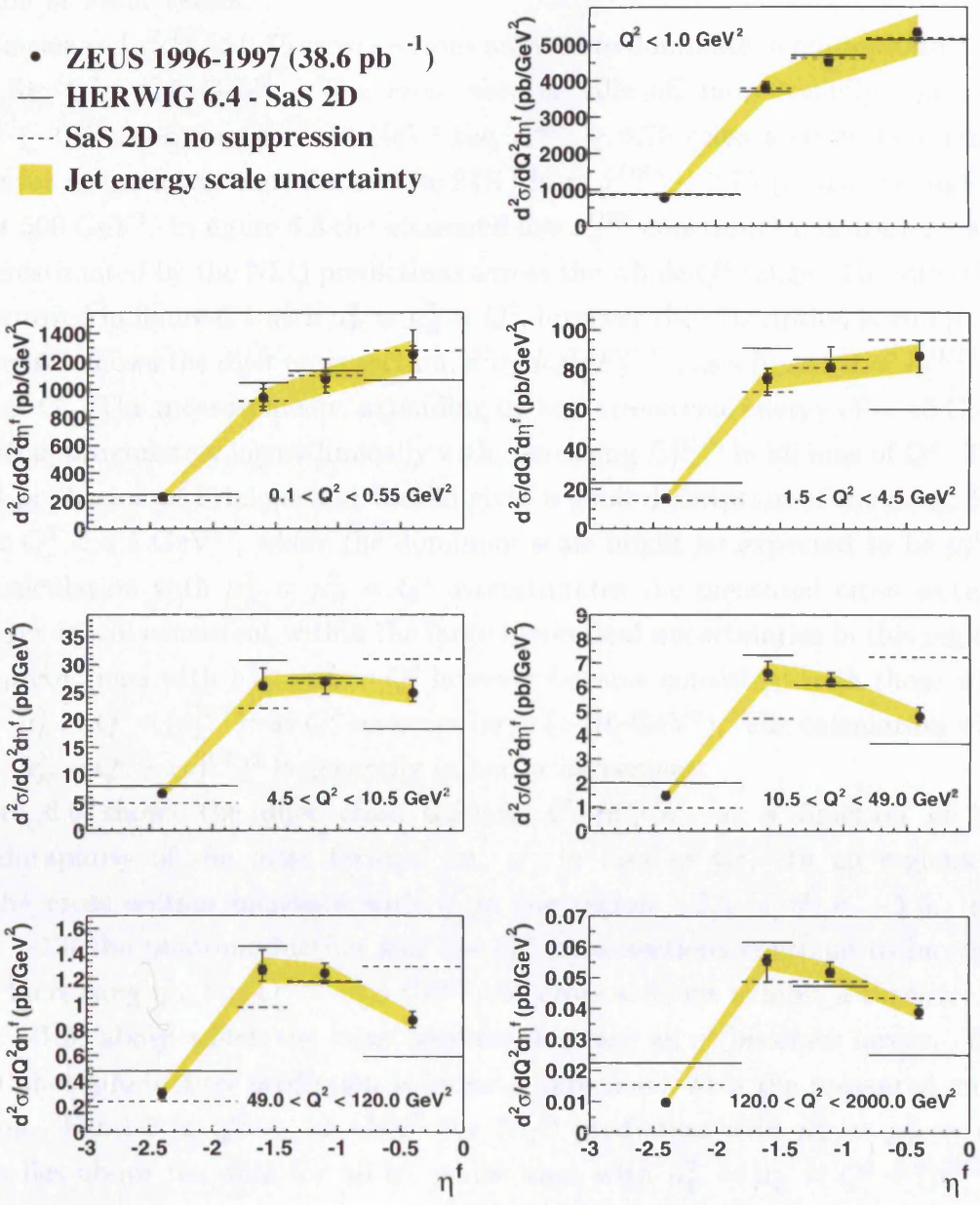

Figure 6.2: *Measured dijet cross-section $d^2\sigma/dQ^2d\eta^{\mathrm{f}}$ (dots). The inner vertical bars represent the statistical uncertainties of the data, and the outer bars show the statistical and systematic uncertainties added in quadrature, except for that associated with the uncertainty in the absolute energy scale of the jets (shaded band). The data are compared to the area normalised predictions of the leading order parton shower Monte Carlo HERWIG, implementing the SaS 2D virtual photon PDF suppressed with increasing Q^2 (solid lines), and with the suppression switched off (dashed lines).*

well for $Q^2 > 10$ GeV^2, however significantly overestimates the measured cross section at lower values.
The measured $x_\gamma^{\rm OBS} < 0.75$ cross sections are seen to dominate in photoproduction and for $Q^2 < 5$ GeV^2. The cross section falls off more rapidly than for $x_\gamma^{\rm OBS} \geq 0.75$, and for $Q^2 > 10$ GeV^2 the $x_\gamma^{\rm OBS} \geq 0.75$ cross section dominates. However a significant contribution ($\approx 24\%$) from $x_\gamma^{\rm OBS} < 0.75$ persists as high as $Q^2 \approx 500$ GeV^2. In figure 6.3 the measured low $x_\gamma^{\rm OBS}$ contribution is dramatically underestimated by the NLO predictions across the whole Q^2 range. The situation is improved in figure 6.4 with $\mu_F^2 = \mu_R^2 = Q^2$, however the description is still poor. Figure 6.5 shows the dijet cross section, $d^2\sigma/dQ^2dE_T^{\rm JET1}$, as a function of $E_T^{\rm JET1}$ in bins of Q^2. The measurements, extending up to a transverse energy of ≈ 40 GeV, fall off approximately logarithmically with increasing $E_T^{\rm JET1}$ in all bins of Q^2. The NLO prediction of Frixione and Ridolfi gives a good description of the data. For $1.5 < Q^2 < 4.5$ GeV^2 , where the dominant scale might be expected to be $p_T^{\rm JET}$, the calculation with $\mu_F^2 = \mu_R^2 = Q^2$ overestimates the measured cross section, however is still consistent within the large theoretical uncertainties in this region. The predictions with $\mu_F^2 = \mu_R^2 = Q^2$ however become consistent with those with $\mu_F^2 = \mu_R^2 = Q^2 + (p_T^{\rm JET})^2$ as Q^2 becomes large (> 10 GeV^2). The calculation with $\mu_F^2 = \mu_R^2 = Q^2 + (p_T^{\rm JET})^2$ is generally in better agreement.
Figure 6.6 shows the dijet cross section, $d^2\sigma/dQ^2\eta^{\rm f}$, as a function of the pseudorapidity of the most forward jet, $\eta^{\rm f}$, in bins of Q^2. In all regions of Q^2 the cross section increases with $\eta^{\rm f}$ in the region $-2.5 < \eta^{\rm f} < -1.5$. For $\eta^{\rm f} > -1.5$ the photoproduction and low Q^2 cross sections continue to increase with increasing $\eta^{\rm f}$. For $Q^2 > 10.5$ GeV^2 the cross sections exhibit a turnover at $\eta^{\rm f} \approx -1.5$, above which the cross sections decrease as $\eta^{\rm f}$ becomes larger. The NLO photoproduction prediction is in good agreement with the measured cross section. For $1.5 < Q^2 < 4.5$ GeV^2 the NLO prediction with $\mu_F^2 = \mu_R^2 = Q^2$ again lies above the data for all $\eta^{\rm f}$, whilst that with $\mu_F^2 = \mu_R^2 = Q^2 + (p_T^{\rm JET})^2$ underestimates the measurement in the forward direction, the data lying between the two. As Q^2 increases the two predictions converge, although both still lie below the data at high $\eta^{\rm f}$.

6.3 Ratio

The Q^2 dependence of the direct- and resolved-enhanced components of the dijet cross section was studied in more detail using the ratio of cross sections

for low ($x_\gamma^{\rm OBS} < 0.75$) to high ($x_\gamma^{\rm OBS} \geq 0.75$) $x_\gamma^{\rm OBS}$, defined in equation 4.1. Many experimental and theoretical uncertainties cancel in this ratio, so that the presence of a resolved contribution can be investigated at higher precision than in the individual cross section discussed so far.

Figures 6.7 and 6.8 show the ratio R as a function of Q^2 in three different regions of $\overline{E_{\rm T}}^2$, where $\overline{E_{\rm T}}^2$ is defined as,

$$\overline{E_{\rm T}}^2 = \left(\frac{E_{\rm T}^{\rm JET1} + E_{\rm T}^{\rm JET2}}{2}\right)^2 . \tag{6.1}$$

The Q^2 dependence of the data is stronger at low $\overline{E_{\rm T}}^2$ than at higher $\overline{E_{\rm T}}^2$, implying that the low $x_\gamma^{\rm OBS}$ component is suppressed at low Q^2 with increasing $\overline{E_{\rm T}}^2$ and, at low $\overline{E_{\rm T}}^2$ as Q^2 increases.

Figure 6.7 shows the leading order prediction of HERWIG 6.4, implementing the SaS2D virtual photon structure function, compared to the data. When the SaS2D structure function is suppressed with increasing virtuality, Q^2, the prediction reproduces the suppression of the low $x_\gamma^{\rm OBS}$ contribution in the data, reasonably well. When the suppression is switched off the predicted ratio is relatively flat with increasing Q^2.

The NLO calculations are compared to the data in figure 6.8. The photoproduction prediction is in reasonable agreement with the data for all $\overline{E_{\rm T}}^2$. The NLO prediction using the GRV photon PDFs are nearer to the data than those using AFG which lie below the data. The DIS predictions show some suppression of the ratio with increasing, Q^2, but generally underestimate the ratio.

6.4 Summary and Conclusions

Dijet cross sections have been measured in the range $0.0 < Q^2 < 2000$ GeV^2, $0.2 < y < 0.55$, $-3 < \eta^{\rm f} < 0$, $E_{\rm T}^{\rm jet1} > 7.5$ GeV and $E_{\rm T}^{\rm jet1} > 6.5$ GeV as a function of Q^2, $E_{\rm T}^{\rm jet1}$ and $\eta^{\rm f}$ in the photon-proton centre-of-mass frame.

The measurements are qualitatively described by leading order QCD models with parton showering, which introduce a partonic structure to the virtual photon which is suppressed with increasing Q^2. The predicted cross sections $d^2\sigma/dQ^2dE_{\rm T}^{\rm jet1}$ generally describe the data well for low Q^2 ($Q^2 < 1.0$ GeV^2) and low $E_{\rm T}^{\rm jet1}$, however differences exist for higher values of Q^2 and $E_{\rm T}^{\rm jet1}$ where both scales are expected to play a role. The cross sections $d^2\sigma/dQ^2d\eta^{\rm f}$ exhibit an

excess in the data in the forward region for $Q^2 > 1.5$ GeV^2, where the effects of resolved photon interactions are expected.

For the case when the virtual photon PDF is not evolved in Q^2 using the modified DGLAP approach [28] the predicted cross sections $d^2\sigma/dQ^2dE_T^{jet1}$ are in better agreement with the data at high Q^2 and high E_T^{jet1} than with the suppression switched on, however fail to describe the data in the region $17 < E_T^{jet1} < 29$ GeV. The cross sections $d^2\sigma/dQ^2d\eta^f$ are well described by the prediction for $Q^2 < 4.5$ GeV^2 however do not describe the data for $Q^2 > 4.5$ GeV^2. The data when compared to these two models suggest the need for a greater contribution from resolved processes at high Q^2 and high E_T^{jet1} than is currently calculated by leading order models. The data also support the notion of a virtual photon PDF suppressed with increasing Q^2. Future fits to these data have the potential to significantly constrain such parton densities.

The currently available NLO QCD calculations have large uncertainties, especially at low Q^2 where the presence of a resolved photon contribution is expected. In spite of this the measured cross sections $d\sigma/dQ^2$ shown in figures 6.3 and 6.4 (table 6.1) suggest that a partonic structure may be required as high as $Q^2 \approx 500$GeV^2 to reconcile the excess in the measured low x_γ^{OBS} cross sections. This conclusion is strengthened further when considering figure 6.6 (tables 6.5 and 6.6). In the backward direction ($\eta^f < -1.5$) the prediction is consistent with the measurement, whilst for $\eta^f > -1.5$, where a larger contribution from the resolved photon is expected, the prediction lies below the data. The photoproduction prediction, which implements such a photon structure function is however consistent with the measurement.

Sensitivity to the resolved photon contribution was enhanced using the ratio of low to high x_γ^{OBS} cross sections (table 11.8). The measured ratio is observed to fall rapidly with increasing Q^2, especially at low values of $\overline{E_T}^2$. The NLO QCD predictions generally underestimate the measured ratio. Differences are also observed between the photoproduction NLO predictions when using the AFG photon PDF in place of GRV. These data slightly favour the GRV photon PDF.

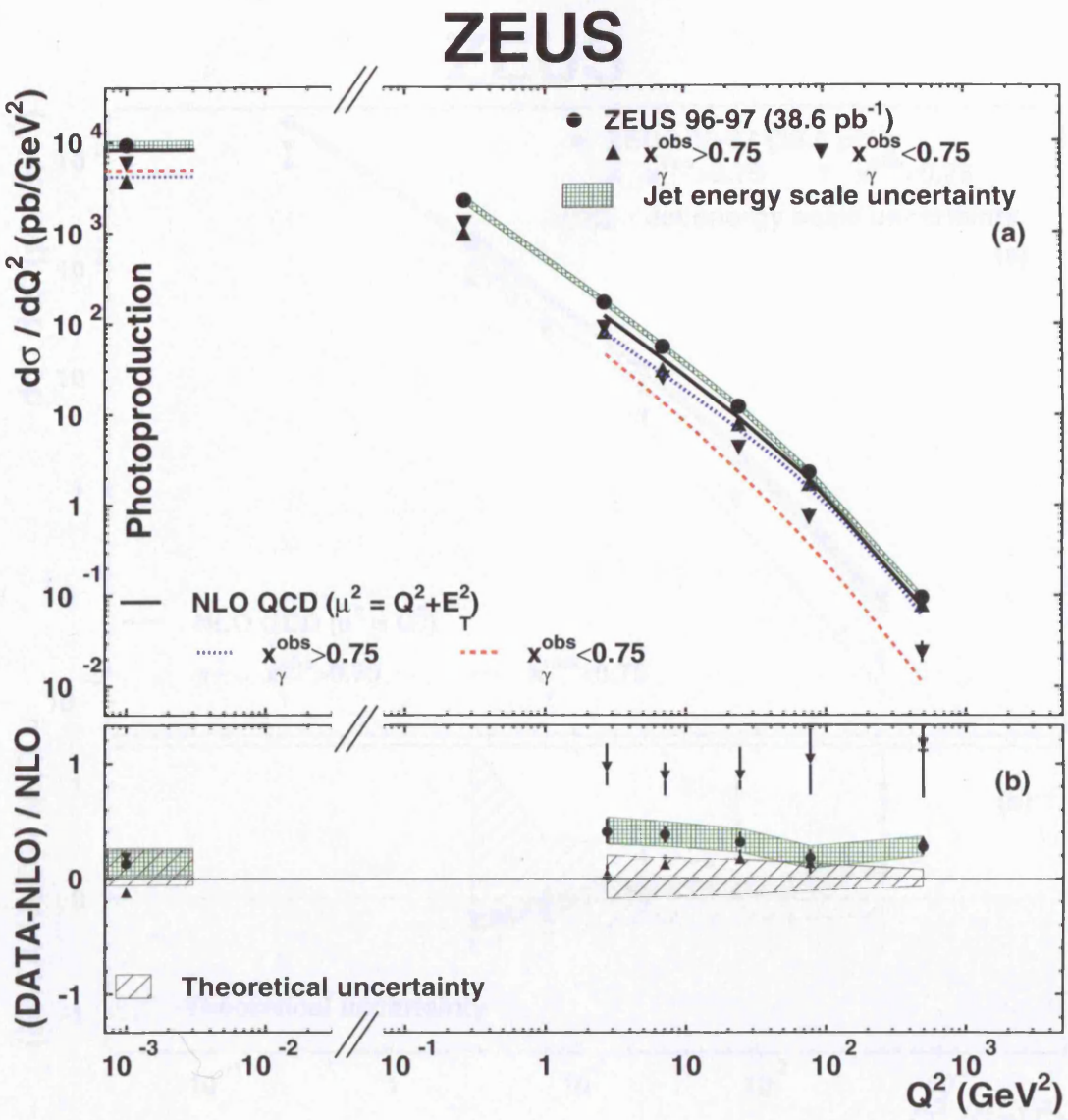

Figure 6.3: *(a) Measured dijet cross-sections $d\sigma/dQ^2$ for $x_\gamma^{\rm OBS} > 0.75$ (upwards triangles) $d\sigma/dQ^2$ for $x_\gamma^{\rm OBS} < 0.75$ (downwards triangles) and $d\sigma/dQ^2$ for the whole $x_\gamma^{\rm OBS}$ region (black dots). The inner vertical bars represent the statistical uncertainties of the data, and the outer bars show the statistical and systematic uncertainties added in quadrature, except for that associated with the uncertainty in the absolute energy scale of the jets (shaded band). The NLO QCD calculations of DISASTER++ $(\mu^2 = Q^2 + (E_T^{jet})^2)$ and of Frixione and Ridolfi $(\mu^2 = (E_T^{jet})^2)$ are shown for each of the cross-sections. (b) Relative difference of the measured dijet cross-sections $d\sigma/dQ^2$ to the DISASTER++ $(\mu^2 = Q^2 + (E_T^{jet})^2)$ and Frixione and Ridolfi $(\mu^2 = (E_T^{jet})^2)$ calculations. The hatched band shows the theoretical uncertainty of the calculations.*

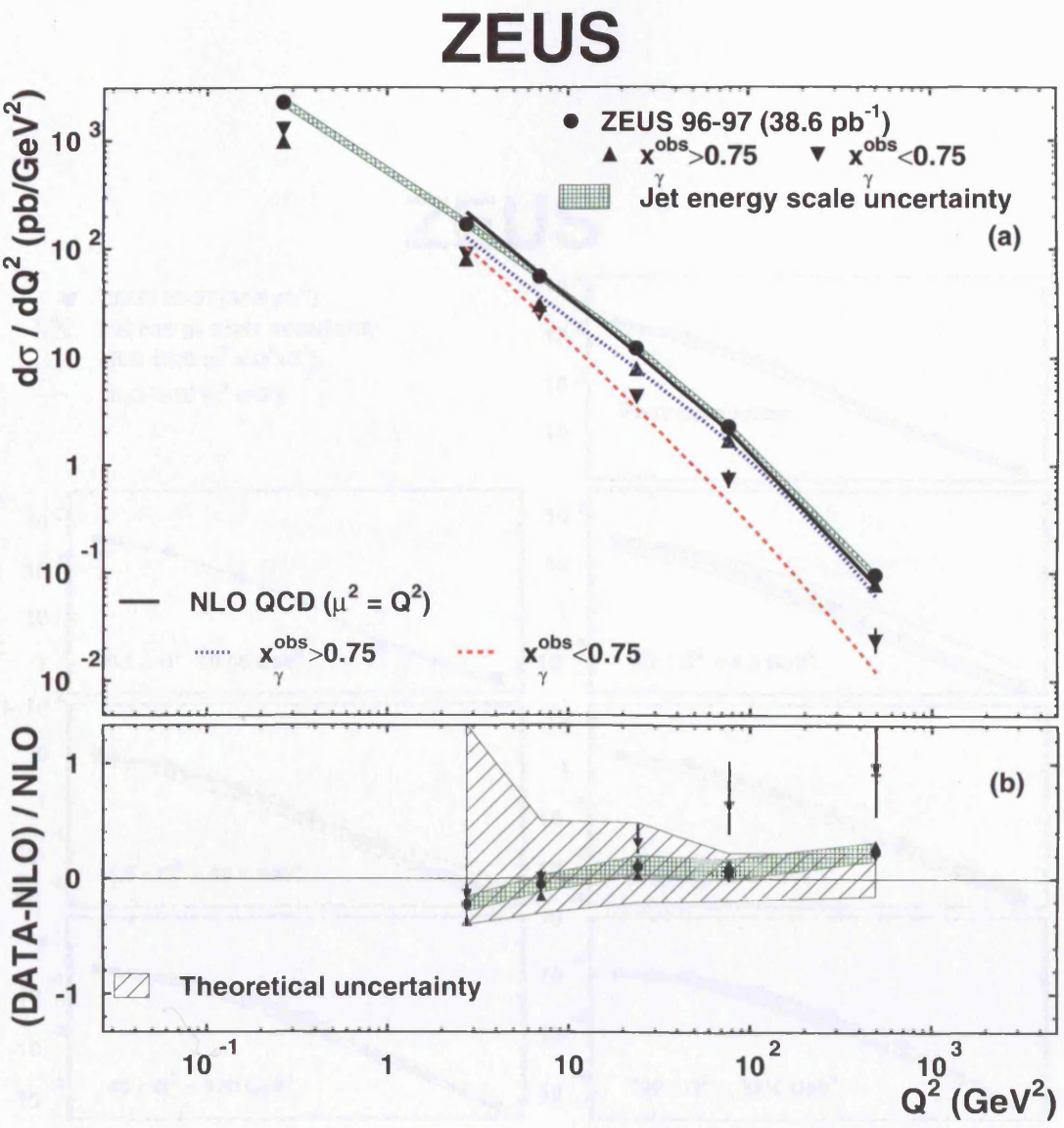

Figure 6.4: *(a) Measured dijet cross-sections $d\sigma/dQ^2$ for $x_\gamma^{\rm OBS} > 0.75$ (upwards triangles) $d\sigma/dQ^2$ for $x_\gamma^{\rm OBS} < 0.75$ (downwards triangles) and $d\sigma/dQ^2$ for the whole $x_\gamma^{\rm OBS}$ region (black dots). The inner vertical bars represent the statistical uncertainties of the data, and the outer bars show the statistical and systematic uncertainties added in quadrature, except for that associated with the uncertainty in the absolute energy scale of the jets (shaded band). The NLO QCD calculations of DISASTER++ $(\mu^2 = Q^2$ are shown for each of the cross-sections. (b) Relative difference of the measured dijet cross-sections $d\sigma/dQ^2$ to the DISASTER++ calculation with $(\mu^2 = Q^2$. The hatched band shows the theoretical uncertainty of the calculations.*

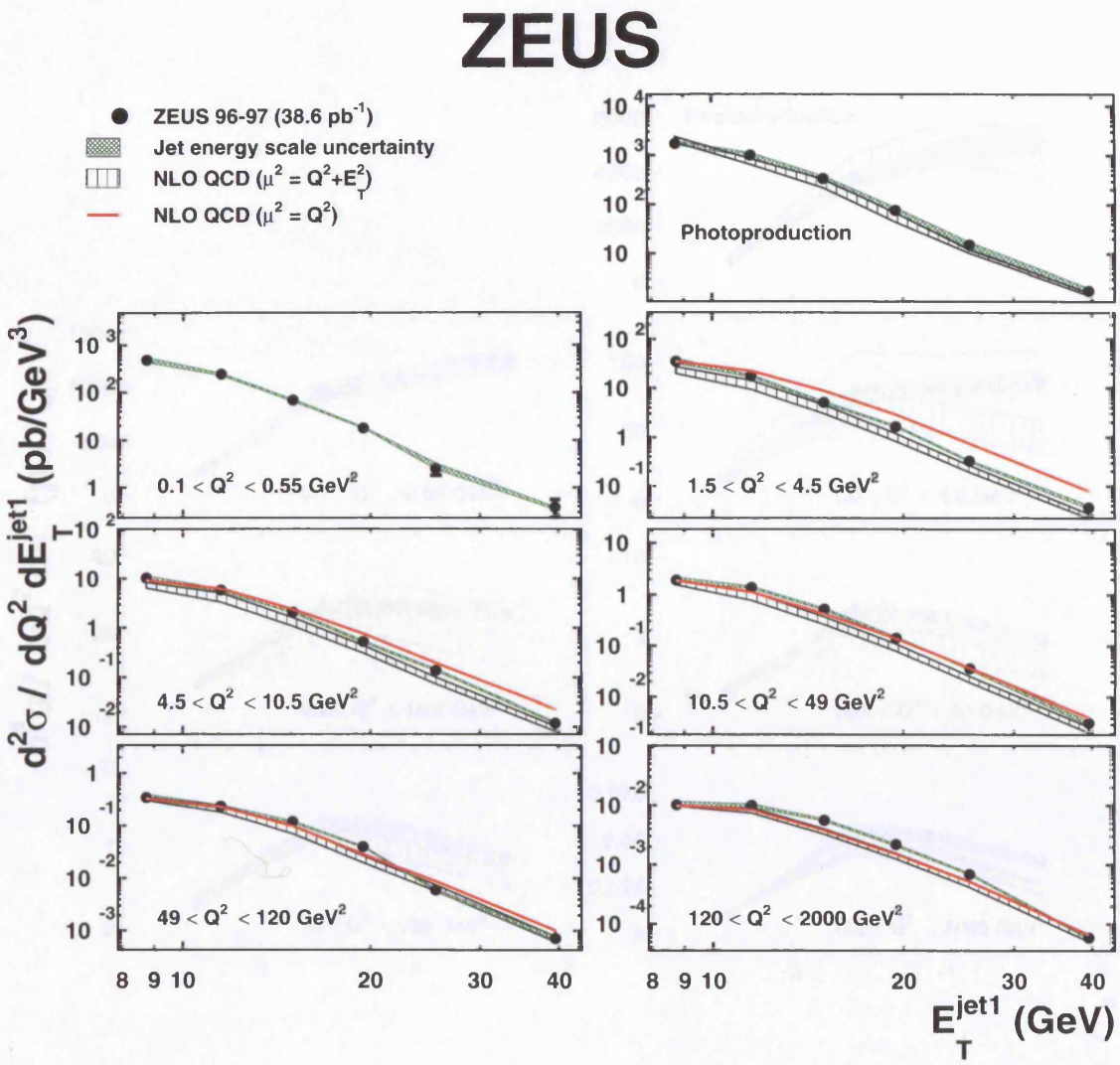

Figure 6.5: *Measured dijet cross-section $d^2\sigma/dQ^2dE_T^{jet1}$ (dots). The NLO QCD calculations of DISASTER++ with $\mu^2 = Q^2 + (E_T^{jet})^2$ and $\mu^2 = Q^2$ as well as Frixione and Ridolfi for the photoproduction region are also shown. Other details as in caption to figure 6.3.*

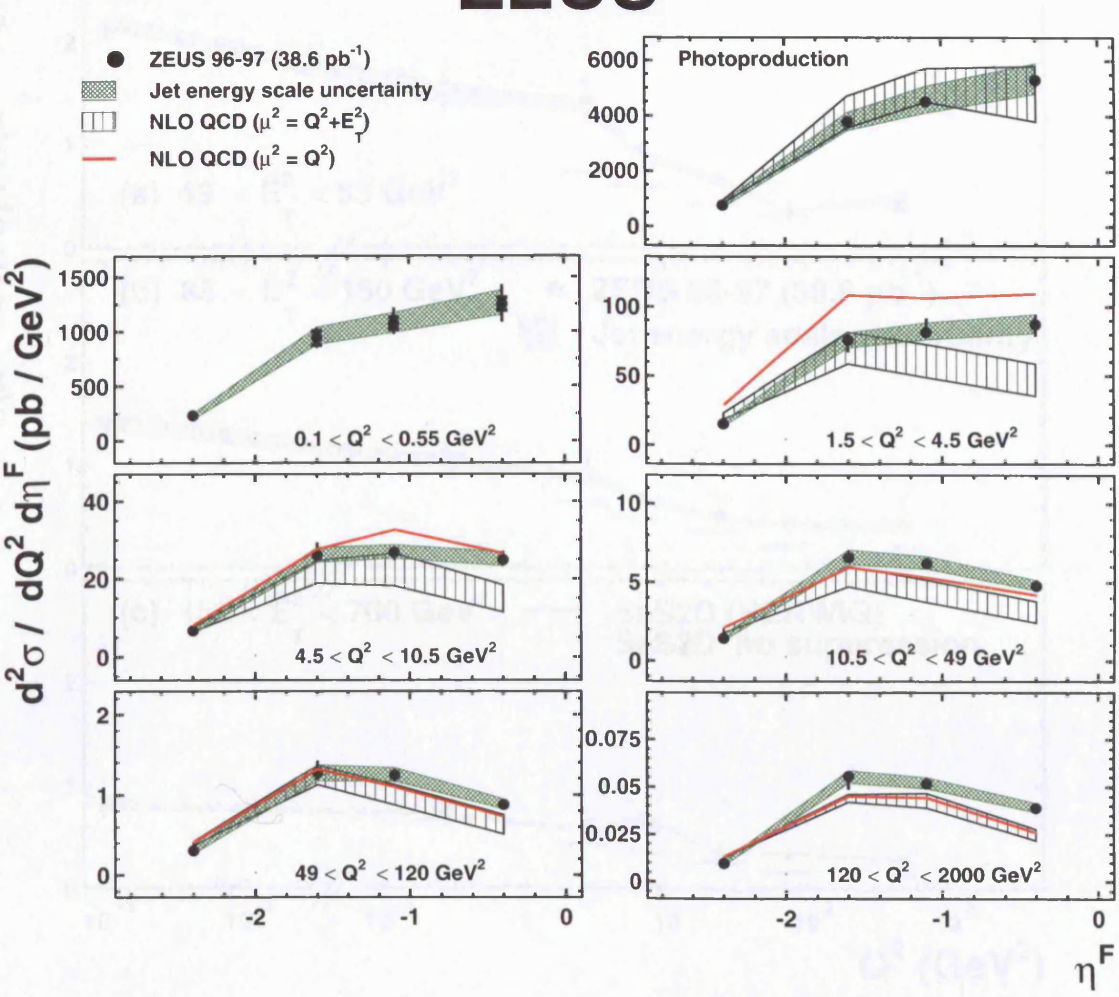

Figure 6.6: *Measured dijet cross-section $d^2\sigma/dQ^2d\eta^f$ (dots). The NLO QCD calculations of DISASTER++ with $\mu^2 = Q^2 + (E_T^{jet})^2$ and $\mu^2 = Q^2$ as well as Frixione and Ridolfi for the photoproduction region are also shown. Other details as in caption to figure 6.3.*

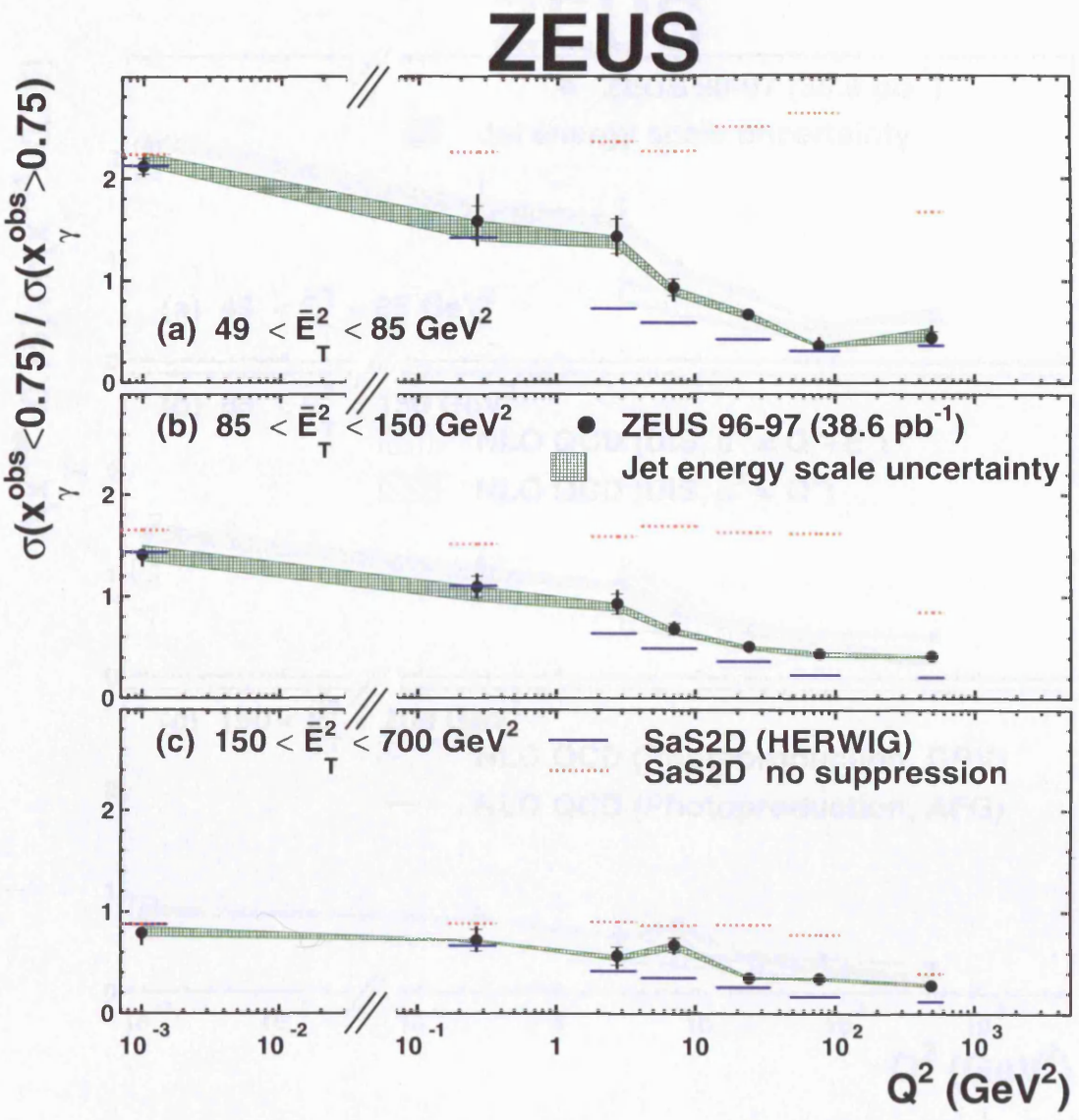

Figure 6.7: *Measured ratio* $R = \sigma(x_\gamma^{\rm OBS} < 0.75)/\sigma(x_\gamma^{\rm OBS} > 0.75)$ *as a function of* Q^2 *in different regions of* $\overline{E_T}^2$ *(black dots). The LO calculations of HERWIG using the SaS2D photon PDFs are also shown. Parameters from the JetWeb fit 692 have been used for the generation of HERWIG. Other details as in caption to figure 6.3.*

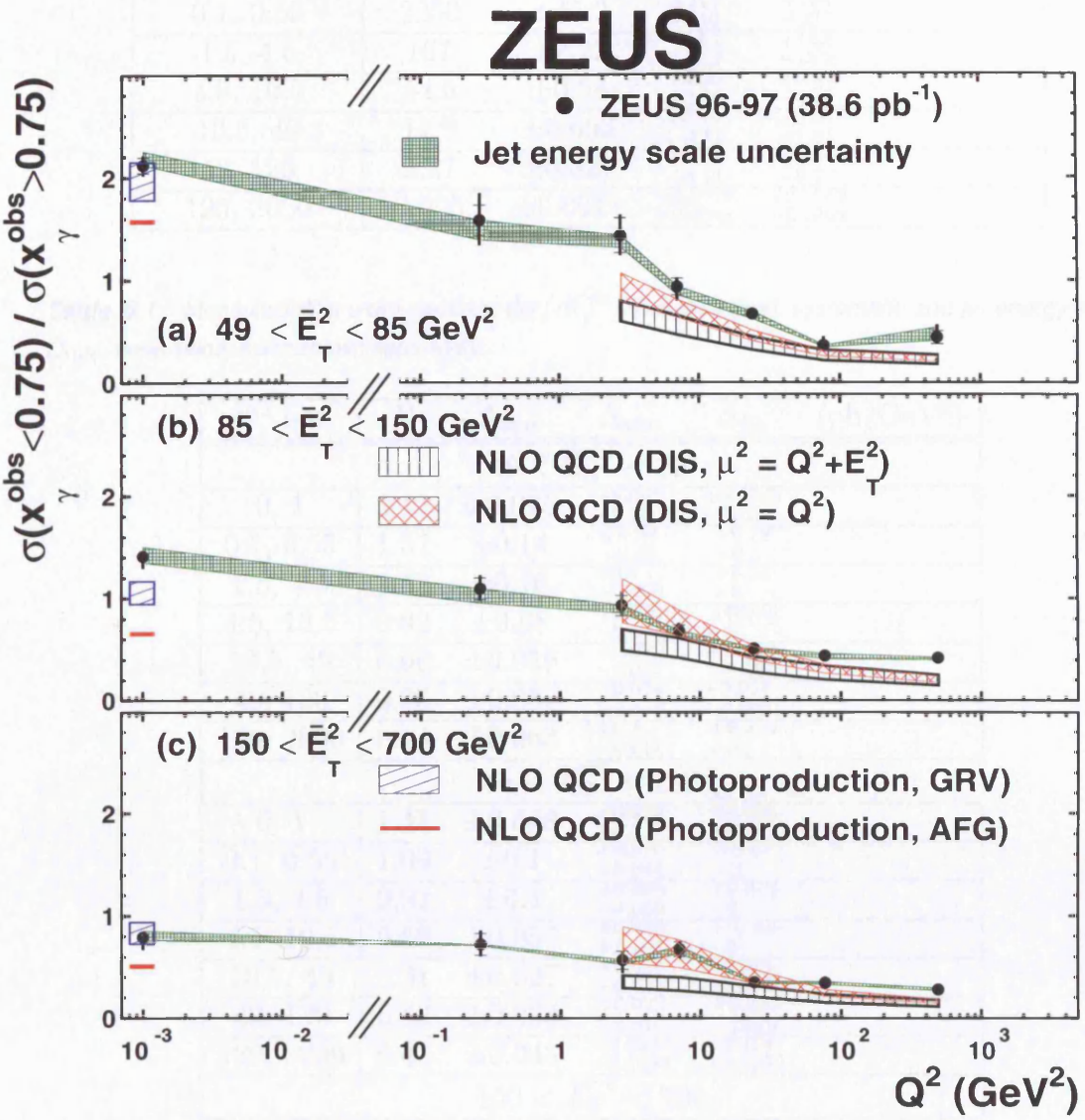

Figure 6.8: *Measured ratio* $R = \sigma(x_\gamma^{\rm OBS} < 0.75)/\sigma(x_\gamma^{\rm OBS} > 0.75)$ *as a function of* Q^2 *in different regions of* $\overline{E_T}^2$ *(black dots). The NLO QCD calculations of DISASTER++ with* $\mu^2 = Q^2 + (E_T^{jet})^2$ *and* $\mu^2 = Q^2$ *as well as the Frixione and Ridolfi predictions for the photoproduction region are also shown. The hatched bands represent the theoretical uncertainties. Other details as in caption to figure 6.3.*

Q^2 bin (GeV^2)	$d\sigma/dQ^2$	$\Delta_{\rm stat}$	$\Delta_{\rm syst}$	$\Delta_{\rm ES}$ (pb/GeV^2)
0, 1	9280	$\pm$113	$^{+102}_{-69.3}$	$^{+917}_{-1100}$
0.1, 0.55	2250	$\pm$45.2	$^{+215}_{-210}$	$^{+194}_{-227}$
1.5, 4.5	167	$\pm$2.22	$^{+14.1}_{-11.9}$	$^{+12.5}_{-15.2}$
4.5, 10.5	54.5	$\pm$0.54	$^{+3.05}_{-2.76}$	$^{+3.94}_{-4.48}$
10.5, 49	11.9	$\pm$0.093	$^{+0.79}_{-0.32}$	$^{+0.81}_{-1.01}$
49, 120	2.27	$\pm$0.027	$^{+0.14}_{-0.13}$	$^{+0.17}_{-0.2}$
120, 2000	0.095	$\pm$0.0011	$^{+0.0019}_{-0.0048}$	$^{+0.0059}_{-0.0068}$

Table 6.1: *Measured dijet cross-sections $d\sigma/dQ^2$. The statistical, systematic and jet energy scale, $\Delta_{\rm ES}$, uncertainties are shown separately.*

Q^2 bin	R	$\Delta_{\rm stat}$	$\Delta_{\rm syst}$	$\Delta_{\rm ES}$ (pb/GeV^2)
$49 < \overline{E_{\rm T}}^2 < 85$				
0, 1	2.12	$\pm$0.075	$^{+0.057}_{-0.066}$	$^{+0.0026}_{-0.12}$
0.1, 0.55	1.57	$\pm$0.14	$^{+0.22}_{-0.19}$	$^{+0.19}_{-0}$
1.5, 4.5	1.42	$\pm$0.16	$^{+0.1}_{-0.096}$	$^{+0.11}_{-0}$
4.5, 10.5	0.92	$\pm$0.08	$^{+0.035}_{-0.1}$	$^{+0.078}_{-0}$
10.5, 49	0.66	$\pm$0.039	$^{+0.029}_{-0.034}$	$^{+0.049}_{-0.021}$
49, 120	0.35	$\pm$0.037	$^{+0.079}_{-0.018}$	$^{+0.014}_{-0.0021}$
120, 2000	0.44	$\pm$0.063	$^{+0.1}_{-0.011}$	$^{+0.035}_{-0.1}$
$85 < \overline{E_{\rm T}}^2 < 150$				
0, 1	1.41	$\pm$0.048	$^{+0.016}_{-0.1}$	$^{+0.065}_{-0.086}$
0.1, 0.55	1.09	$\pm$0.1	$^{+0.079}_{-0.044}$	$^{+0.13}_{-0}$
1.5, 4.5	0.92	$\pm$0.1	$^{+0.095}_{-0.032}$	$^{+0.073}_{-0}$
4.5, 10.5	0.68	$\pm$0.057	$^{+0.052}_{-0.026}$	$^{+0.053}_{-0}$
10.5, 49	0.51	$\pm$0.027	$^{+0.044}_{-0.023}$	$^{+0.033}_{-0.0036}$
49, 120	0.43	$\pm$0.038	$^{+0.029}_{-0.015}$	$^{+0.029}_{-0.019}$
120, 2000	0.41	$\pm$0.048	$^{+0.033}_{-0.0084}$	$^{+0.018}_{-0.0062}$
$150 < \overline{E_{\rm T}}^2 < 700$				
0, 1	0.78	$\pm$0.032	$^{+0.0022}_{-0.11}$	$^{+0.028}_{-0.06}$
0.1, 0.55	0.72	$\pm$0.1	$^{+0.086}_{-0.049}$	$^{+0.018}_{-0}$
1.5, 4.5	0.56	$\pm$0.088	$^{+0.015}_{-0.088}$	$^{+0.042}_{-0}$
4.5, 10.5	0.67	$\pm$0.07	$^{+0.03}_{-0.059}$	$^{+0.043}_{-0.028}$
10.5, 49	0.34	$\pm$0.026	$^{+0.015}_{-0.0057}$	$^{+0.0092}_{-0.0098}$
49, 120	0.34	$\pm$0.039	$^{+0.046}_{-0.049}$	$^{+0.016}_{-0.0068}$
120, 2000	0.28	$\pm$0.046	$^{+0.019}_{-0.0052}$	$^{+0.014}_{-0.011}$

Table 6.2: *Measured ratio $R = \sigma(x_\gamma^{\rm OBS} < 0.75)/\sigma(x_\gamma^{\rm OBS} > 0.75)$ as a function of Q^2 in different regions of $\overline{E_{\rm T}}^2$.*

E_T^{jet1} bin (GeV)	$d^2\sigma/dE_T^{\text{jet1}}dQ^2$	Δ_{stat}	Δ_{syst}	Δ_{ES} (pb/GeV)
$0 < Q^2 < 1$				
7.5, 10	1740	± 34.8	$^{+20.9}_{-84.3}$	$^{+146}_{-189}$
10, 13	1010	± 20.4	$^{+11.3}_{-24.8}$	$^{+90}_{-118}$
13, 17	337	± 8.5	$^{+21.5}_{-8.51}$	$^{+35.7}_{-39.9}$
17, 22	76.4	± 3.22	$^{+3.9}_{-3.14}$	$^{+9.45}_{-9.6}$
22, 29	15	± 1.25	$^{+0.1}_{-0.085}$	$^{+1.96}_{-2.03}$
29, 50	1.75	± 0.092	$^{+0.37}_{-0.16}$	$^{+0.22}_{-0.23}$
$0.1 < Q^2 < 0.55$				
7.5, 10	484	± 22.6	$^{+24.3}_{-75.5}$	$^{+53.6}_{-70.3}$
10, 13	243	± 12.1	$^{+6.81}_{-14.7}$	$^{+16.8}_{-15}$
13, 17	68.7	± 4.91	$^{+4.92}_{-1.38}$	$^{+4.22}_{-3.53}$
17, 22	17.9	± 2.19	$^{+1.33}_{-1.76}$	$^{+0.48}_{-0.94}$
22, 29	2.49	± 0.67	$^{+0.39}_{-0.29}$	$^{+0.13}_{-0.69}$
29, 50	0.38	± 0.17	$^{+0.071}_{-0.083}$	$^{+0.048}_{-0}$
$1.5 < Q^2 < 4.5$				
7.5, 10	35.2	± 0.72	$^{+2.46}_{-1.31}$	$^{+3.44}_{-4.71}$
10, 13	17.6	± 0.41	$^{+0.96}_{-1}$	$^{+0.96}_{-1.12}$
13, 17	5.09	± 0.16	$^{+0.52}_{-0.044}$	$^{+0.36}_{-0.26}$
17, 22	1.64	± 0.091	$^{+0.032}_{-0.13}$	$^{+0.057}_{-0.086}$
22, 29	0.32	± 0.033	$^{+0.0087}_{-0.035}$	$^{+0.015}_{-0.01}$
29, 50	0.037	± 0.0063	$^{+0.0023}_{-0.0049}$	$^{+0.0024}_{-0.0035}$
$4.5 < Q^2 < 10.5$				
7.5, 10	10.2	± 0.16	$^{+0.23}_{-1.32}$	$^{+1}_{-1.21}$
10, 13	5.86	± 0.1	$^{+0.25}_{-0.16}$	$^{+0.34}_{-0.37}$
13, 17	2.08	± 0.048	$^{+0.043}_{-0.061}$	$^{+0.11}_{-0.12}$
17, 22	0.52	± 0.02	$^{+0.0084}_{-0.033}$	$^{+0.034}_{-0.019}$
22, 29	0.13	± 0.0097	$^{+0.0071}_{-0.0078}$	$^{+0.0053}_{-0.011}$
29, 50	0.011	± 0.0015	$^{+0.002}_{-0.00084}$	$^{+0.00039}_{-0.00059}$

Table 6.3: *Measured dijet cross-section* $d^2\sigma/dQ^2dE_T^{\text{jet1}}$.

E_T^{jet1} bin (GeV)	$d^2\sigma/dE_T^{\text{jet1}}dQ^2$	Δ_{stat}	Δ_{syst}	Δ_{ES} (pb/GeV)
$10.5 < Q^2 < 49$				
7.5, 10	1.9	± 0.024	$^{+0.15}_{-0.059}$	$^{+0.17}_{-0.25}$
10, 13	1.36	± 0.018	$^{+0.057}_{-0.041}$	$^{+0.091}_{-0.082}$
13, 17	0.51	± 0.0091	$^{+0.024}_{-0.013}$	$^{+0.028}_{-0.025}$
17, 22	0.14	± 0.0041	$^{+0.0029}_{-0.007}$	$^{+0.0031}_{-0.0086}$
22, 29	0.036	± 0.0018	$^{+0.0014}_{-0.0021}$	$^{+0.0017}_{-0.0012}$
29, 50	0.0031	± 0.00031	$^{+0.00018}_{-0.00011}$	$^{+0.00028}_{-0.00034}$
$49 < Q^2 < 120$				
7.5, 10	0.34	± 0.0071	$^{+0.025}_{-0.024}$	$^{+0.038}_{-0.053}$
10, 13	0.23	± 0.0049	$^{+0.014}_{-0.011}$	$^{+0.018}_{-0.016}$
13, 17	0.11	± 0.0031	$^{+0.0016}_{-0.0071}$	$^{+0.0058}_{-0.0047}$
17, 22	0.039	± 0.0016	$^{+0.00087}_{-0.001}$	$^{+0.0011}_{-0.0014}$
22, 29	0.0059	± 0.00047	$^{+0.001}_{-0.00023}$	$^{+0.00031}_{-0.00018}$
29, 50	0.00072	$\pm 8.5E-05$	$^{+0.00023}_{-3E-05}$	$^{+8.3E-05}_{-5.2E-05}$
$120 < Q^2 < 2000$				
7.5, 10	0.01	± 0.00025	$^{+0.00041}_{-0.00098}$	$^{+0.001}_{-0.0014}$
10, 13	0.0099	± 0.00021	$^{+0.00043}_{-0.00076}$	$^{+0.00059}_{-0.0006}$
13, 17	0.0056	± 0.00014	$^{+0.00011}_{-0.00023}$	$^{+0.00022}_{-0.00025}$
17, 22	0.0021	$\pm 7.7E-05$	$^{+6.7E-05}_{-0.00011}$	$^{+0.00014}_{-6.4E-05}$
22, 29	0.00069	$\pm 3.6E-05$	$^{+7.1E-05}_{-3.9E-05}$	$^{+1.8E-05}_{-3.3E-05}$
29, 50	6E-05	$\pm 5.2E-06$	$^{+5E-06}_{-4.2E-06}$	$^{+3.4E-06}_{-2E-06}$

Table 6.4: *Measured dijet cross-section* $d^2\sigma/dQ^2dE_T^{\text{jet1}}$.

η^F bin	$d^\sigma/d\eta^F dQ^2$	Δ_{stat}	Δ_{syst}	Δ_{ES} (pb)
$0 < Q^2 < 1$				
-3, -1.8	771	± 27.5	$^{+39.1}_{-38.3}$	$^{+92.8}_{-119}$
-1.8, -1.4	3790	± 108	$^{+130}_{-49.8}$	$^{+305}_{-335}$
-1.4, -0.8	4510	± 96.9	$^{+162}_{-55.9}$	$^{+399}_{-571}$
-0.8, 0	5300	± 99.3	$^{+66.6}_{-229}$	$^{+494}_{-606}$
$0.1 < Q^2 < 0.55$				
-3, -1.8	229	± 18.1	$^{+3.41}_{-28.6}$	$^{+35.3}_{-21.3}$
-1.8, -1.4	939	± 64.2	$^{+77.3}_{-67.3}$	$^{+60.9}_{-98.9}$
-1.4, -0.8	1070	± 55	$^{+132}_{-81.6}$	$^{+82.2}_{-102}$
-0.8, 0	1240	± 58.7	$^{+165}_{-155}$	$^{+101}_{-126}$
$1.5 < Q^2 < 4.5$				
-3, -1.8	15.3	± 0.62	$^{+1.62}_{-2.08}$	$^{+1.68}_{-2.05}$
-1.8, -1.4	75.8	± 2.47	$^{+4.11}_{-8.29}$	$^{+5.58}_{-5.4}$
-1.4, -0.8	81.5	± 1.96	$^{+10}_{-1.15}$	$^{+5.05}_{-7.21}$
-0.8, 0	87.1	± 1.78	$^{+7.4}_{-8.2}$	$^{+6.37}_{-7.57}$
$4.5 < Q^2 < 10.5$				
-3, -1.8	6.67	± 0.19	$^{+0.37}_{-0.62}$	$^{+0.78}_{-0.85}$
-1.8, -1.4	26	± 0.61	$^{+3.17}_{-0.21}$	$^{+1.84}_{-2.06}$
-1.4, -0.8	26.8	± 0.47	$^{+0.27}_{-2.12}$	$^{+1.63}_{-1.81}$
-0.8, 0	24.9	± 0.41	$^{+2.16}_{-1.58}$	$^{+1.62}_{-1.97}$

Table 6.5: *Measured dijet cross-section* $d\sigma/dQ^2 d\eta^F$.

η^F bin	$d^\sigma/d\eta^F dQ^2$	Δ_{stat}	Δ_{syst}	Δ_{ES} (pb)
$10.5 < Q^2 < 49$				
-3, -1.8	1.45	± 0.031	$^{+0.17}_{-0.036}$	$^{+0.15}_{-0.2}$
-1.8, -1.4	6.57	± 0.11	$^{+0.48}_{-0.25}$	$^{+0.44}_{-0.47}$
-1.4, -0.8	6.21	± 0.084	$^{+0.37}_{-0.16}$	$^{+0.36}_{-0.45}$
-0.8, 0	4.78	± 0.064	$^{+0.4}_{-0.22}$	$^{+0.28}_{-0.37}$
$49 < Q^2 < 120$				
-3, -1.8	0.3	± 0.01	$^{+0.032}_{-0.042}$	$^{+0.036}_{-0.045}$
-1.8, -1.4	1.27	± 0.034	$^{+0.14}_{-0.08}$	$^{+0.098}_{-0.1}$
-1.4, -0.8	1.24	± 0.026	$^{+0.074}_{-0.08}$	$^{+0.076}_{-0.09}$
-0.8, 0	0.87	± 0.018	$^{+0.065}_{-0.056}$	$^{+0.059}_{-0.065}$
$120 < Q^2 < 2000$				
-3, -1.8	0.0097	± 0.00035	$^{+9.2E-05}_{-0.0011}$	$^{+0.00093}_{-0.0014}$
-1.8, -1.4	0.055	± 0.0015	$^{+0.0011}_{-0.0067}$	$^{+0.0035}_{-0.0032}$
-1.4, -0.8	0.051	± 0.001	$^{+0.003}_{-0.0012}$	$^{+0.0027}_{-0.0032}$
-0.8, 0	0.039	± 0.00082	$^{+0.002}_{-0.0019}$	$^{+0.0022}_{-0.0024}$

Table 6.6: *Measured dijet cross-section* $d\sigma/dQ^2 d\eta^F$.

PART III
Charm Production

Chapter 7

Heavy Quark Production

In Section II dijet production was studied in photoproduction, where the dominant hard scale was the transverse momentum of the outgoing parton, p_{T}, and DIS where the two scale play a role, Q and p_{T}. Studies of heavy quark production give the opportunity to investigate perturbative QCD with a third hard scale, that of the heavy quark mass, m_Q, in addition to Q and p_{T}. The charm mass is particularly well suited for the study of semi-perturbative effects in photoproduction and at low Q^2, as its mass lies near to the lower limit of applicability for perturbative calculations. The mass of the beauty quark lies well above this limit ($m_b \sim 3m_c$) and is therefore expected to provide a hard enough scale to study perturbative effects at low Q^2. In DIS the dominant hard scale again tends towards Q^2 (for $Q^2 \gg m_Q^2$) and one might expect no obvious theoretical advantages in the calculation of heavy quark production cross sections in this regime. Heavy quark production in photoproduction and DIS is however an important testing ground of the applicability of pQCD in describing multiscale processes.

The large data set now available at HERA make detailed studies of heavy quark production possible [75]. The study of charm jet production has been studied in some detail at HERA, as has charm fragmentation and the production of charmed mesons. Opportunities now also exist for the study of the charm content of the proton and photon, and studies of beauty production are possible [76], however these are currently limited by low statistics.

In this chapter the production of heavy quarks is discussed within the framework of perturbative QCD. This is followed by a short review of heavy flavour production results from HERA, and some of the remaining questions are introduce along with the theoretical challenges they present. Results are also available from

LEP and TEVATRON, including measurements of heavy quark hadroproduction, the lifetimes of heavy mesons and baryons and CP violation. These have not been included here as they are not relevant to the discussion that follows.

7.1 Heavy Quarks in pQCD

Heavy quark production in perturbative QCD follows roughly the same formalism as that of light quark production. The cross sections are calculated as the sum of contributions from direct and resolved processes, taken as the convolution of the partonic cross section with the parton distributions functions of the proton and photon respectively. Some aspects of the calculations of heavy quark production are simplified, since only the boson-gluon fusion process ($\gamma g \rightarrow qq$) contributes to the total direct cross section, and the resolved cross section is heavily dominated by heavy quark excitation ($qg \rightarrow qg$) [77] (see figure 7.1). Also the additional hard scale, m_Q, make more reliable perturbative calculations possible. However since at low transverse momentum the assumption that the quark mass is negligible no longer holds, a suitable treatment of the mass must be included in the calculations. Also how non-perturbative effects are dealt with, such as fragmentation and intrinsic transverse momentum, must be resolved.

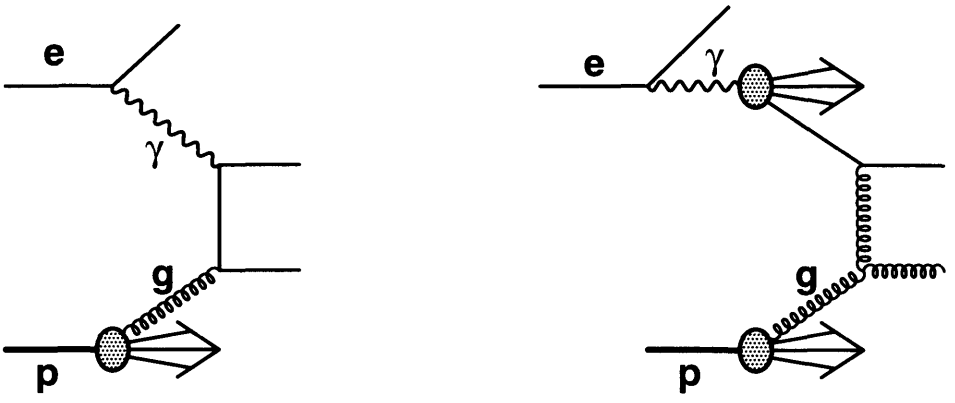

Figure 7.1: *Dominant leading order direct (left) and resolved (right) processes contributing to the production of heavy quarks.*

The inclusive hadroproduction of a heavy quark Q has been calculated to $\mathcal{O}(\alpha\alpha_s^2)$ [78]. The short distance cross sections, $\hat{\sigma}(s, m^2, \mu^2)$, for direct and resolved processes are dealt with separately, and are given in terms of the partonic

centre of mass energy, s, the quark mass m, and the factorisation scale μ, and are given by,

$$\hat{\sigma_{\gamma j}}(s, m^2, \mu^2) = \frac{\alpha\alpha_s(\mu^2)}{m^2} f_{\gamma j}(\rho, \mu^2/m^2), \tag{7.1}$$

and

$$\hat{\sigma_{ij}}(s, m^2, \mu^2) = \frac{\alpha_s^2(\mu^2)}{m^2} f_{ij}(\rho, \mu^2/m^2) \tag{7.2}$$

respectively [79], where $\rho = 4m^2/s$. The terms $f_{\gamma j}$ and f_{ij} are dimensionless functions, the form of which is dependent upon the process being described and the order to which the perturbative expansion is calculated. Normally the perturbative expansion is cutoff after two or three orders, above which contributions are expected to be small. The functions to leading order are given by,

$$f_{\gamma j}(\rho, \mu^2/m^2) = f_{\gamma j}^0(\rho) + g^2(\mu^2)\left[f_{\gamma j}^1(\rho) + \overline{f}_{\gamma j}^1(\rho)\log(\mu^2/m^2)\right] + ... \tag{7.3}$$

and

$$f_{ij}(\rho, \mu^2/m^2) = f_{ij}^0(\rho) + g^2(\mu^2)\left[f_{ij}^1(\rho) + \overline{f}_{ij}^1(\rho)\log(\mu^2/m^2)\right] + ... \tag{7.4}$$

These when convoluted with the AP splitting function, E, and a suitable fragmentation function, D, are used to calculate the heavy quark cross sections in the collinear resummation scheme such that,

$$\sigma = f \otimes E \otimes D. \tag{7.5}$$

7.1.1 Massive Schemes

The massive scheme [80] fixes the number of active flavours regardless of the scale of the interaction, μ. Only the gluons and the light quarks (u,d,s) are included in the initial proton and photon PDFs, with the heavy quark being produced dynamically in the hard scatter. This scheme was used to calculate the above dimensionless coefficients, $f_{\gamma j}(\rho, \mu^2/m^2)$ and $f_{ij}(\rho, \mu^2/m^2)$, from which it is clear that at large scales, $\mu^2 \gg m_Q^2$, terms in $\log(\mu^2/m_Q^2)$ become large and the calculations diverge. Such schemes are however suitable for calculating the cross section at scales near to the heavy quark mass.

7.1.2 Massless Schemes

In the massless scheme [81–83] the heavy quark is treated as an additional active flavour above some threshold, $\mu^2 \gg m_Q^2$, such that the incoming proton and photon PDFs contain u,d,s and c quarks. For $\mu^2 < m_Q^2$ it is no longer valid to treat the quark as massless, and the scheme is not applicable in the limit $\mu \to 0$. The massless scheme is not suitable for calculating most dijet cross sections at HERA, except those limited to high p_T jet production.
In order to compare such calculations to data it is necessary to adjust the heavy quark momentum such that it reflects the final state hadron, which will have a different momentum than the initial heavy quark. A fragmentation function is used to produce the hadron from the quark, which can be calculated perturbatively for heavy quark production. Generally however the perturbative description does not produce reliable calculations, particularly in regions of phase space where soft gluon production dominates. Higher order (Sudakov) resummations to some extent rectify the problem, however usually a non-perturbative description is used, where the non-perturbative parameters of the fragmentation function are extracted from fits to data. The non-perturbative fragmentation model proposed by Peterson et. al. is one such description of heavy quark fragmentation used at HERA. In the massless scheme the fragmentation function is included in the calculation. This is possible because the charm quark is active in the incoming proton in direct events, or photon in resolved events. In the massive scheme this is not possible and the fragmentation function is applied to the final state heavy quark.

7.2 Heavy Quark Production at HERA

Heavy flavour production has constituted a large part of the HERA physics program, yielding many interesting results and posing many new questions. Whilst a full review of all such results is beyond the scope of this thesis an overview of some recent results which illustrate the range of heavy flavour physics studied at HERA, and the current status of research into heavy flavour phenomena are given. Results from, for instance fixed target experiments and studies of diffractive heavy quark production are not included as they have been discussed previously, in for instance [85–88].

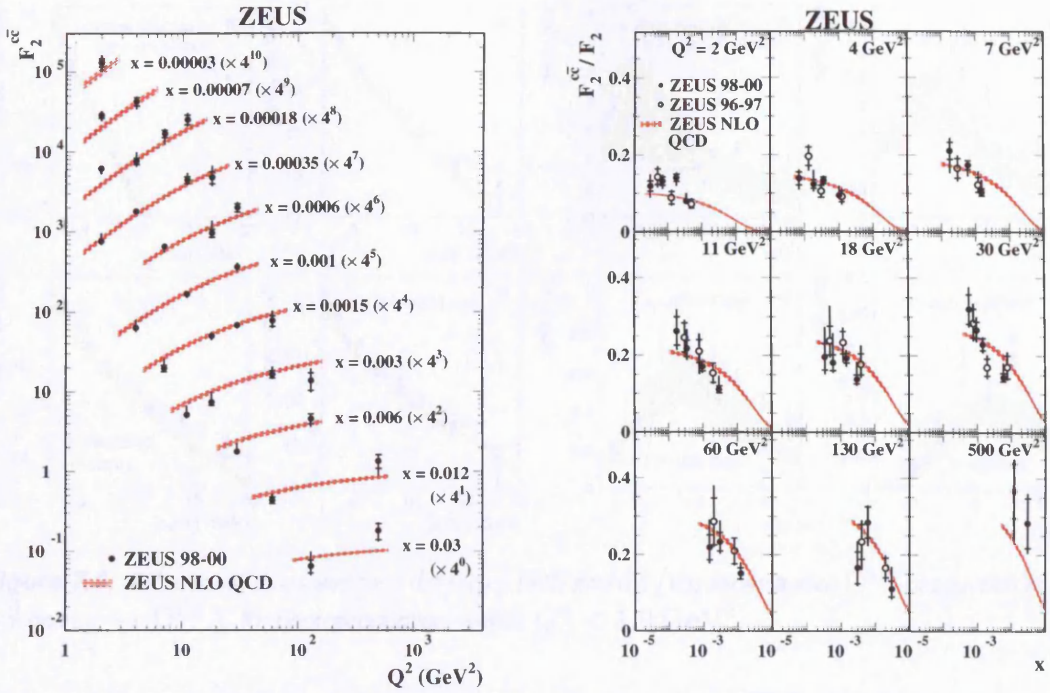

Figure 7.2: *Measurement of $F_2^{c\bar{c}}$ at x values between 0.00003 and 0.03 as a function of Q^2 (left). The ratio for $F_2^{c\bar{c}}/F_2$ at Q^2 values between 2 and 500 GeV^2 as a function of x (right).*

The study of beauty production is still in its infancy at HERA, and the majority of work has concentrated on charm production. The decay channels of the D$^{\star\pm}$(2010) meson have proved particularly useful. The D$^{\star\pm}$ meson decays through a small number of well understood channels, which can be tagged by reconstructing their decay vertices. The primary channels used are,

$$\mathrm{D}^{\star\pm} \rightarrow D^0\pi_s^{\pm} \rightarrow (K^{\mp}\pi^{\pm})\pi_s^{\pm} \tag{7.6}$$

$$\mathrm{D}^{\star\pm} \rightarrow D^0\pi_s^{\pm} \rightarrow (K^{\mp}\pi^{\pm}\pi^{\pm}\pi^{\mp})\pi_s^{\pm}. \tag{7.7}$$

These channels have well defined signals in their mass difference distributions, $\Delta M = m(\mathrm{D}^{\star\pm}) - m(D^0)$, in a region of phase space not heavily populated by the combinatorial background.

The decay of this meson was used to extract the charm contribution to the structure function F_2 in [89]. Figure 7.2 shows the value of $F_2^{c\bar{c}}$ as a function of Q^2 in fixed bins of x on the left, with the fractional contribution to

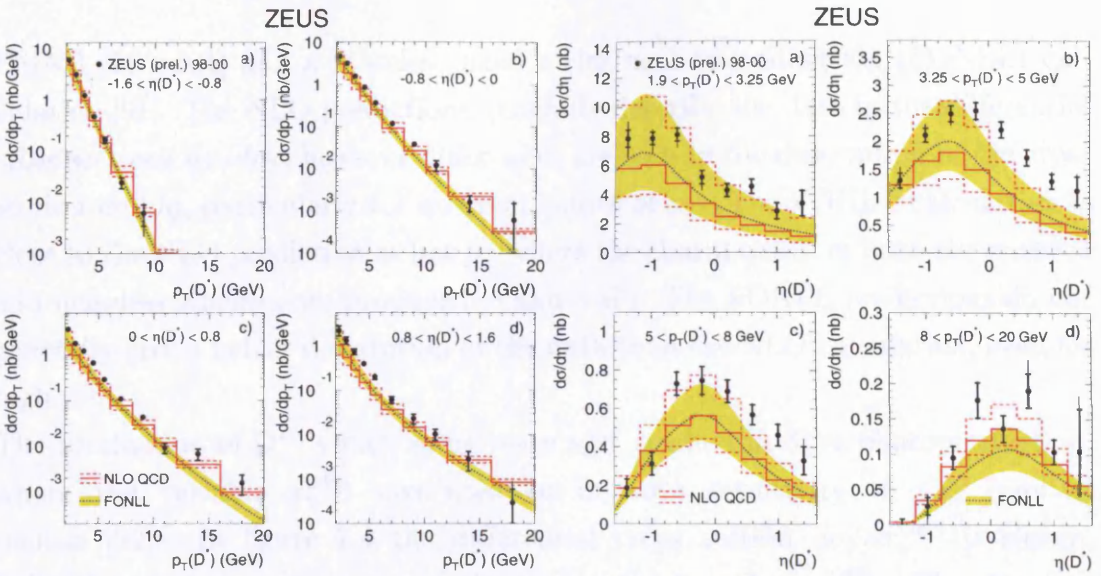

Figure 7.3: *Differential cross sections $d\sigma/dp_{\mathrm{T}}$ (left) and $d\sigma/d\eta$ for inclusive $\mathrm{D}^{\star\pm}$ production in the process $ep \to \mathrm{D}^{\star\pm}X$ for photoproduction events, $Q^2 < 1.0\,\mathrm{GeV}^2$.*

the total F_2 (i.e. $F_2^{c\bar{c}}/F_2$) on the right. The data in the left hand figure rise with increasing Q^2, with the rise becoming steeper at lower x, demonstrating the scaling violation of $F_2^{c\bar{c}}$. The charm contribution to F_2 (right) rises from 10% to 30% as Q^2 increases and x decreases. The results are compared to the NLO calculation of HVQDIS [90] which are generally in good agreement with the data, although small discrepancies exist at low Q^2.

Figure 7.3 shows the differential cross sections $d\sigma/dp_{\mathrm{T}}$ as a function of the transverse momentum of the $\mathrm{D}^{\star\pm}$, $p_{\mathrm{T}}(D^*)$, in bins of $\eta(D^*)$, and $d\sigma/d\eta$ as a function of $\eta(D^*)$ in bins of $p_{\mathrm{T}}(D^*)$, for photoproduction events containing a $\mathrm{D}^{\star\pm}$ meson. The results explore the applicability of the massive next-to-leading order (NLO) calculation of

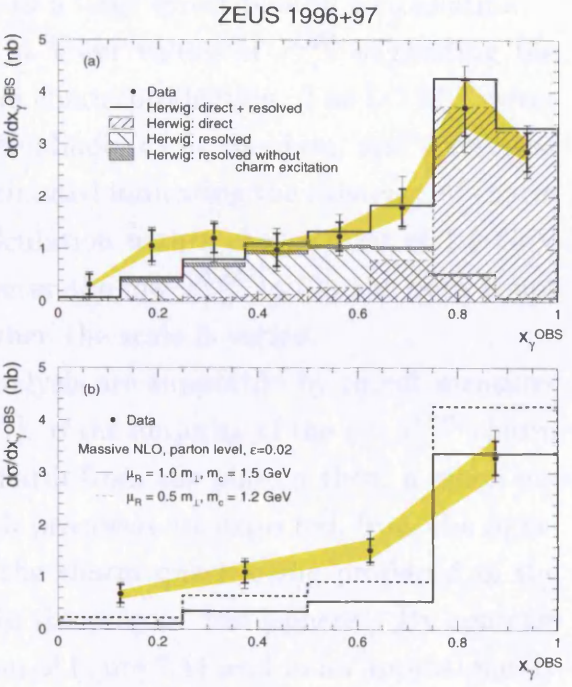

Figure 7.4: *The differential cross section $d\sigma/dx_\gamma^{\mathrm{OBS}}$ for dijets with an associated $\mathrm{D}^{\star\pm}$ meson compared to the leading order predictions of HERWIG (top) and the predictions of a NLO massive calculation (bottom).*

FMNR [100, 101] and a massless fixed order next-to-leading log (FONLL) calculation [91]. The NLO predictions generally describe the data in the differential cross sections $d\sigma/dp_{\mathrm{T}}$, however differences are seen in the description of the cross section $d\sigma/d\eta$, particularly for medium values of p_{T}. The FONLL calculation is close to the NLO prediction at low p_{T} where the charm quark in both the massive and massless schemes are produced dynamically. The FONLL predictions do not generally give a better description of the data than the NLO calculation, even for high p_T.

The production of $D^{*\pm}$'s was, some years ago, studied in dijet photoproduction, where the variable x_γ^{OBS} was used to increase sensitivity to the resolved photon [92]. In figure 7.4 the differential cross section $d\sigma/dx_\gamma^{\mathrm{OBS}}$ is shown, indicating a clear suppression of the cross section at low x_γ^{OBS}. The data are compared to the LO MC prediction of HERWIG in the upper plot, and to an NLO prediction calculated in the massive scheme in the lower plot. A peak in the data at high x_γ^{OBS} is seen, indicative of a large direct photon contribution.

A large cross section is also measured at lower values of x_γ^{OBS} suggesting the need for a resolved photon contribution in charm production. The LO MC direct and resolved predictions were varied individually to fit the data, and a resolved charm contribution of about 45% was estimated indicating the existence of charm excitation in the photon. The NLO calculation with a charm mass of 1.5 GeV describes the data for $x_\gamma^{\mathrm{OBS}} > 0.75$, however the low x_γ^{OBS} tail in the data is not well described by the calculation even when the scale is varied.

The conclusions reached in the above analysis are supported by recent measurements of dijet charm photoproduction [77]. If the majority of the low x_γ^{OBS} charm production cross section is a result of charm from the photon then, a gluon exchange process should be dominant. Such processes are expected, from the right-hand diagram of figure 7.1, to lead to the charm quark being produced in the photon "hemisphere", with a gluon jet in the proton "hemisphere". By contrast the LO direct diagrams (lefthand diagram of figure 7.1) lead to an approximately symmetrical distribution (over a large number of events), with a $c\bar{c}$ pair being produced in the dominant boson-gluon fusion process.

Figure 7.5 shows the charm tagged dijet cross sections as a function of $cos\ \theta^*$, where θ^* is defined as the angle between the jet-jet axis and the proton beam direction. In the unique case when a particular flavour, in this case charm, can be tagged and thus associated to a jet the sign of $cos\theta^*$ can be determined. The

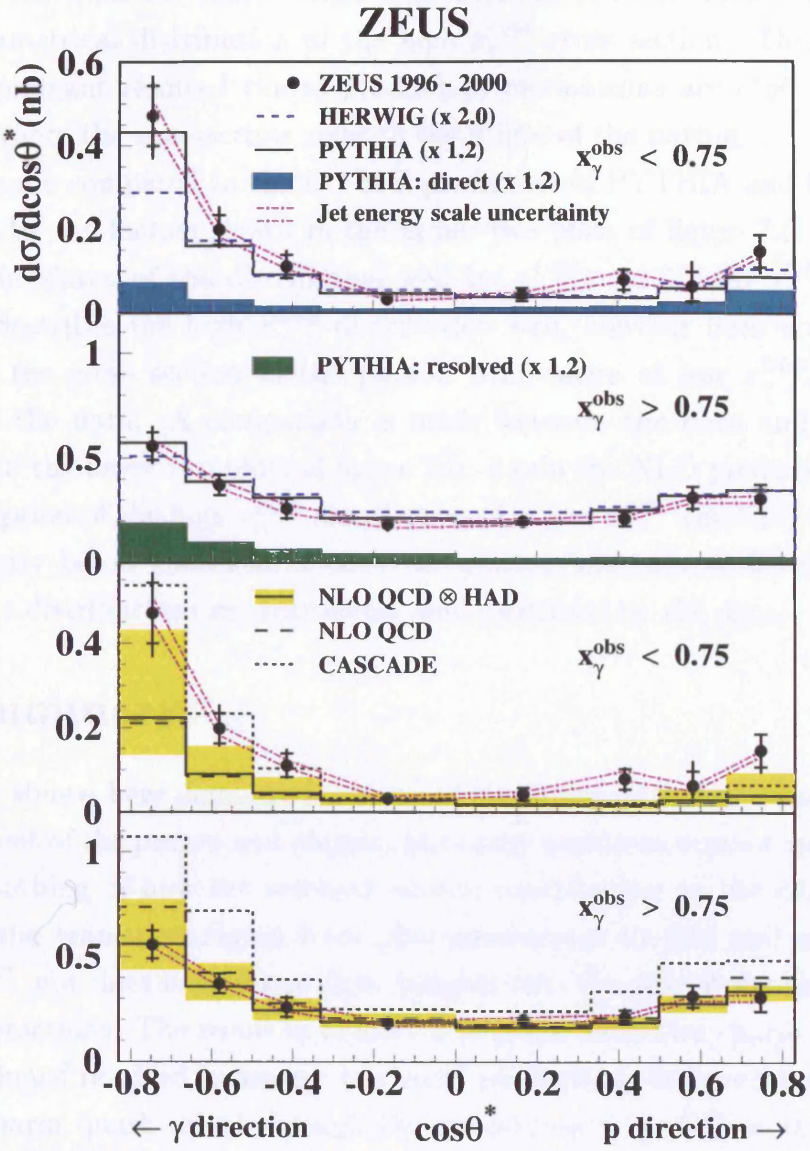

Figure 7.5: *Differential cross-sections $d\sigma/dcos\theta^*$ (dots) compared with a-b) PYTHIA and HERWIG MC simulations (histograms); c-d) CASCADE (short dashed lines) and NLO FO predictions after hadronisation correction (full lines) and at parton level (long-dashed lines). Results are given separately for the low $x_\gamma^{\rm OBS}$ $(x_\gamma^{\rm OBS} < 0.75)$ and high $x_\gamma^{\rm OBS}$ $(x_\gamma^{\rm OBS} > 0.75)$ regions.*

enhancement towards $cos\ \theta^* = -1$ in the low x_γ^{OBS} cross section then supports the assumption that the charm originated from the photon. This is contrasted by the symmetrical distribution of the high x_γ^{OBS} cross section. This indicates that the dominant resolved charm production mechanisms are $c^\gamma g^p \rightarrow cg$ and $c^\gamma q \rightarrow cq$, where the superscripts refer to the origin of the parton.
The results are compared to the LO MC prediction of PYTHIA and HERWIG, normalised by the factors shown in the upper two plots of figure 7.5. PYTHIA describes the shape of the distribution well for $x_\gamma^{\mathrm{OBS}} < 0.75$ and $x_\gamma^{\mathrm{OBS}} > 0.75$. HERWIG describes the high x_γ^{OBS} distribution well, however does not describe the rise in the cross section in the photon hemisphere at low x_γ^{OBS}, which is stronger in the data. A comparison is made between the data and the NLO prediction in the lower two plots of figure 7.5. Again the NLO prediction gives a good description of the high x_γ^{OBS} distribution. For low x_γ^{OBS} the NLO prediction is significantly below the data in both the photon and proton direction. The shape of the distributions are reasonably well described by the data.

7.3 Summary

The results shown here demonstrate some of the advances in understanding the charm content of the proton and photon, but many questions remain unanswered. They say nothing of how the resolved photon contribution to the cross section evolves in the transition region from photoproduction to DIS and up to high values of Q^2, nor does it give any clear insights into the role of the charm mass in such interactions. The result in figure 7.5 demonstrates that charm excitation is the dominant resolved processes in charm production, however does not tell us if the charm quark arises through the anomalous $\gamma \rightarrow Q\overline{Q}$ or through the VMD chain $\gamma \rightarrow V \rightarrow Q\overline{Q}$ with the heavy quark arising from a gluon splitting. How the ratio of low to high x_γ^{OBS} cross sections, which was shown to be strongly suppressed with increasing Q^2 in the all-flavours measurement, evolves in the presence of charm is also an unanswered question. The remainder of this thesis is primarily concerned with these questions.

Chapter 8

Kinematic Reconstruction and Event Selection

The principles of reconstructing event and jet kinematic variables are the same in most analyses. Quantities measured in the detector are used to determine the event variables given the current best knowledge of the accelerator, detector and reconstruction techniques. The analysis presented here is no exception, and the methods used are almost identical to those described in chapter 3, except that the presence of a $D^{\star\pm}$ meson is required within a specific kinematic region.

8.1 Definition of Measured Cross Sections

Inclusive dijet cross sections tagged with an associated $D^{\star\pm}(2010)$ meson were measured, where the $D^{\star\pm}$ was not required to be associated to a jet. The measurement was performed for a wide range of photon virtualities, $0 < Q^2 < 5000.0\text{GeV}^2$, and in the range $0.2 < y < 0.55$, corresponding to the identical kinematic region of the all-flavours measurement of section II. Dijet cross sections, differential in Q^2 were measured in two regions of x_γ^{OBS}, with the contribution from resolved processes being enhanced using the ratio, R, of the two cross sections where,

$$R = \frac{d\sigma(x_\gamma^{\text{OBS}} < 0.75)}{dQ^2} \Big/ \frac{d\sigma(x_\gamma^{\text{OBS}} > 0.75)}{dQ^2}. \tag{8.1}$$

The measurements were performed in two kinematic regions distinguished by the two frames of reference in which jet reconstruction was performed. In the laboratory frame the jets were reconstructed with the kt-cluster algorithm in

the longitudinally invariant mode, with at least two jets required to lie in the kinematic region defined by,

- $E_T^{jet1,jet2} > 6.5, 7.5$ GeV^2;
- $-2.4 < \eta^{jet} < 2.4$.

In the photon-proton centre-of-mass frame, the measurements were performed in the kinematic region defined by,

- $E_T^{jet1,jet2} > 6.5, 7.5$ GeV^2;
- $-3.0 < \eta^{jet} < 0.0$.

In these measurements the $D^{\star\pm}$ meson was not required to be directly associated to a jet, but was required to lie in the region defined by,

- $p_T(D^{\star\pm}) > 3$GeV;
- $|\eta(D^{\star\pm})| < 1.5$,

in the laboratory frame.

8.2 Online Event Selection

The online event selection used the same three level trigger system [8] outlined in sections 1.6 and 4.2. The precise logic used was identical to that of the subsections 4.2.1, 4.2.2 and 4.2.3, with dijet events being selected with no requirement being made on the presence of a $D^{\star\pm}$ online. Although trigger slots exist for the online selection of $D^{\star\pm}$'s, the dijet trigger chain is favoured due to its higher efficiency. All events passing the dijet trigger were then scanned for the presence of $D^{\star\pm}$'s offline.

8.3 Offline Event Selection

Cuts were applied offline to the data sample to improve its purity whilst retaining an optimal number of $D^{\star\pm}$ mesons. Three separate sets of jet selection criteria are presented here, which represent the evolution of the analysis chronologically, in terms of the accuracy of the reconstruction methods used and the frame of

reference in which the measurement was performed. The analysis was in the first instance performed in the laboratory frame, in an approximately equivalent kinematic region to the all-flavours measurement. In order to compare and contrast the charm tagged measurement with the all-flavours measurement the analysis was also performed in the photon-proton centre of mass frame, and the same cut values were used as in the all-flavours measurement.

8.3.1 Subsample Selection

The analysis presented here covers a wide range of photon virtualities, $0 < Q^2 < 5000.0$ GeV^2, excluding the region $1.0 < Q^2 < 1.5$ GeV^2 where the scattered electron is not efficiently tagged. The detector response was used to separate the sample into two subsamples corresponding to photoproduction and deep inelastic scattering. This was done in the following way.

- **Photoproduction** events were selected by requiring that no scattered positron was found in the CAL with energy $E_e' > 5$ GeV and $y_e < 0.7$. Electrons misidentified by the SINISTRA [43] electron finder are recovered by the above vetoes, the remaining photoproduction sample contains events in the region $Q^2 < 1.0$, with a median at 10^{-3} GeV^2.

- **Deep Inelastic Scattering** (DIS) events were selected by required that a scattered positron was found in the calorimeter with $E_e' > 10.0$ GeV and $y_e > 0.02$. A box cut, identical to that shown in figure 4.1 was applied to remove poorly reconstructed electrons. The variables Q^2 and y_e were reconstructed using the electron method of equations 3.6 and 3.7, and the DIS sample was separated into four divisions of Q^2 corresponding to $1.5 < Q^2 < 4.5$ GeV^2, $4.5 < Q^2 < 10.5$ GeV^2, $10.5 < Q^2 < 49.0$ GeV^2 and $49.0 < Q^2 < 5000.0$ GeV^2.

8.3.2 General Selection

Additional cuts were applied before jet selection to optimise the proportion of "physics events" in the sample, and reject events from unwanted processes. An event vertex consistent with the nominal interaction point was ensured by requiring $|Z_{\text{vtx}}| < 50cm$. This is predominantly to reduce the loss of material outside of the coverage region of the ZEUS detector. Beam gas events, caused

mainly by the interaction of the proton beam with residual gas in the beam pipe, were rejected by requiring that $0.15 < y_{JB} < 0.55$, where y_{JB} was reconstructed from either uncorrected calorimeter cells or energy corrected EFOs, depending upon which method was used for jet reconstruction.

8.3.3 Jet selection

In all cases jets were reconstructed with the k_T-cluster algorithm [41] in the longitudinally invariant inclusive mode. Where a well reconstructed scattered electron was identified (i.e DIS) by SINISTRA, either the corresponding calorimeter en-

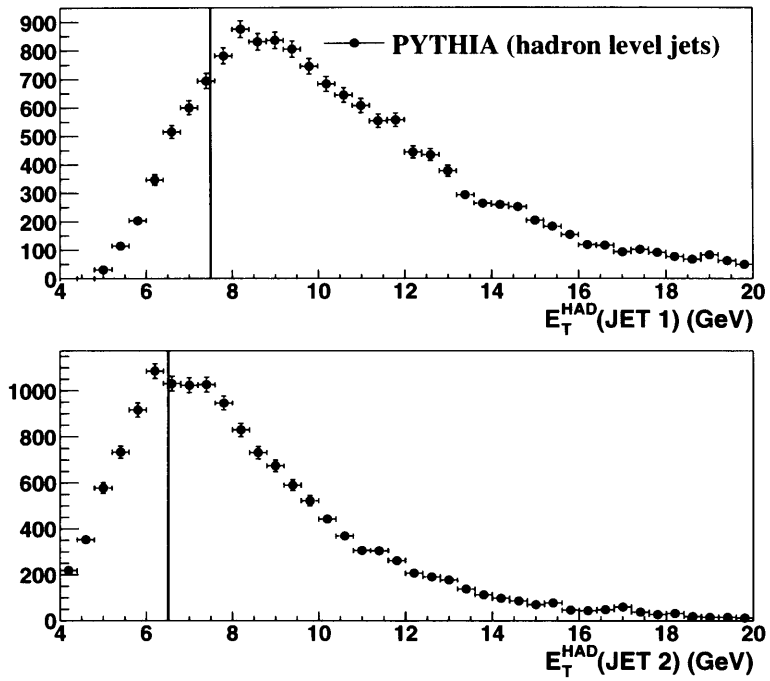

Figure 8.1: *Hadron level jet E_T for events passing detector level jet cuts, with jets reconstructed from uncorrected calorimeter cells. The vertical line represents the kinematic cut on each of the two jets. The area under the histogram to the left of the line is equivalent to the number of jets selected that lie outside of the true kinematic reion.*

ergy deposit or EFO was removed before jet finding (and before the calculation of hadronic energy sums). In the first instance the jet finding algorithm was applied to uncorrected calorimeter cells in the laboratory frame. A cut was chosen which optimised the statistics of the $D^{\star\pm}$ sample whilst roughly corresponding to the required jet kinematics. At least two jets were required to satisfy,

- $E_T^{jet1,jet2} > 4.0$ GeV

- $|\eta| < 2.4$.

Figure 8.1 shows the "true" value of E_T^{jet} for the two hardest jets passing these cuts. The figure illustrates the crudeness of the cuts, showing that approximately 25% of the sample lies outside of the required kinematic region. The low purity of the sample means a large dependence on the Monte Carlo is expected when unfolding cross sections from jets reconstructed in this way. The measurement was refined by running the $kt-$cluster [41] algorithm over EFOs [37] in the laboratory frame. Prior to jet finding the EFOs were corrected for losses in energy incurred traversing dead material in the detector. The correction method employed was identical to that described in section 3.1.5. The method has been shown to reconstruct the "true" jet transverse energy with a resolution of $\sim 1\%$ at high E_T and $\sim 2\%$ at low E_T. Using this method at least two jets were required satisfying,

- $E_T^{jet1,jet2} > 6.5, 7.5$ GeV
- $|\eta| < 2.4$.

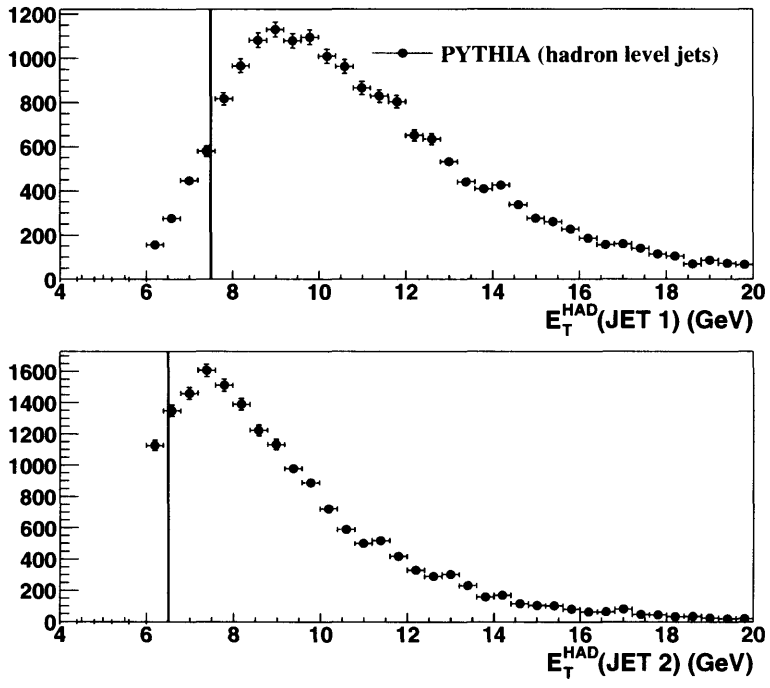

Figure 8.2: *Hadron level jet E_T for events passing detector level jet cuts, with jets reconstructed from corrected EFOs. The vertical line represents the kinematic cut on each of the two jets. The area under the histogram to the left of the line is equivalent to the number of jets selected that lie outside of the true kinematic region.*

Figure 8.2 shows the "true" value of E_T^{jet} passing the above cuts with jets reconstructed from energy corrected EFOs in the laboratory frame. The fraction of misidentified jets is clearly smaller relative to figure 8.1, with approximately 8% of the sample outside of the required kinematic region.
The corrected EFOs were finally boosted into the photon-proton centre of mass frame prior to jet finding. The boost was performed using either the scattered positron in the case of DIS [46], or the prescription outlined in section 3.5.1 for photoproduction. At least two jets were required in the photon-proton centre of mass frame satisfying,

- $E_T^{jet1,jet2} > 6.5, 7.5$ GeV
- $-3.0 < \eta < 0.0$.

The jets were then boosted back into the laboratory frame and the value of $x_\gamma^{\rm OBS}$ was determined from quantities in the laboratory frame. Dijet cross sections were measured in both the laboratory frame and the photon-proton centre of mass frame.

8.4 $D^{\star\pm}$ Reconstruction and Selection

Tracks from the CTD were used to reconstruct $D^{\star\pm}$'s in the decay channel $D^{\star\pm} \to D^0\pi_s^\pm \to (K^\mp\pi^\pm)\pi_s^\pm$. Pions and kaons cannot be uniquely differentiated, so in the first instance every track which was assigned to the primary event vertex and passed through three CTD superlayers or more was alternately assigned as type "kaon" or type "pion", i.e assigned the kaon or pion mass. Oppositely charged combinations of tracks with $p_T(K,\pi) > 0.45$ GeV were then combined to form a D^0 candidate. If the mass of the candidate lay in the range $1.8 < m(D^0) < 1.92$ GeV, it was combined with another track of type "pion", called the "slow pion", π_s, due to its low energy (since the difference in mass between the $D^{\star\pm}$ and the $D^0\pi_s$ combination is small [97]). The π_s was required to have opposite charge to the track of type "kaon" and a $p_T(\pi_s) > 0.15$ GeV. The requirement on the transverse momentum of the π_s restricts it to a region where the pion background is suppressed. The combination of these three tracks then made the $D^{\star\pm}$ candidate, which was accepted if $p_T(D^{\star\pm}) > 3.0$ GeV and $|\eta(D^{\star\pm})| < 1.5$. The combination of these two cuts both ensures that the $D^{\star\pm}$ as well as its decay products lie in a well understood region of the detector, and the combinatorial background is reduced relative to the signal. The $D^{\star\pm}$ signal was then extracted from the $\Delta M = m(D^{\star\pm}) - m(D^0)$ distribution [93].

8.4.1 Background Estimation

Two methods were employed to extract the number of $D^{\star\pm}$'s from the background:

- **Wrong Charge Background:** The number of background events was estimated from a consideration of the wrong-sign $K\pi$ combinations [94]. The selection is identical to that of section 8.4, except that the two tracks forming the D^0 candidate were required to have an equal charge of ± 1. Combinations satisfying the selection criteria and lying in the same mass region as the signal, give a good description of the background, as is shown in figure 8.3. Such combinations lie in the same region of phase space as the signal, and with appropriate scaling can be subtracted to give an estimate of the true number of $D^{\star\pm}$'s measured.

- **Log Likelihood Fit:** In the log likelihood or unbinned fit method [95] the aim is to maximise the use of information in a data set and remove common biases associated with fitting a binned (histogrammed) sample. The procedure finds the most likely set of parameters $\vec{\alpha}$ given a set of values x_i, and a user defined probability distribution function $p(x_i, \vec{\alpha})$ dependent on x_i. Fitting in this way has a number of advantages over fitting to a pre-binned sample. The distinction of an events location in a bin, lost in a binned fit, is restored and the fit is independent of empty bins and bin width. As such the method is particularly useful when the set x_i is small.

The low statistics available in the data sample studied here, particularly when the DIS sample is divided into the four bins of Q^2 detailed in section 8.3.1, make estimation by wrong charge subtraction difficult and inaccurate, as the estimation of the background is subject to large statistical fluctuations. As such the primary method of extracting the number of $D^{\star\pm}$'s was the unbinned fit method, with the wrong charge background method being used as a systematic check of the accuracy of the fitting procedure. Despite the statistical restrictions the two methods differ by only $\sim 5\%$ across all bins. A three parameter fit is performed with the function:

$$F(\Delta M) = \frac{P1}{\sqrt{2\pi}\sigma_{\Delta M}} e^{-\frac{(\Delta M - < \Delta M >)^2}{2\sigma_{\Delta M}}} + P2(\Delta M - m_\pi)^{P3} \qquad (8.2)$$

Where ΔM is defined above. $< \Delta M >$ and $\sigma_{\Delta M}$ are the mean and width of the Gaussian, and were fixed to values obtained from a five parameter fit to the

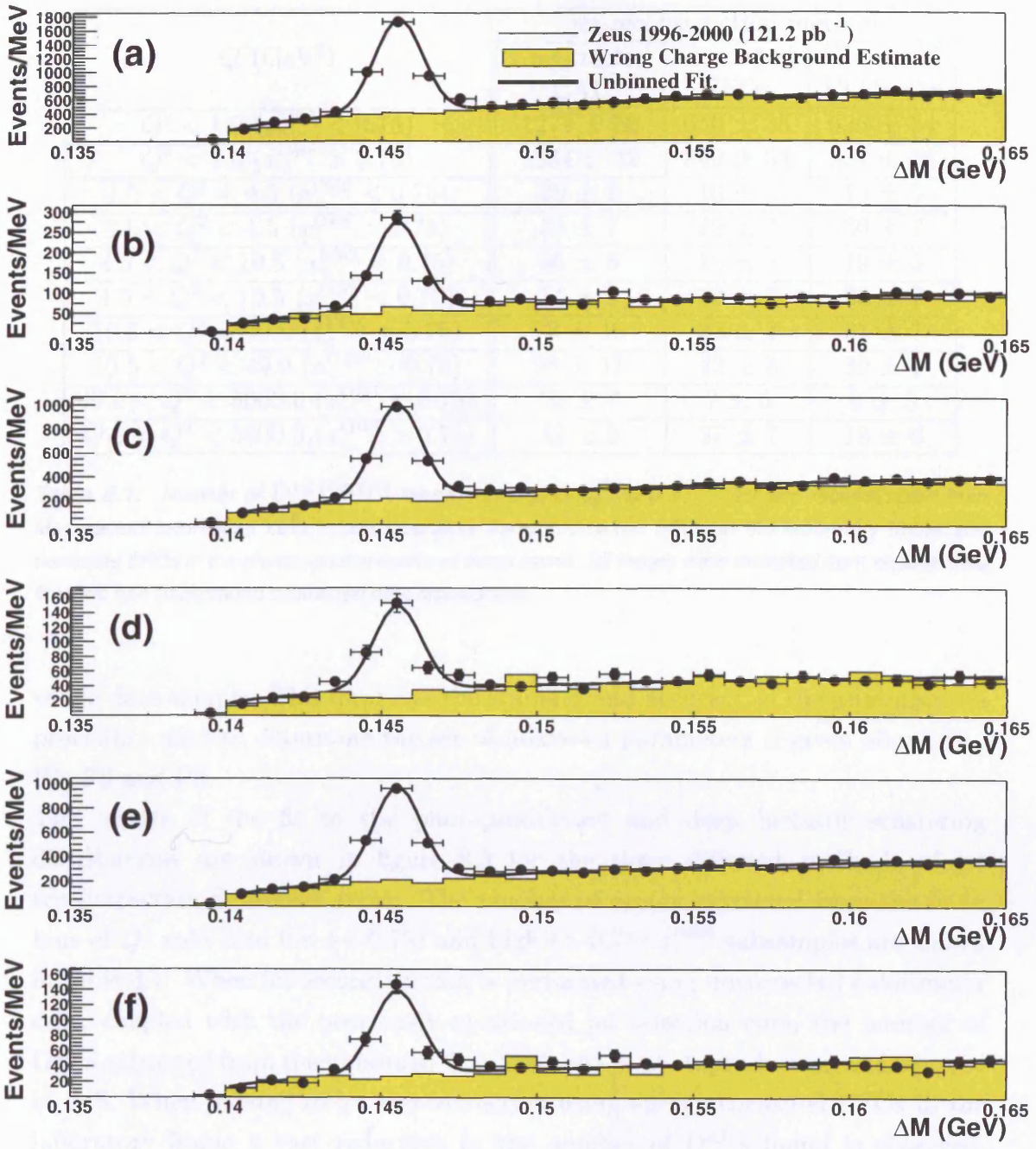

Figure 8.3: *$D^{\star\pm}$ signals for photoproduction (a,c,e) and DIS (b,d,f) shown with the result of an unbinned fit to the $\Delta M = m(D^{\star\pm}) - m(D^0)$ distribution for dijet events containing a $D^{\star\pm}$ meson. Distributions are shown for jets reconstructed with uncorrected calorimeter cells in the laboratory frame (a-b), corrected EFOs in the laboratory frame (c-d) and corrected EFOs in the photon-proton center of mass frame (e-f).*

$Q^2(\mathrm{GeV}^2)$	jet reconstruction method		
	Uncorrected CAL	Corrected EFOs	Corrected EFOs $\gamma^* p$
$Q^2 < 1.0$ ($x_\gamma^{\mathrm{OBS}} < 0.75$)	1279 ± 50	650 ± 35	625 ± 34
$Q^2 < 1.0$ ($x_\gamma^{\mathrm{OBS}} > 0.75$)	1284 ± 42	849 ± 34	834 ± 34
$1.5 < Q^2 < 4.5$ ($x_\gamma^{\mathrm{OBS}} < 0.75$)	29 ± 7	16 ± 5	15 ± 5
$1.5 < Q^2 < 4.5$ ($x_\gamma^{\mathrm{OBS}} > 0.75$)	35 ± 7	29 ± 7	30 ± 7
$4.5 < Q^2 < 10.5$ ($x_\gamma^{\mathrm{OBS}} < 0.75$)	36 ± 8	18 ± 5	19 ± 5
$4.5 < Q^2 < 10.5$ ($x_\gamma^{\mathrm{OBS}} < 0.75$)	54 ± 9	33 ± 7	33 ± 7
$10.5 < Q^2 < 49.0$ ($x_\gamma^{\mathrm{OBS}} < 0.75$)	72 ± 10	32 ± 7	31 ± 7
$10.5 < Q^2 < 49.0$ ($x_\gamma^{\mathrm{OBS}} > 0.75$)	93 ± 11	42 ± 8	39 ± 7
$49.0 < Q^2 < 5000.0$ ($x_\gamma^{\mathrm{OBS}} < 0.75$)	25 ± 7	7 ± 5	9 ± 5
$49.0 < Q^2 < 5000.0$ ($x_\gamma^{\mathrm{OBS}} > 0.75$)	42 ± 9	27 ± 7	18 ± 6

Table 8.1: *Number of $D^{\star\pm}(2010)$ mesons in bins of Q^2 and x_γ^{OBS} for jets reconstructed from uncorrected calorimeter cells in the laboratory frame, corrected EFOs in the laboratory frame and corrected EFOs in the photon-proton centre of mass frame. All values were extracted from an unbinned fit to the non-background subtracted data distributions.*

whole data sample. This improves the stability and accuracy of the minimisation procedure used to determine the set of unknown parameters $\vec{\alpha}$ given above by , P1, P2 and P3.

The results of the fit to the photoproduction and deep inelastic scattering distributions are shown in figure 8.3 for the three different methods of jet reconstruction described above. The number of events extracted from the fit in bins of Q^2 split into low (< 0.75) and high (> 0.75) x_γ^{OBS} subsamples are shown in table 8.1. When jet reconstruction is performed using uncorrected calorimeter cells, coupled with the previously mentioned jet selection cuts, the number of $D^{\star\pm}$'s extracted from the unbinned fit is 2563±65 in photoproduction and 386±24 in DIS. When moving to jet reconstruction using energy corrected EFOs in the laboratory frame a vast reduction in the number of $D^{\star\pm}$'s found is observed. The photoproduction sample contains 1499 ± 49 $D^{\star\pm}$'s and the DIS 204 ± 19 representing a decrease in statistics of $\sim 40\%$ for $Q^2 < 10.5$ GeV^2 and $\sim 50\%$ for $Q^2 > 10.5$ GeV^2. A negligible decrease in statistics is observed when the analysis is carried out using jets reconstructed from energy corrected EFOs in the photon-proton centre of mass frame, with the most marked difference occurring in the highest Q^2 bin where the $D^{\star\pm}$ sample is reduced by $\sim 20\%$. The reason for this was demonstrated in figures 8.1 and 8.2 where it was shown that the uncorrected

calorimeter cell sample contains a large fraction of jets with transverse energy outside of the required kinematic region. It might be expected therefore that the use of uncorrected calorimeter cells with a cut at $E_{\mathrm{T}}^{\mathrm{jet}} > 4.0$ GeV will lead to increased statistics however lower purity, implying that the measurement is more dependent on the Monte Carlo model and detector simulation than the corrected EFOs sample. This is investigated further in the next chapter.

Chapter 9

Monte Carlo Simulation and Description of Data.

9.1 Event Simulation

The data was corrected for smearing of kinematic variables in the detector, and trigger inefficiencies using a method similar to that described in section 5.1. The Monte Carlo method was used to simulate events describing the underlying event dynamics. Non-perturbative effects such as parton showering and hadronisation were simulated, to produce a sample of Monte Carlo events containing a $D^{\star\pm}$. The generated events were passed through the MOZART [49] simulation of the ZEUS detector. Two trigger configurations and two beam energies were used during the 1996-2000 running periods. This was taken into account by separating the Monte Carlo sample into four subsamples each of which was then passed through the ZGANA trigger simulation separately before the event was reconstructed offline by the ZEPHYR program.

9.2 Monte Carlo Generators

Leading order direct and resolved events were generated separately using the PYTHIA 6.1 [51] Monte Carlo event generator. The MRSA [53] and SaS1D [28] sets for the proton and photon parton distributions functions were used. A filter was applied before the detector simulation requiring the presence of at least one $D^{\star\pm}$ with $p_T(D^{\star\pm}) > 2.5\text{GeV}$ and $|\eta(D^{\star\pm})| < 3.0$ in the $D^{\star\pm} \rightarrow D^0\pi_s^{\pm} \rightarrow (K^{\mp}\pi^{\pm})\pi_s^{\pm}$. A jet filter was also applied to increase the efficiency with which dijet events were generated. The filter reconstructs jets with the EUCELL [40]

cone algorithm working in the laboratory frame, and events were selected with $E_{\mathrm{T}}^{\mathrm{JET}} > 4.0$ GeV and $|\eta^{\mathrm{JET}}| < 3.0$, an identical requirement to the online dijet trigger used for the selection of data.
A second smaller sample of events were generated with the HERWIG [50] Monte Carlo generator. The MRSA [53] and SAS1D [28] sets for the proton and photon parton distribution functions were again used. The sample was used to conduct a study on the systematic uncertainty arising from the choice of Monte Carlo used. In both cases the direct and resolved samples were reweighted offline using a single parameter χ^2 fit of the combined Monte Carlo, to the uncorrected, background subtracted x_γ^{OBS} distributions of the data. The procedure was performed separately for each of the required bins of Q^2. The data distributions were however limited by low statistics, particularly for $Q^2 > 1.5$ GeV^2. The DIS sample was split into just two subsamples to perform the fit, which reduced the effects of statistical fluctuations in the data distribution.

9.3 Description of Data

If the Monte Carlo is to be used to perform acceptance corrections of the data it must give a reasonable description of the data, particularly the parameters used to select the data sample. The background subtracted data are compared to the reweighted Monte Carlo in figures 9.1, 9.2 and 9.3 for the three methods of jet reconstruction described in the previous chapter.
Figure 9.1 shows the comparison of the data to Monte Carlo when uncorrected calorimeter cells were used to reconstruct the jets in the laboratory frame. The description of all quantities are reasonable for the purposes of this study, however differences do exist. The description of the transverse energy of the jets is reasonably good, however the data has a number of fluctuations in the distribution of E_T^{jet1}, caused by large discrepancies in the wrong charge background, particularly where statistics were limited at high E_T. Both of the jets exhibit a more rapid fall in the data than is observed in the Monte Carlo, however both exhibit a roughly logarithmic behaviour for $E_T^{jet} > 6.5$ GeV. The jet pseudorapidities are described well by the Monte Carlo, as is the jet multiplicity. The variable y_{JB} is very well described by the Monte Carlo. The electron variables E_e and θ_e, which were reconstructed only in the DIS regime where a scattered electron is detected, are subject to the largest statistical fluctuations in the

wrong charge background. The electron energy E_e is however well described by the Monte Carlo, however the polar angle at which the electron is scattered, θ_e shows significant differences. The variables used to define the $D^{\star\pm}$ kinematics, $p_T(D^{\star\pm})$ and $\eta(D^{\star\pm})$ are both very well described. The transverse momentum of the $D^{\star\pm}$ exhibits a similar turnover at $p_T(D^{\star\pm}) > 6.5$ GeV, as was seen in the jets. This confirms the expectation that the charm quark plays a significant role in determining the final state jet properties.

In Figure 9.2 the Monte Carlo is compared to the data from the analysis where jets were reconstructed using energy corrected ZUFOs in the laboratory frame. The description of all variables is good. The jet transverse energies exhibit similar behaviour to that seen in the previous figure, with the turnover to logarithmic behaviour occurring for $E_T^{jet} > 8.5$ GeV, and differences between Monte Carlo and data occurring at high E_T^{jet} where statistics are most limited. The jet pseudorapidities η^{jet} and the multiplicity N_{jet} are again well described, as is the variable y_{JB}. The electron variables E_e and θ_e are well described, and the differences seen in figure 9.1 have largely disappeared. Both $p_T(D^{\star\pm})$ and $\eta(D^{\star\pm})$ are well described, however a discrepancy exists in the highest two bins of $p_T(D^{\star\pm})$, where the data lies below the Monte Carlo. This discrepancy feeds through into the transverse energy of the highest E_T jet. The same effect has been observed in other recent heavy flavour analyses [96].

The description of the data when jets are reconstructed with energy corrected ZUFOs in the photon-proton centre of mass frame is shown in Figure 9.3. Again the description of all variables is good, with the largest difference occurring in the description of the electron polar angle θ_e. The characteristics of the variables are identical to those described above, although the description of $p_T(D^{\star\pm})$ is improved.

9.4 Acceptance Correction

An acceptance correction was applied to the measured uncorrected distributions on a bin-by-bin basis (in bins of high and low x_γ^{OBS} and Q^2) to unfold back to the hadron level. The calculation can be thought of as a three step procedure:

1. For each bin of Q^2 and x_γ^{OBS} count the number of Monte Carlo events detected in the bin (i.e. reconstructed from detector level quantities), the number generated in the bin (i.e. reconstructed from generator level quantities) and the number both generated and detected in the bin.

2. Calculate the purity and efficiency in each bin, where;

$$purity = \frac{\#\ generated\ and\ detected\ in\ bin}{\#\ detected\ in\ bin}$$
$$efficiency = \frac{\#\ generated\ and\ detected\ in\ bin}{\#\ generated\ in\ bin}.$$

3. Calculate the acceptance correction factor given by;

$$correction = \frac{purity}{efficiency} = \frac{\#\ generated\ in\ bin}{\#\ detected\ in\ bin}$$

Dissecting the quantities calculated above it can be seen that the purity gives the fraction of events reconstructed by the detector in a bin which are also generated in the bin, and the efficiency gives the fraction of events generated in a bin which were also detected in the bin. It is important that both the purity and efficiency are high in order for the dependence of the measurement on the Monte Carlo model used to be low.
Figures 9.4-9.6 show the purity, efficiency and correction factors as a function of Q^2 in bins of x_γ^{OBS} for the three different methods of hadronic final state reconstruction. The plots support the expectation that the purity of the energy corrected sample (figure 9.5 and 9.6) is greater than that of the uncorrected calorimeter cell sample (figure 9.4). This then accounts for the loss of statistics when moving from uncorrected calorimeter cells to corrected EFOs.
The differential cross section $d\sigma/dQ^2$ given the number of $D^{\star\pm}$ mesons in a bin N, the acceptance correction factor C and the integrated luminosity, $\int \mathcal{L}dt$ is given by,

$$\frac{d\sigma}{dQ^2} = \frac{N.C}{\int \mathcal{L}dt.(Q^2{}_{max} - Q^2{}_{min}).BR} \tag{9.1}$$

for a bin running from $Q^2{}_{min}$ to $Q^2{}_{max}$. The factor BR is the branching ratio for the process $D^{\star\pm} \rightarrow K\pi\pi_s$, given as $2.609 \pm 0.098\%$ [97].

9.5 Systematic Uncertainties

Sources of systematic uncertainty in the measurement were studied and quantified. The study was performed for the analyses using all three jet reconstruction techniques and included:

- Varying the cuts on the jet E_T and η by $\pm 1\sigma$. For uncorrected jets the transverse energy requirement was varied by ± 0.6 GeV(15%), and for corrected jets ± 0.1 GeV($\sim$ 1.5%). For all cases the η requirement was varied ± 0.1 units.

- Varying the cut on y_{JB} by $\pm 1\sigma$ (± 0.07).
- Varying the electron energy requirements by $\pm 1\sigma$. The photoproduction veto and the cut on the DIS electron were both varied at the same time (± 0.3 GeV in photoproduction and ± 0.7 GeV).
- Increasing the dimensions of the box cut by ± 1cm.
- Varying the cuts of the transverse momentum of the $\mathrm{D}^{\star\pm}$ decay products ($K\pi\pi_s$) by ± 10 MeV, which is roughly twice the CTD resolution [3] at the cut values.
- Increasing the width of the D^0 mass window by 20 MeV allowing a greater fraction of background events to enter the fit.
- Varying the mean and width of the Gaussian function fixed in the three parameter unbinned fit by $\pm 1\sigma$ (± 0.03 MeV for the mean and width of the Gaussian.).
- Using the HERWIG [50] Monte Carlo to perform the acceptance correction.
- Scaling only the Monte Carlo calorimeter quantities $E_{\mathrm{T}}^{\mathrm{jet}}$ and y_{JB} by $\pm 5\%$ [35]. This is at the upper limit of the uncertainty in the calorimeter energy scale between data and Monte Carlo [34] .

The effect on the ratio of low to high x_γ^{OBS} cross sections expressed as a fractional change in the ratio is shown in figure 9.7. The first five plots moving down the left are the systematic uncertainties arising when event selection is performed on jets reconstructed with uncorrected calorimeter cells in five bins of Q^2. The five plots on the right are the systematic uncertainties obtained when jets were reconstructed with corrected ZUFOs in the laboratory frame. The remaining plots (bottom left) are for the analysis performed in the photon-proton centre of mass frame. The green band on each figure represents the statistical error in each of the bins of Q^2.

All of the systematic uncertainties lie within the statistical errors for all jet reconstruction methods and bins of Q^2. The dominant uncertainty generally arises from varying the requirement on the estimator y_{JB}. A large effect is also caused by using HERWIG to perform acceptance corrections, although the error is still within the statistical error. Widening the box cut also has an effect on

the ratio between $1.5 < Q^2 < 4.5$ GeV^2, especially when using uncorrected calorimeter cells to reconstruct the jets. In photoproduction a significant effect is observed from widening the D^0 mass window, which is not generally seen in DIS.

9.6 Corrected Measurements

The measured high and low x_γ^{OBS} cross sections as a function of Q^2 in the laboratory frame and photon-proton centre of mass frame are shown in figures 9.8 and 9.9. The measured acceptance corrected ratios, with statistical and systematic uncertainties are shown in figure 9.10, for each of the jet reconstruction methods. The upper plot was produced to mirror a previous analysis [12], which agrees well with the measurement shown here. Future discussions will however concentrate on the bottom two plots, where the improved reconstruction method was used in the laboratory and photon-proton centre of mass frame respectively.

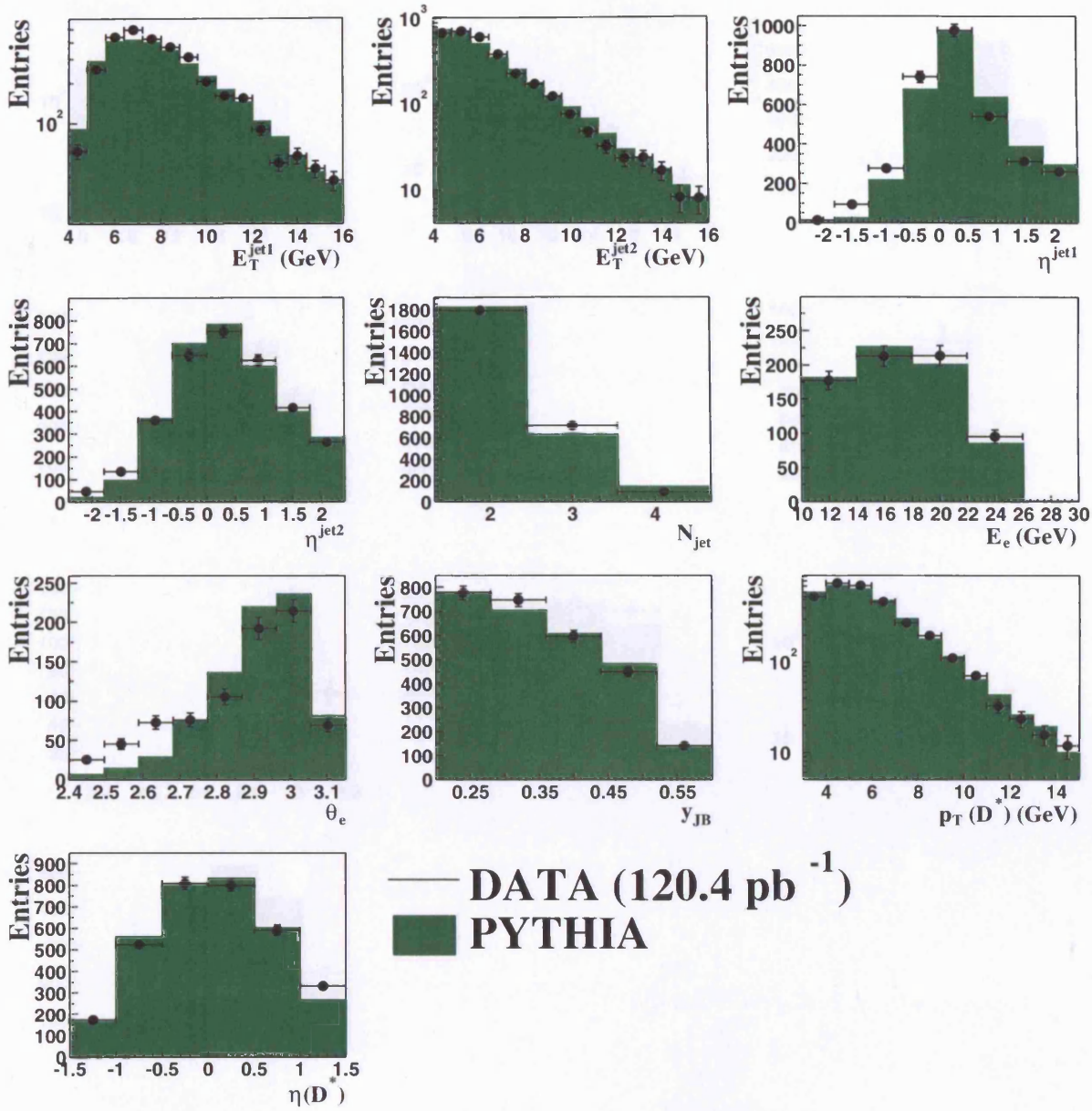

Figure 9.1: *Comparison of data (dots) and Monte Carlo (histogram) for event, jet and $D^{*\pm}$ properties with jets reconstructed from uncorrected calorimeter cells in the laboratory frame.*

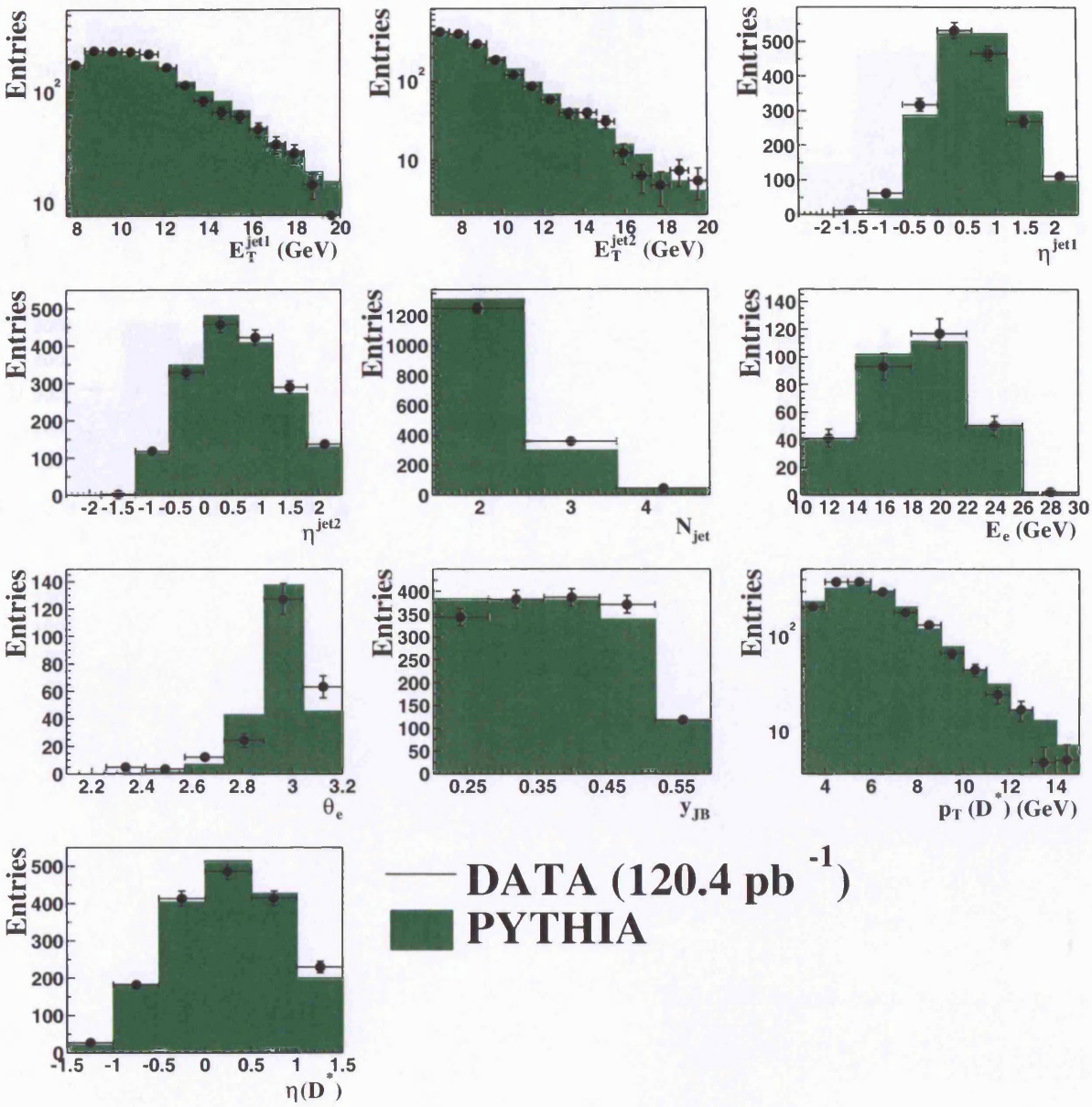

Figure 9.2: *Comparison of data (dots) and Monte Carlo (histogram) for event, jet and $D^{*\pm}$ properties with jets reconstructed from corrected ZUFOs in the laboratory frame.*

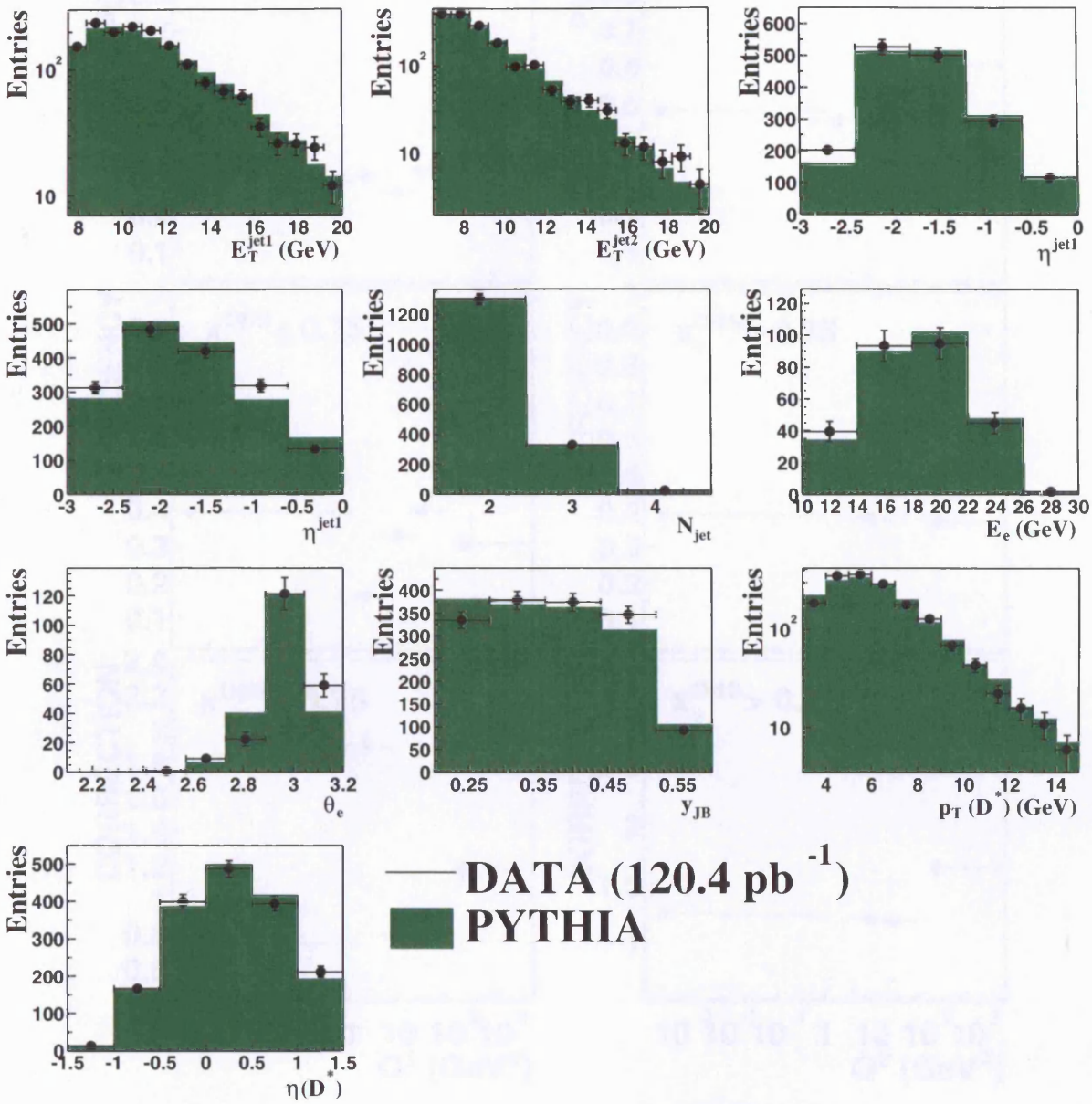

Figure 9.3: *Comparison of data (dots) and Monte Carlo (histogram) for event, jet and $D^{\star\pm}$ properties with jets reconstructed from corrected ZUFOs in the photon-proton centre of mass frame.*

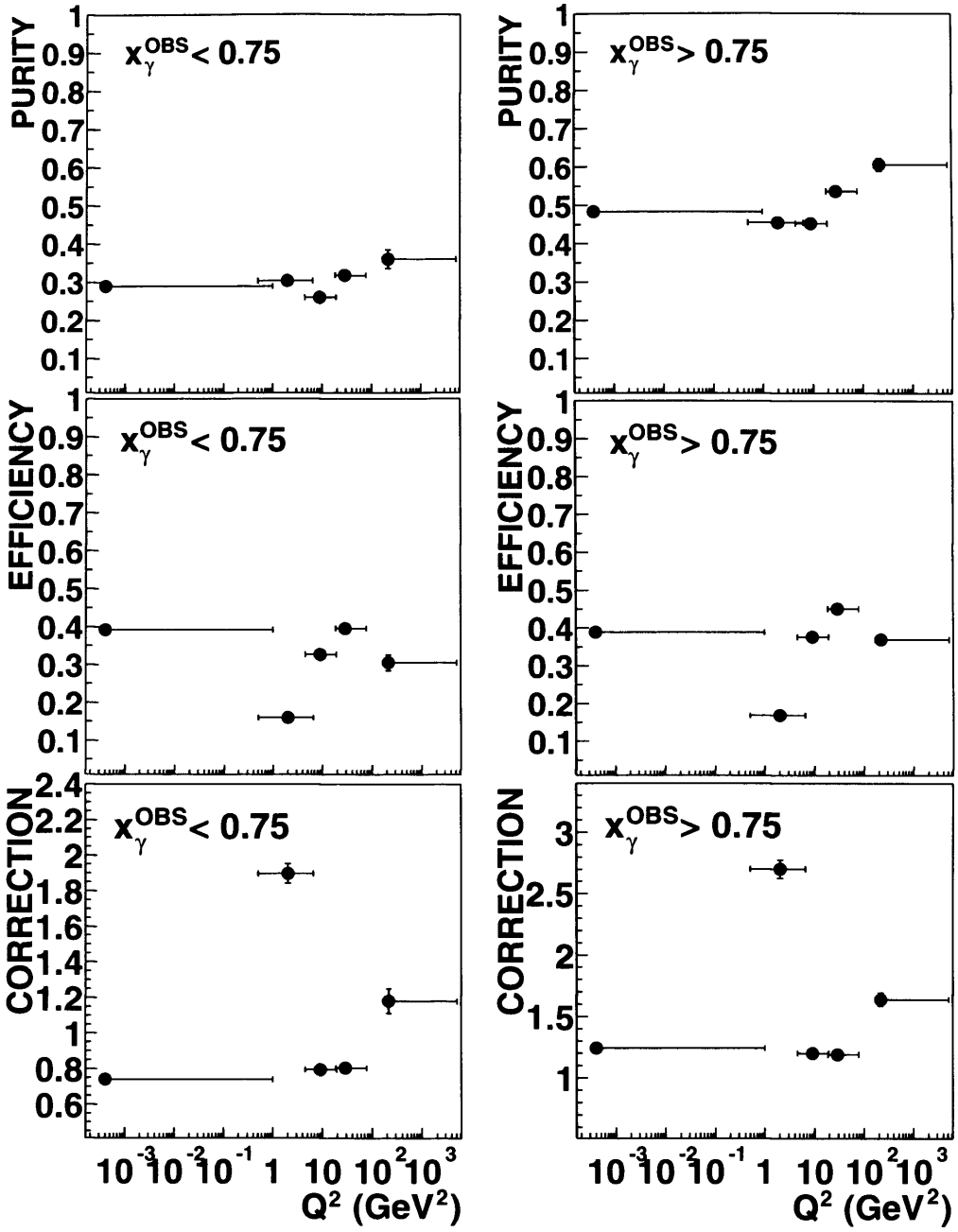

Figure 9.4: *Purity, efficiency and correction factor used for unfolding procedure as a function of Q^2 in bins of low $(x_\gamma^{\rm OBS} < 0.75)$ and high $(x_\gamma^{\rm OBS} > 0.75)$ $x_\gamma^{\rm OBS}$. The values shown are those obtained with jets reconstructed from calorimeter cells in the laboratory frame.*

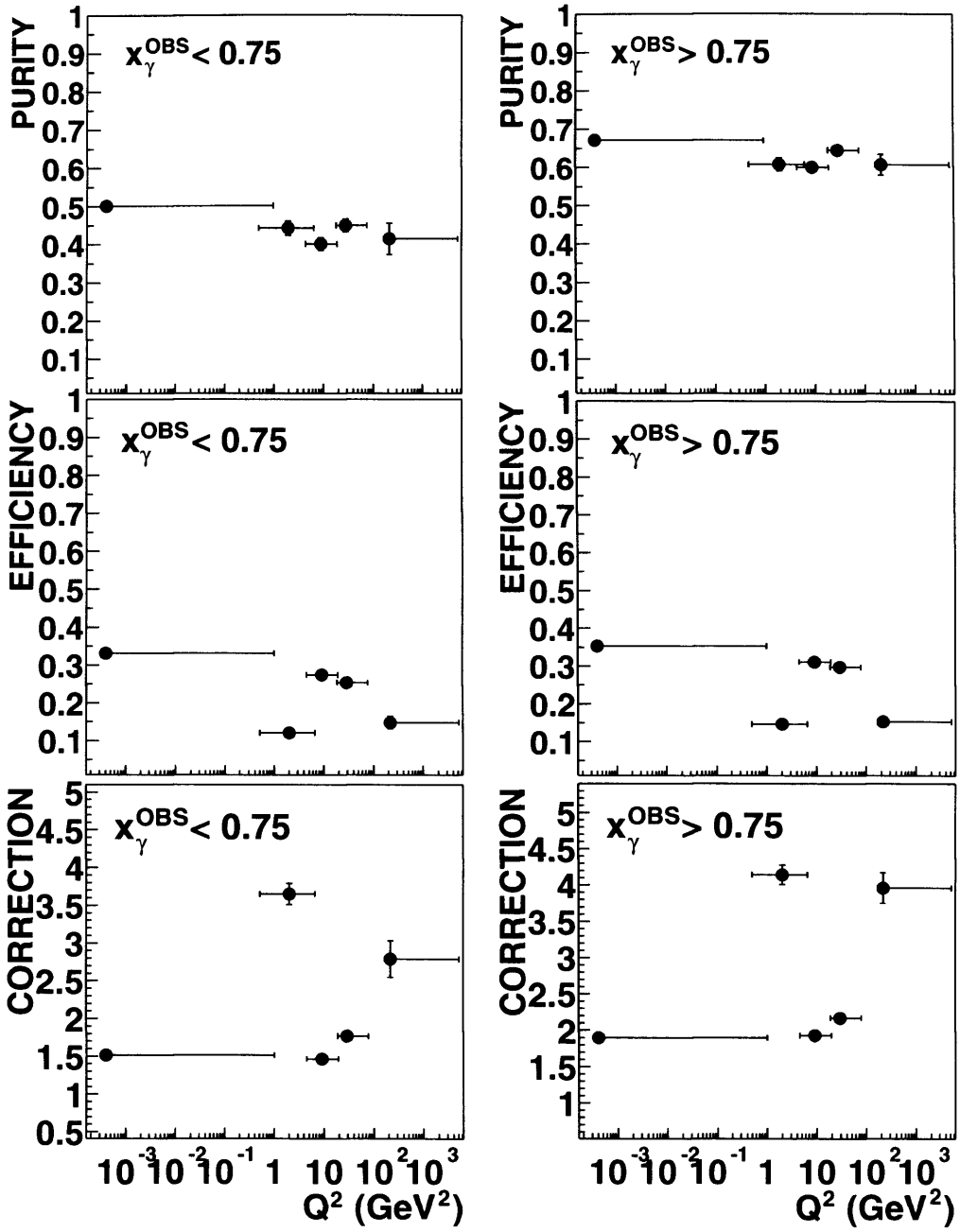

Figure 9.5: *Purity, efficiency and correction factor used for unfolding procedure as a function of Q^2 in bins of low $(x_\gamma^{\rm OBS} < 0.75)$ and high $(x_\gamma^{\rm OBS} > 0.75)$ $x_\gamma^{\rm OBS}$. The values shown are those obtained with jets reconstructed from EFOs in the laboratory frame.*

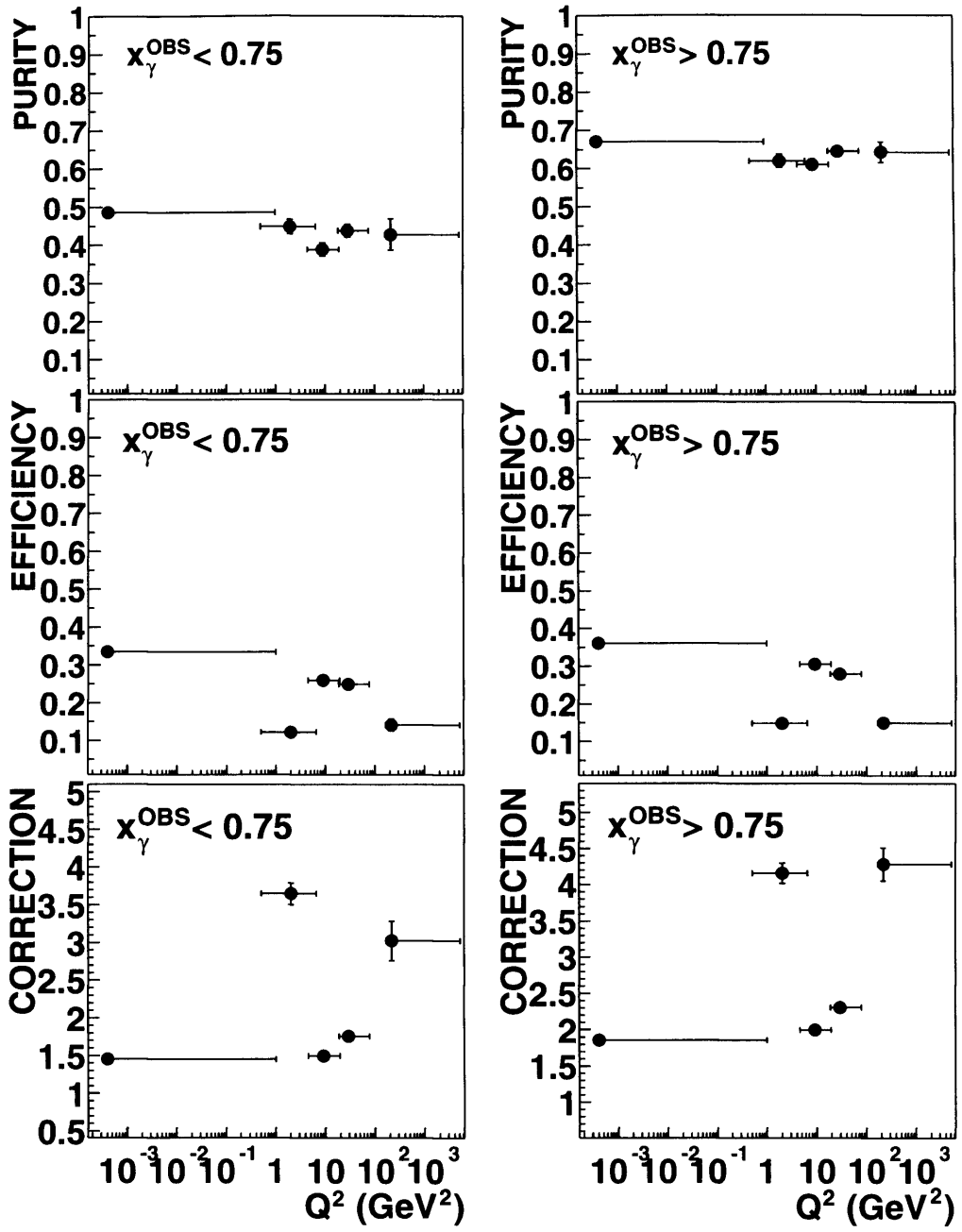

Figure 9.6: *Purity, efficiency and correction factor used for unfolding procedure as a function of* Q^2 *in bins of low* $(x_\gamma^{\rm OBS} < 0.75)$ *and high* $(x_\gamma^{\rm OBS} > 0.75)$ $x_\gamma^{\rm OBS}$. *The values shown are those obtained with jets reconstructed from EFOs in the photon-proton center of mass frame.*

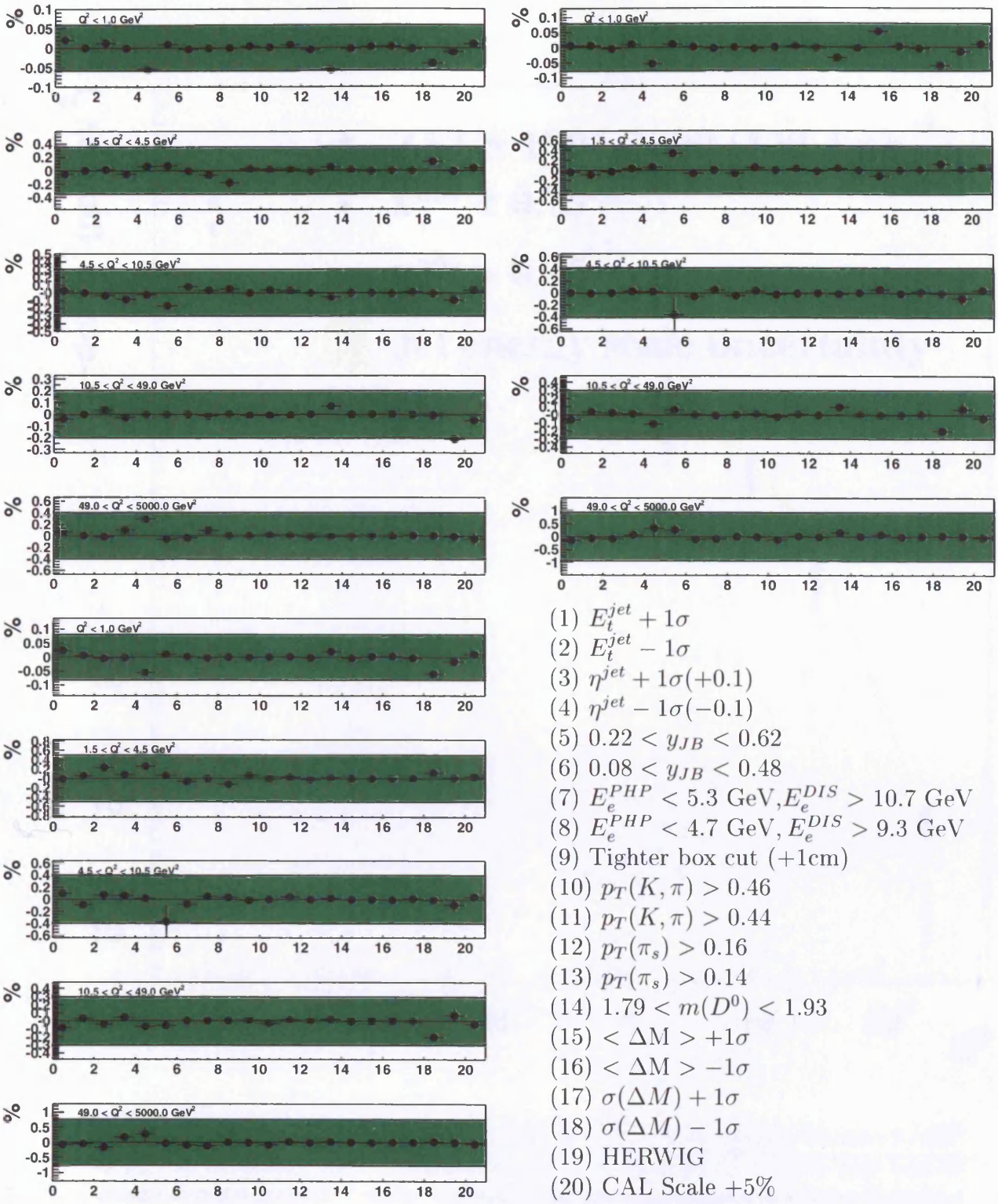

(1) $E_t^{jet} + 1\sigma$
(2) $E_t^{jet} - 1\sigma$
(3) $\eta^{jet} + 1\sigma(+0.1)$
(4) $\eta^{jet} - 1\sigma(-0.1)$
(5) $0.22 < y_{JB} < 0.62$
(6) $0.08 < y_{JB} < 0.48$
(7) $E_e^{PHP} < 5.3$ GeV,$E_e^{DIS} > 10.7$ GeV
(8) $E_e^{PHP} < 4.7$ GeV, $E_e^{DIS} > 9.3$ GeV
(9) Tighter box cut (+1cm)
(10) $p_T(K,\pi) > 0.46$
(11) $p_T(K,\pi) > 0.44$
(12) $p_T(\pi_s) > 0.16$
(13) $p_T(\pi_s) > 0.14$
(14) $1.79 < m(D^0) < 1.93$
(15) $< \Delta M > +1\sigma$
(16) $< \Delta M > -1\sigma$
(17) $\sigma(\Delta M) + 1\sigma$
(18) $\sigma(\Delta M) - 1\sigma$
(19) HERWIG
(20) CAL Scale +5%
(21) CAL Scale −5%

Figure 9.7: *Systematic uncertainties on the measurements due to kinematic cuts, fitting method, Monte Carlo model and the jet energy scale uncertainty. The uncertainties are separated into five regions of Q^2 for jets reconstructed with uncorrected calorimeter cells in the laboratory frame (top left), corrected ZUFOs in the laboratory frame (top right) and corrected ZUFOs in the photon-proton centre of mass frame (bottom left).*

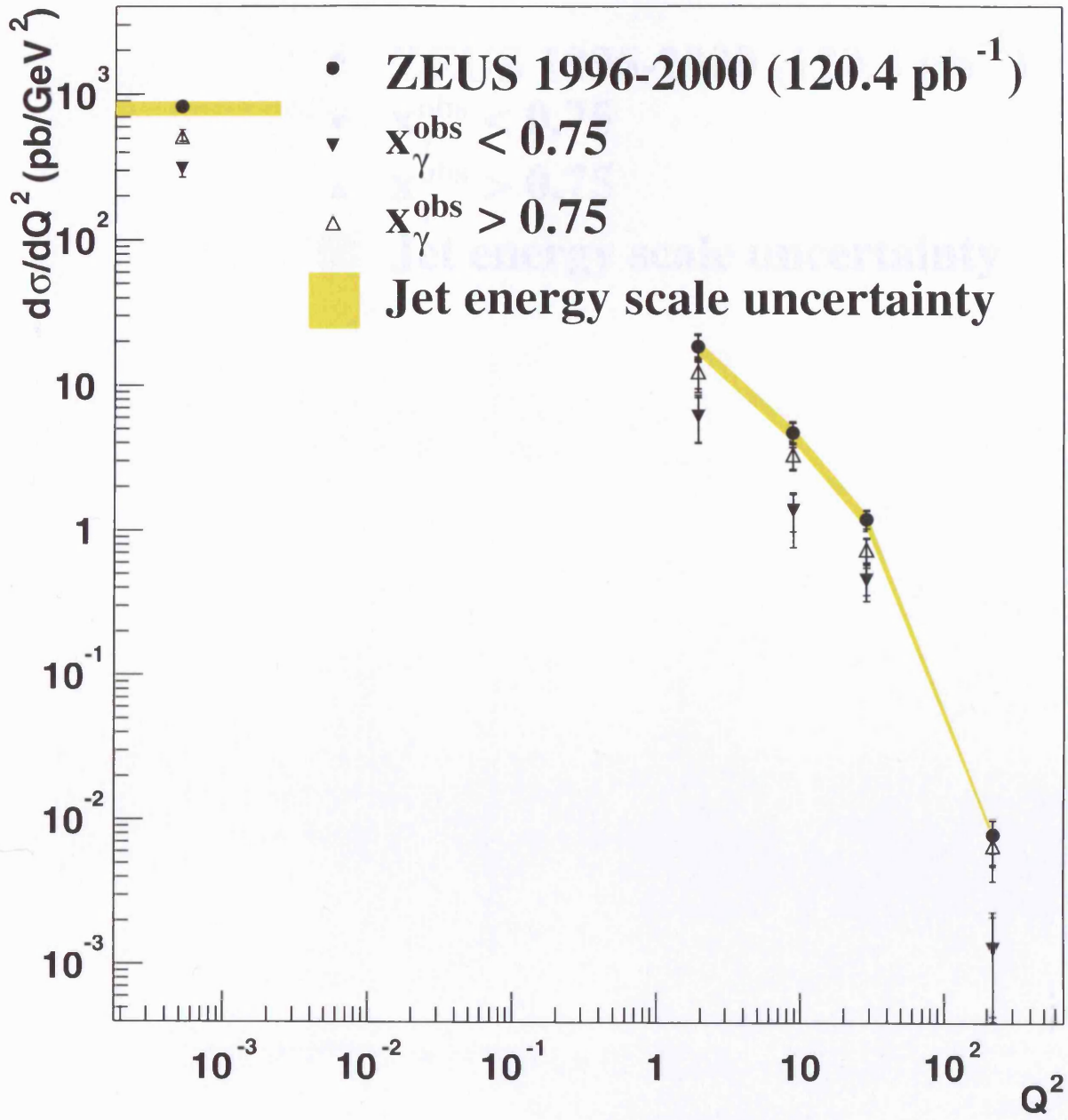

Figure 9.8: *Measured dijet cross-sections $d\sigma/dQ^2$ for $x_\gamma^{\mathrm{OBS}} > 0.75$ (upwards triangles) $d\sigma/dQ^2$ for $x_\gamma^{\mathrm{OBS}} < 0.75$ (downwards triangles) and $d\sigma/dQ^2$ for the whole x_γ^{OBS} region (black dots), for events with an associated $\mathrm{D}^{\star\pm}$ meson. The measurements were performed using jet reconstructed from corrected ZUFOs in the laboratory frame.*

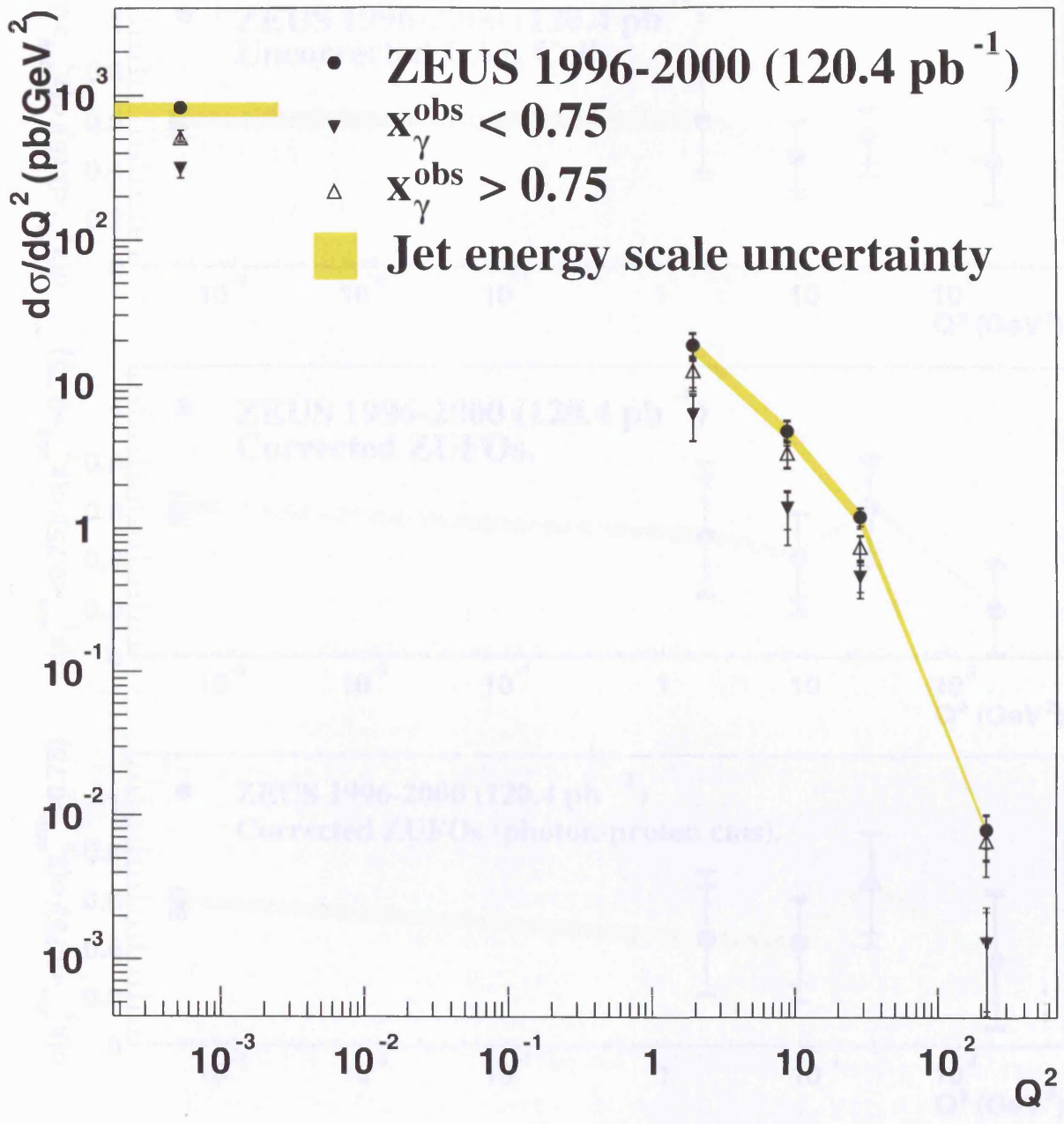

Figure 9.9: *Measured dijet cross-sections $d\sigma/dQ^2$ for $x_\gamma^{\mathrm{OBS}} > 0.75$ (upwards triangles) $d\sigma/dQ^2$ for $x_\gamma^{\mathrm{OBS}} < 0.75$ (downwards triangles) and $d\sigma/dQ^2$ for the whole x_γ^{OBS} region (black dots), for events with an associated $\mathrm{D}^{\star\pm}$ meson. The measurements were performed using jet reconstructed from corrected ZUFOs in the photon-proton centre of mass frame.*

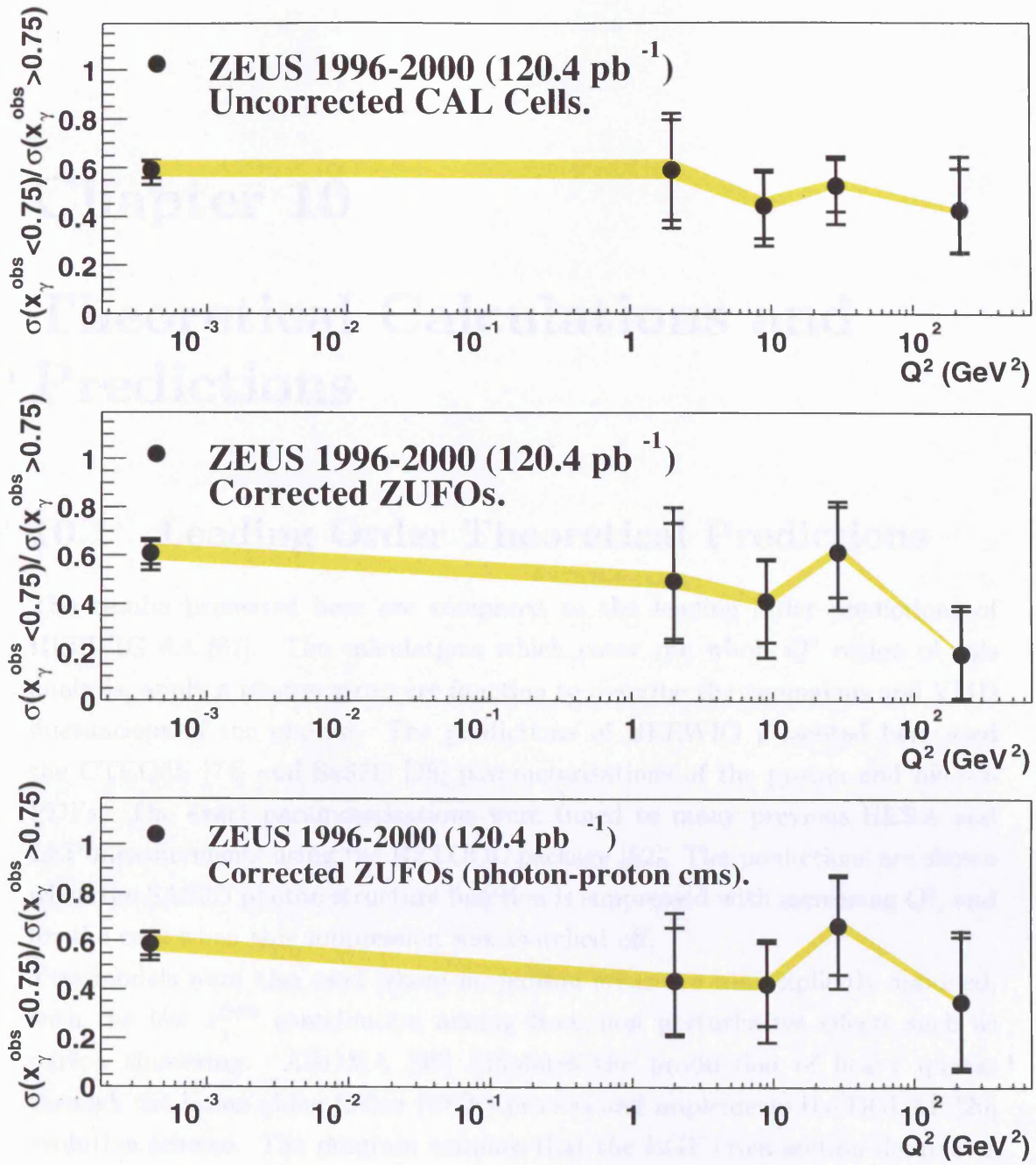

Figure 9.10: *Ratio of low to high x_γ^{OBS} cross sections for dijet events with an associated $\mathrm{D}^{*\pm}(2010)$ meson. The ratio is shown for jets reconstructed with uncorrected calorimeter cells in the laboratory frame (top), corrected ZUFOs in the laboratory frame (middle) and corrected ZUFOs in the photon-proton centre of mass frame (bottom). The shaded band represents the uncertainty due to the difference in absolute jet energy scale between data and MC.*

Chapter 10

Theoretical Calculations and Predictions

10.1 Leading Order Theoretical Predictions

The results presented here are compared to the leading order predictions of HERWIG 6.4 [61]. The calculations which cover the whole Q^2 region of this analysis, apply a photon structure function to describe the anomalous and VMD fluctuations of the photon. The predictions of HERWIG presented here used the CTEQ5L [74] and SaS2D [28] parameterisations of the proton and photon PDFs. The exact parameterisations were tuned to many previous HERA and LEP measurements using the HZTOOL package [62]. The predictions are shown when the SAS2D photon structure function is suppressed with increasing Q^2, and for the case when this suppression was switched off.

Two models were also used where no photon structure was explicitly assumed, with the low x_γ^{OBS} contribution arising from non perturbative effects such as parton showering. AROMA [98] simulates the production of heavy quarks through the boson gluon fusion (BGF) process and implements the DGLAP [20] evolution scheme. The program assumes that the BGF cross section dominates over the production of heavy quarks through other processes such as resolved hadroproduction. AROMA includes a treatment of hadronisation based on the Lund string model. CASCADE [99] which implements the CCFM [22] evolution equation to generate initial state parton cascades, is also compared to the ratio of cross sections.

10.2 Next to Leading Order Theoretical Predictions

No single next-to-leading order calculation exists which is applicable for the production of heavy quarks over the whole Q^2 range of this analysis. The photoproduction cross sections were calculated independently from DIS using the heavy flavour production code of Frixione, Mangano, Nason and Ridolfi (FMNR) [80]. HVQDIS [90] was used to compute heavy flavour cross sections in DIS. In both models charm is produced dynamically and is not treated as an active flavour in the proton. A more detailed discussion now follows.

10.2.1 Photoproduction

FMNR calculates the point-like (direct) and hadronic (resolved) cross sections separately, the sum of the two contributions then gives a physically meaningful cross section at next-to-leading order. The point-like component is generated according to the formalism described in [100]. The CTEQ5M1 [74] parameterisation of the proton PDF was used, which uses the $\overline{\text{MS}}$ scheme to renormalise the running coupling, with $\Lambda_{QCD} = 226$ GeV. The hadronic component was calculated using a generalisation of the hadroproduction method described in [101]. The GRV-G HO [52] structure function was used for the photon PDFs, which uses the DIS renormalisation scheme. In the calculation of both the direct and resolved contribution the mass of the charm quark was set to $m_c = 1.5$ GeV.

10.2.2 Deep Inelastic Scattering

The HVQDIS [90] program calculates charm production cross sections in the DIS region studied in this analysis ($Q^2 > 1.5$ GeV^2). Only the point-like contribution to the total cross section is considered, using the formalism of Harris and Smith [103] for calculating exclusive cross sections. The next-to-leading order QCD matrix elements are calculated in an approach where the number of flavours is fixed to three. This restricts the available choice of proton PDFs to those with fixed flavour schemes, where $N_f = 3$ for renormalising the running coupling α_s. The CTEQ5F3 [74] parameterisation was used because it was the most recent set at time of writing that satisfied the above requirements. The mass of the charm quark was fixed to $m_c = 1.5$ GeV.

10.3 Peterson Fragmentation

Fragmentation is a non-perturbative effect caused by the heavy quark combining with lighter quarks, produced in the vacuum (and colour field) around it, to form baryons or mesons that can be measured in the detector. The above calculations however only produce a charmed $Q\overline{Q}$ pair, and a non-perturbative model must be applied to account for the fragmentation $c \rightarrow \mathrm{D}^{\star\pm}$ if the calculations are to be compared to the measured cross sections. In both the photoproduction and DIS calculations the Peterson fragmentation model [104] was used to relate the momentum of the final state charmed hadron to the charm quark from which it originated. The form of the fragmentation function is

$$D_{c\rightarrow D^{\star}}(z,\epsilon) = \frac{Nz(1-z)^2}{[(1-z)^2+\epsilon z]^2} \tag{10.1}$$

which is equivalent to the fraction of the charm quark momentum, z, carried by the $\mathrm{D}^{\star\pm}$ meson. The factor ϵ cannot be calculated or measured directly, but must be extracted from phenomenological fits to data. In both the photoproduction and DIS calculation the value $\epsilon = 0.035$ [105] was used.

10.4 Hadronisation Corrections

To estimate the effects of parton showering and hadronisation a hadronisation correction, C_{HAD} was calculated from the leading order HERWIG [50] Monte Carlo generator. Cross sections were generated at the level of the emerging partons, $d\sigma^{parton}$ and at the level of the final state hadrons, $d\sigma^{hadron}$. The Peterson function was again used to adjust the outgoing heavy quark momentum for fragmentation effects. The partonic cross sections were then multiplied by the fraction of charm quarks fragmenting into $\mathrm{D}^{\star\pm}$s, $f(c \rightarrow \mathrm{D}^{\star\pm})$, the value of which was taken to be 0.235 [106]. C_{HAD} was then calculated and applied to the NLO predictions following and identical method to that described in section 5.7.

Chapter 11

Results and Conclusions

The ratio $R = \sigma(x_\gamma^{\mathrm{OBS}} < 0.75)/\sigma(x_\gamma^{\mathrm{OBS}} > 0.75)$ for a wide range of photon virtualities Q^2 using the three different methods of jet reconstruction are shown together in figure 11.1. The differences between the measurements are small, and all three are consistent with one another within the statistical and systematic uncertainties of the measurement. The inner error bars show the statistical uncertainty on each of the measurements. The outer error bars show the systematic errors added in quadrature to the statistical error. The ratio, which is sensitive to effects of photon structure, is consistent with being flat with increasing Q^2 in marked contrast to the "all-flavours" measurement of figures 6.7 and 6.8. The result in the laboratory frame is roughly consistent with the result in the photon-proton centre of mass frame, within the large uncertainties of the measurement.

The validity of applying the different approaches to describing the photon within pQCD discussed in chapter 10 is now discussed in the light of this result. A discussion of the next to leading order QCD predictions of Frixione-Mangano-Nason-Ridolfi (FMNR) [80], and HVQDIS [90] also follows.

11.1 Leading Order pQCD Theoretical Predictions

11.1.1 Comparison to Models without γ PDF

Figure 11.2 shows the measured ratio compared to the predictions of AROMA and CASCADE. These models do not explicitly implement a treatment of the photon structure, however in both models a significant fraction of the total cross

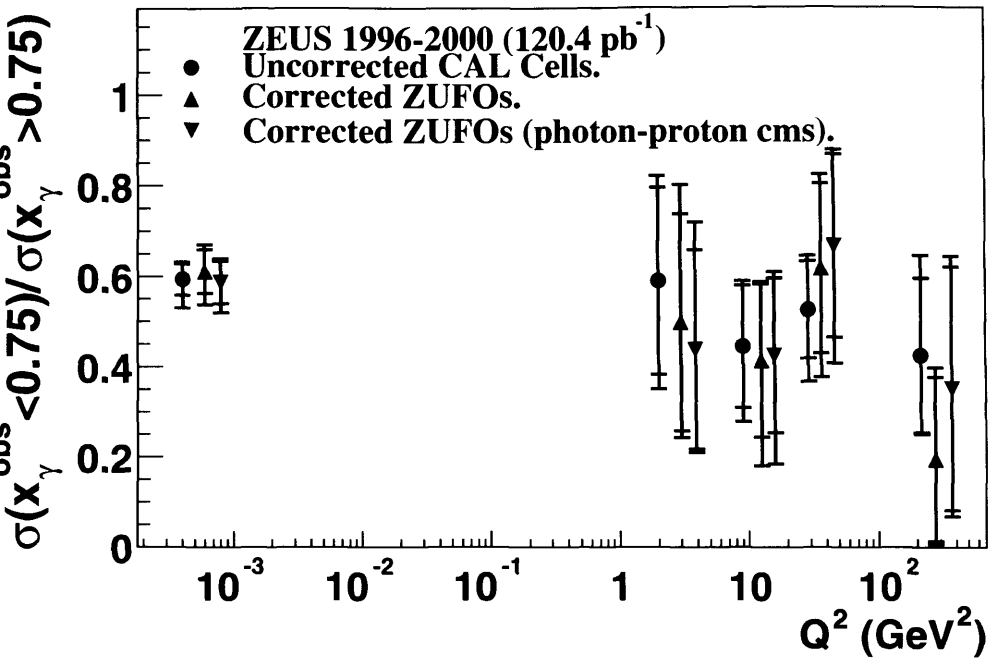

Figure 11.1: *Ratio of low to high x_γ^{OBS} cross sections for dijet events with an associated $\mathrm{D}^{\star\pm}(2010)$ meson. The ratio is shown for jets reconstructed with uncorrected calorimeter cells in the laboratory frame (dots), corrected ZUFOs in the laboratory frame (up triangle) and corrected ZUFOs in the photon-proton centre of mass frame (down triangle).*

section is generated in the low x_γ^{OBS} region ($x_\gamma^{\mathrm{OBS}} < 0.75$). Both models produce a roughly flat behaviour of the ratio with increasing Q^2, however differences in the absolute value of the ratio exist between the models.

In the laboratory frame (upper plot) the prediction of AROMA implementing the DGLAP evolution scheme is consistent with the data within the large uncertainties of the measurement for $Q^2 > 1.5$ GeV^2. In the photoproduction region, $Q^2 < 1.0$ GeV^2, where the effects of photon structure are expected to be most significant, the prediction lies below the data. The prediction of CASCADE implementing the CCFM evolution scheme lies above AROMA across the whole Q^2 region, and is again consistent with the data for $Q^2 > 1.5$ GeV^2. CASCADE lies closer to the data than AROMA for $Q^2 < 1.0$ GeV^2, however still does not describe the ratio in this region.

In the photon-proton centre of mass frame (lower plot) the prediction of AROMA is consistent with the prediction in the laboratory frame, lying below the data in the low Q^2 region. CASCADE exhibits unusual behaviour under the boost, with the absolute value of the predicted ratio reduced by approximately 50%, while the shape is unchanged. The effect was studied and the x_γ^{OBS} distribution found to be harder when jets are selected in the photon-proton centre of mass frame,

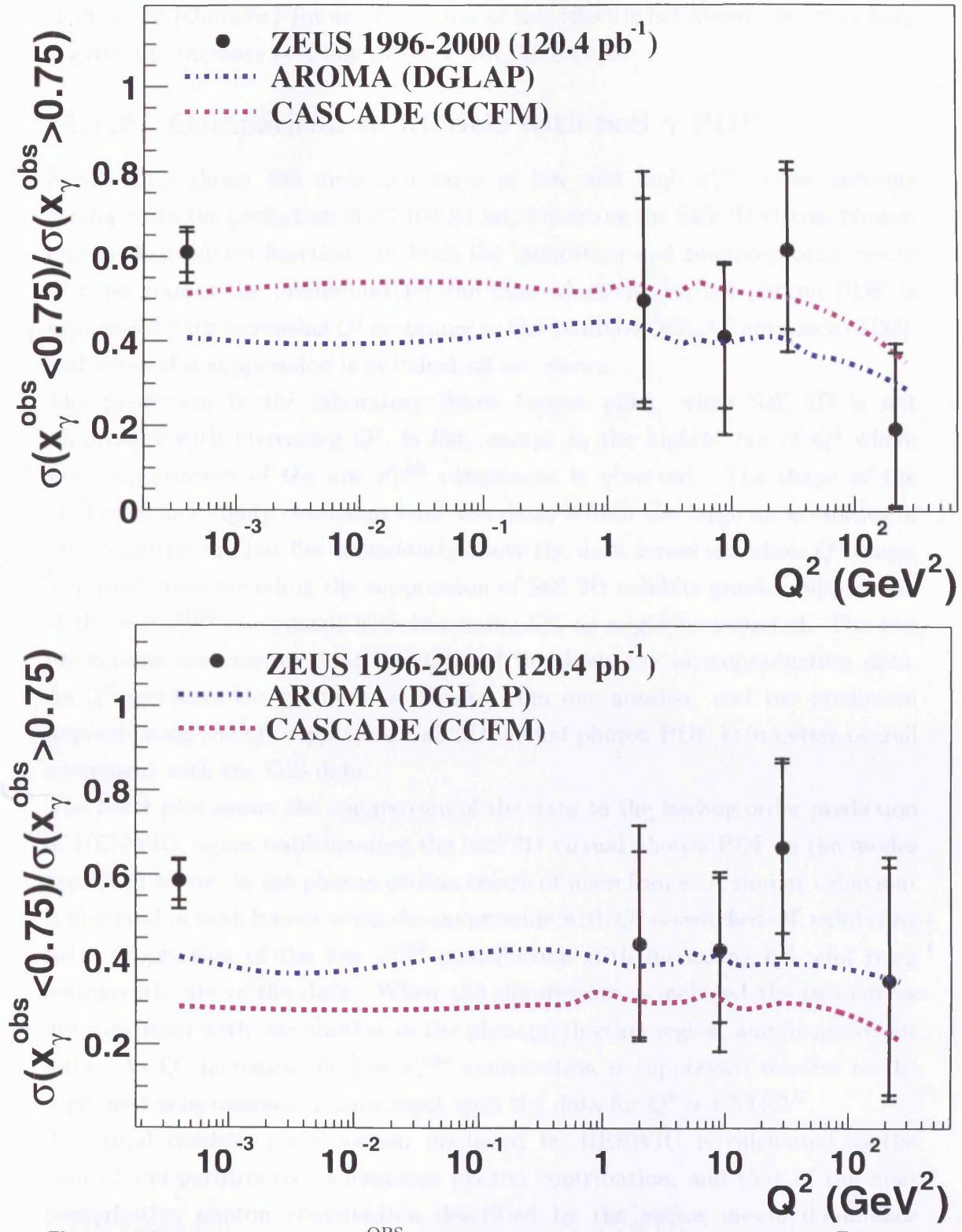

Figure 11.2: *Ratio of low to high x_γ^{OBS} cross sections for dijet events with an associated D^* in the laboratory frame (top) and the photon-proton centre of mass frame (bottom), compared to the leading order predictions of AROMA and CASCADE.*

than in the laboratory frame. The cause of this effect is not known, however may suggest the presence of a bug in the CASCADE code.

11.1.2 Comparison to Models with SaS γ PDF

Figure 11.3 shows the measured ratio of low and high x_γ^{OBS} cross sections compared to the prediction of HERWIG implementing the SaS 2D virtual photon parton distribution function. In both the laboratory and photon-proton centre of mass frames the predictions for the case when the virtual photon PDF is suppressed with increasing Q^2 according to the modified DGLAP approach of [28], and when this suppression is switched off are shown.

The prediction in the laboratory frame (upper plot), when SaS 2D is not suppressed with increasing Q^2, is flat, except in the highest bin of Q^2 where some suppression of the low x_γ^{OBS} component is observed. The shape of the prediction is roughly consistent with the data, within the large uncertainties of the measurement, but lies consistently above the data across the whole Q^2 range. The prediction including the suppression of SaS 2D exhibits greater suppression of the low x_γ^{OBS} component with increasing Q^2, as might be expected. The two predictions are consistent at low Q^2 and lie above the photoproduction data. As Q^2 increases the predictions deviate from one another, and the prediction implementing the Q^2 suppressed SaS 2D virtual photon PDF is in better overall agreement with the DIS data.

The lower plot shows the comparison of the data to the leading order prediction of HERWIG, again implementing the SaS 2D virtual photon PDF in the modes described above, in the photon-proton centre of mass frame. A similar behaviour is observed in both frames when the suppression with Q^2 is switched off, exhibiting little suppression of the low x_γ^{OBS} contribution with increasing Q^2, and lying consistently above the data. When the suppression is included the two curves are consistent with one another in the photoproduction region, and lie above the data. As Q^2 increases the low x_γ^{OBS} contribution is suppressed relative to the high, and is in reasonable agreement with the data for $Q^2 > 1.5$ GeV^2.

The total resolved cross section predicted by HERWIG is calculated as the sum of the perturbative anomalous photon contribution, and that of the non-perturbative photon contribution described by the vector meson dominance (VMD) model. The contribution of the non-perturbative component of the photon was investigated by removing its contribution from the sum. The effect

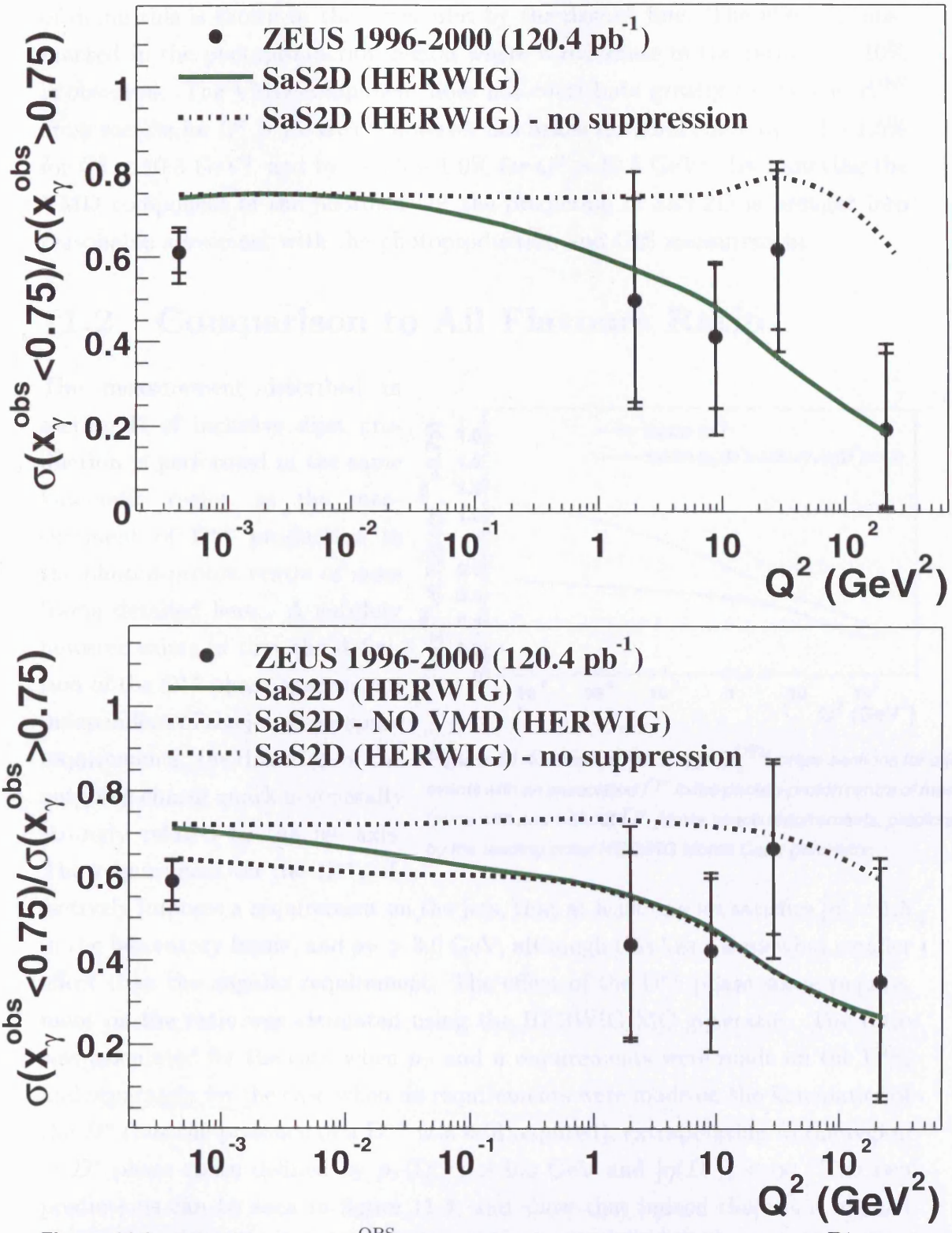

Figure 11.3: *Ratio of low to high x_γ^{OBS} cross sections for dijet events with an associated D^* in the laboratory frame (top) and the photon-proton centre of mass frame (bottom) compared to the leading order predictions of HERWIG implementing the SaS 2D virtual photon PDF.*

of doing this is shown in the lower plot by the dashed line. The effect is most marked in the photoproduction region where a reduction in the ratio of $\sim 10\%$ is observed. The VMD component does not contribute greatly to the low $x_\gamma^{\rm OBS}$ cross section for $Q^2 > 1.5$ GeV^2, however lies below the solid curve by $\sim 1-1.5\%$ for $Q^2 < 10.5$ GeV^2, and by $\sim 0.5-1.0\%$ for $Q^2 > 10.5$ GeV^2. By removing the VMD component of the photon PDF the prediction of SaS 2D is brought into reasonable agreement with the photoproduction and DIS measurement.

11.2 Comparison to All Flavours Ratio

The measurement described in section II of inclusive dijet production is performed in the same kinematic region as the measurement of D$^{*\pm}$ production in the photon-proton centre of mass frame detailed here. A subtlety however exists in that the definition of the D$^{*\pm}$ phase space is not independent of the jet phase space requirements, the direction of the outgoing charm quark is generally strongly related to the jet axis. The requirement on the D$^{*\pm}$, effectively imposes a requirement on the jets, that at least one jet satisfies $|\eta| < 1.5$ in the laboratory frame, and $p_{\rm T} > 3.0$ GeV, although this has a somewhat smaller effect than the angular requirement. The effect of the D$^{*\pm}$ phase space requirement on the ratio was estimated using the HERWIG MC generator. The ratio was calculated for the case when p_T and η requirements were made on the D$^{*\pm}$, and separately for the case when no requirements were made on the kinematics of the D^* (but the presence of a D$^{*\pm}$ was still required), extrapolating to the region of D^* phase space defined by p_T(D$^{*\pm}$) > 0.0 GeV and $|\eta(D^*)| < \infty$. The two predictions can be seen in figure 11.4, and show that indeed there is a marked suppression of the ratio caused by the D$^{*\pm}$ phase space requirement. The effect is greatest for $Q^2 < 1.0$ GeV^2 where the D$^{*\pm}$ demand suppresses the ratio by

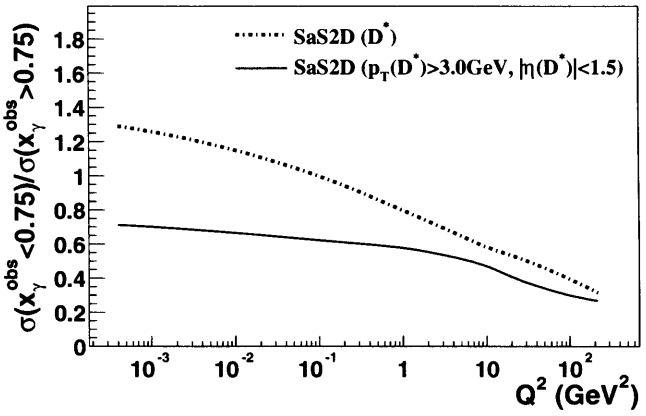

Figure 11.4: *Ratio of low to high $x_\gamma^{\rm OBS}$ cross sections for dijet events with an associated D^* in the photon-proton centre of mass frame with and without D^* phase space requirements, predicted by the leading order HERWIG Monte Carlo generator.*

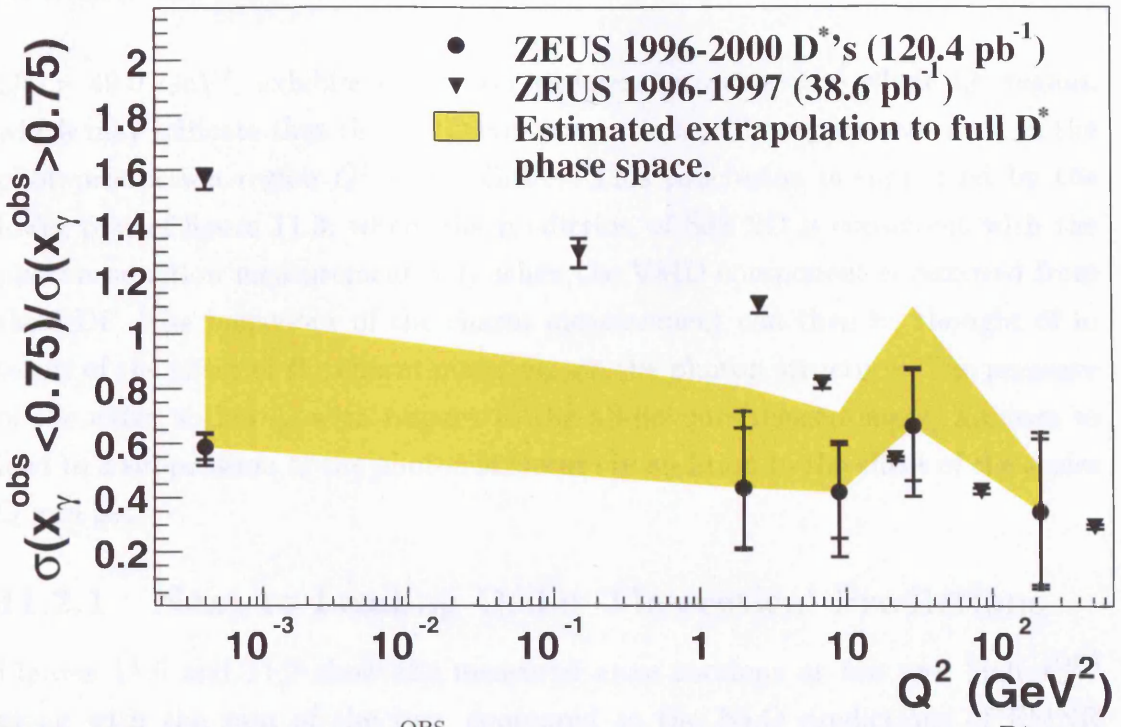

Figure 11.5: *Ratio of low to high x_γ^{OBS} cross sections for dijet events with an associated D^* in the photon-proton centre of mass frame compared to the ZEUS all flavours measurement performed in the same region of jet phase space. The shaded band represents the suppression of the charm tagged ratio due to the D^* phase space requirements estimated with the HERWIG Monte Carlo generator.*

$\sim 45\%$. In DIS the effect is smaller and reduces the ratio by $15 - 25\%$. Figure 11.5 shows the comparison of the charm tagged ratio to the all flavours ratio. The shaded band represents the predicted suppression due to the $D^{\star\pm}$ requirement, estimated from the method described above. Taking the band into account the conclusion that the ratio is roughly flat with increasing Q^2 remains valid within the large statistical and systematic uncertainties of the measurement. The all flavours measurement exhibits a steep decline of the ratio with increasing Q^2, particularly between $0.0 < Q^2 < 49.0$ GeV^2, in marked contrast to the charm tagged measurement. For $Q^2 > 49.0$ GeV^2 the all flavours measurement is consistent with that of the charm tagged measurement, showing a slight suppression of the ratio as Q^2 increases.

For $0.0 < Q^2 < 49.0$ GeV^2 the shape of the all flavours ratio may indicate a significant contribution from the heavily suppressed (Q^{-4}) VMD component of the photon. For $Q^2 > 49.0$ GeV^2 the shape indicates that the scale, Q^2, is large enough to effectively suppress the VMD component almost completely, leaving only the softer suppression ($\ln(\mu_R^2/Q^2)$) of the anomalous component. The charm tagged measurement, which is consistent with the all flavours measurement for

$Q^2 > 49.0$ GeV^2, exhibits this softer suppression across the whole Q^2 region, which may indicate that the VMD component is heavily suppressed, even in the photoproduction region $Q^2 < 1.0$ GeV^2. This conclusion is supported by the lower plot of figure 11.3, where the prediction of SaS 2D is consistent with the photoproduction measurement only when the VMD component is removed from the PDF. The behaviour of the charm measurement can then be thought of in terms of the effect of the charm mass, m_c, on the photon structure. The presence of the extra scale m_c, with respect to the all-flavours measurement, appears to lead to a suppression of the photon structure in addition to the effect of the scales Q and p_{T}.

11.2.1 Next to Leading Order Theoretical Predictions

Figures 11.6 and 11.7 show the measured cross sections at low and high x_γ^{OBS} along with the sum of the two, compared to the NLO predictions of FMNR and HVQDIS. The data and NLO are all laboratory frame quantities which are statistically favoured over the photon-proton centre of mass frame measurements. The yellow band represents the jet energy scale uncertainty on the total cross sections, the size of which is in the range $9 - 12\%$ except in the highest bin of Q^2 where it is $3 - 5\%$. The jet energy scale uncertainty is not shown individually for the low and high x_γ^{OBS} cross sections but is larger at low x_γ^{OBS} ($\sim 15\%$) than at high ($\sim 10\%$). The total cross sections (black circles) fall nearly five orders of magnitude across the whole Q^2 range. The low x_γ^{OBS} cross sections fall off more rapidly than the high, however the deviation of the two is less marked than in the all flavours measurement of figures 6.3 and 6.4, a fact reflected in the measured ratios of low to high x_γ^{OBS}.

Figure 11.6 shows the data compared to the NLO prediction of FMNR and HVQDIS with the renormalisation and factorisation scales set to $\mu_f^2 = \mu_R^2 = 4m_c^2$ in photoproduction and $\mu_f^2 = \mu_R^2 = Q^2 + m_c^2$ in DIS. The lower two plots show the differences between the data and NLO predictions, with the shaded band representing the renormalisation scale uncertainty estimated by varying the scales used, μ, by factors of 2 and 0.5. Hadronisation corrections were applied to the predictions following the method described in the previous chapter. The exact values of the hadronisation corrections factors applied is shown in table 11.1. These factors are applied according to the prescription $\sigma^{HAD} = C_{HAD}.\sigma^{NLO}$,

$Q^2(\mathrm{GeV}^2)$	hadronisation correction			
	$x_\gamma^{\mathrm{OBS}} < 0.75$	$x_\gamma^{\mathrm{OBS}} > 0.75$	Total	Ratio
$Q^2 < 0.0$	0.802308	0.732275	0.759492	1.09564
$1.5 < Q^2 < 4.5$	0.734474	0.737777	0.736609	0.995524
$4.5 < Q^2 < 10.5$	0.787577	0.744544	0.757882	1.0578
$10.5 < Q^2 < 49.0$	1.00165	0.76082	0.816151	1.31655
$49.0 < Q^2 < 5000.0$	1.94651	0.777145	0.899633	2.4942

Table 11.1: *Hadronisation corrections factors applied to the next-to-leading order calculations of FMNR (photoproduction) and HVQDIS (DIS), at low x_γ^{OBS}, high x_γ^{OBS}, the whole x_γ^{OBS} region and the ratio of low and high x_γ^{OBS}.*

where σ^{HAD} and σ^{NLO} are the cross sections at the hadron level and parton level respectively and C_{HAD} is the correction factor given in the above table.

The total cross sections are all well described by the predictions within the large statistical and theoretical uncertainties. The photoproduction prediction of the total cross section lies below the data in absolute value, however with the scale $\mu_f^2 = \mu_R^2 = 4m_c^2$ large uncertainties in the prediction are introduced due to terms beyond NLO, estimated by varying the scale using the method described above. The large uncertainty may be indicative that the chosen scale is not appropriate, and that a multiscale approach (p_T and m_c) is required. The theoretical uncertainty is reduced in the DIS sample where the predictions agree well with the data. The predictions of the low and high x_γ^{OBS} cross sections, where the theoretical uncertainties are comparable to those of the total cross sections and show no pronounced variation between the two regions of x_γ^{OBS}, both agree well with the data.

Figure 11.7 show the prediction of FMNR with the scale, $\mu_f^2 = \mu_R^2 = p_t^2 + m_c^2$, which reflects the fact that two scales are present in the photoproduction region. The prediction of HVQDIS is the same as that shown in the previous plot. The renormalisation scale dependence is smaller for the prediction of FMNR, and is closer to the uncertainty on the DIS prediction. The prediction of the total cross section lies below the photoproduction measurement, and does not describe the data. Both the low and high x_γ^{OBS} predictions are below the data by approximately the same amount.

Figure 11.8 shows the comparison of the measured ratio of low to high x_γ^{OBS} in the laboratory frame, compared to the same NLO predictions described above. In photoproduction the prediction of FMNR does not describe the data when

using the scale $\mu^2 = 4m_c^2$, with the predicted ratio lying above data. FMNR performs better when using the scale $\mu^2 = p_T^2 + m_c^2$, where the prediction gives a good descriptions of the data. The calculation of HVQDIS, which has no explicit treatment of the photon structure, using the scale $\mu^2 = Q^2 + m_c^2$ gives a reasonable description of the measured ratio for $Q^2 > 1.5$ GeV^2. The predicted ratio is roughly flat with increasing Q^2. It is also interesting to note that the renormalisation scale uncertainty on the predictions is significantly smaller for the ratio than for the independent cross sections, especially for the photoproduction prediction.

11.3 Summary and Conclusions

Dijet cross sections differential in Q^2 have been measured for events containing a $D^{\star\pm}(2010)$ meson in the laboratory and photon-proton centre of mass frames for a wide range of photon virtualities $0.0 < Q^2 < 5000.0$ GeV^2. In the laboratory frame (tables 11.2 - 11.4) the dijet selection was performed in the kinematic region, $E_T^{jet1,2} > 6.5, 7.5$ GeV^2 and $|\eta^{jet}| < 2.4$. In the photon-proton centre of mass frame (table 11.5 - 11.7) the requirements were $E_T^{jet1,2} > 6.5, 7.5$ GeV^2 and $-3.0 < \eta^{jet} < 0.0$, which is identical to the requirements of the all-flavour measurement. Both analyses were conducted in the region of $D^{\star\pm}$ phase space defined by $p_T(D^{\star\pm}) > 3.0$ GeV^2 and $|\eta(D^{\star\pm})| < 1.5$, with $0.2 < y < 0.55$. The cross sections were separated into two subsamples, low $x_\gamma^{\rm OBS}$ ($x_\gamma^{\rm OBS} < 0.75$) and high $x_\gamma^{\rm OBS}$ ($x_\gamma^{\rm OBS} > 0.75$), the ratio of which is sensitive to the effects of photon structure.

The measured ratio of low to high $x_\gamma^{\rm OBS}$ (tables 11.8 - 11.9) has been compared to several leading order models. AROMA and CASCADE which do not explicitly implement a photon PDF and generate the low $x_\gamma^{\rm OBS}$ contribution from parton showering and hadronisation effects failed to describe the data for $Q^2 < 1.0$ GeV^2, where the dominant effects of photon structure are expected. Both models were consistent with the data for $Q^2 > 1.5$ GeV^2 within the large uncertainties of the measurement. The data were also compared to the LO prediction of HERWIG implementing the SaS 2D virtual photon PDF. The prediction when no suppression of the PDF is applied lies consistently above the data across the whole Q^2 region. When the photon PDF is suppressed with Q^2 according to a modified DGLAP evolution approach [28], the predicted ratio is in better agreement with

the data, however lies above the data in the photoproduction region. Removing the contribution from the VMD part of the photon PDF brings the prediction into reasonable agreement with the data, indicating the scale provided by the charm mass may act to suppress the photon structure at low Q^2. This conclusion was supported by a direct comparison of the charm tagged ratio to the all flavours ratio. The ratio shows a steep decline as Q^2 increases, particularly in the region $0.0 < Q^2 < 49.0$ GeV^2, indicating a significant contribution from the heavily suppressed (Q^{-4}) VMD component. For $Q^2 > 49.0$ GeV^2, where the scale provided by the photon virtuality, Q^2, is large, the all flavours ratio exhibits similar behaviour to the charm tagged ratio.

The measured cross sections and the ratio of low to high x_γ^{OBS} cross sections have been compared to the NLO predictions of FMNR and HVQDIS. The photoproduction prediction of FMNR describes the cross sections reasonably well within the large theoretical and statistical uncertainties present, when the scale $\mu^2 = 4m_c^2$ is used however, it does not describe the ratio which lies above the data. Using the scale $\mu^2 = Q^2 + m_c^2$ the predicted cross sections lie below the data, however the ratio is described well. The DIS predictions of HVQDIS give a good description of the measured cross sections. The predicted ratio is roughly flat in DIS and is in reasonable agreement with the data.

More detailed studies of photon structure like effects in charm production are required in photoproduction in order to understand the role of the charm mass in such processes. The photoproduction data presented here favour models which implement a photon PDF suppressed in Q^2, however more details of resolved charm production, particularly at low Q^2 may be needed. Solid conclusions are currently difficult to extract from the DIS data due to the large statistical uncertainties of the measurement. LO and NLO calculations which do not explicitly implement a virtual photon PDF describe the DIS data equally as well as those models which do. A more accurate measurement is required to differentiate between these models.

11.4 Outlook and Future Development

The analyses presented here have given current QCD models at leading order and next-to-leading order a thorough test in kinematic regions where the effect of more than a single physical hard scale is present. Understanding multiscale QCD

is of particular importance for future colliders, such as LHC, where two hadronic objects ($p\overline{p}$) partake in the hard interaction. The results presented here give clear insights into the nature of such interactions, in this case with the photon acting as a source of partons. However in the charm production measurement more statistics and better tagging of charmed mesons are required in DIS to understand more fully the role of the charm quark in such interactions.
At time of writing strong progress had been made in the HERA II heavy flavour program [111]. It is envisaged in the future that greater statistics and use of the Micro Vertex Detector (MVD) will vastly reduce the statistical uncertainties on the measurement presented here.

Q^2 bin (GeV^2)	$d\sigma/dQ^2$	Δ_{stat}	Δ_{syst}	Δ_{ES}	($\mathrm{pb}/\mathrm{GeV}^2$)
0, 1	311.4	± 17.4	$^{+37.863}_{-5.691}$	$^{+36.75}_{-52.87}$	
1.5, 4.5	6.223	± 2.12	$^{+0.513}_{-1.22}$	$^{+0.825}_{-1.14}$	
4.5, 10.5	1.401	± 0.406	$^{+0.479}_{-0.205}$	$^{+0.169}_{-0.263}$	
10.5, 49	0.464539	± 0.0996	$^{+0.0886}_{-0.0725}$	$^{+0.0462}_{-0.0757}$	
49, 5000	0.00130432	± 0.0008613	$^{+0.000244}_{-0.000548}$	$^{+0.0000796}_{-0.0000848}$	

Table 11.2: *Measured dijet cross-sections $d\sigma/dQ^2$ in the laboratory frame for events with an associated $\mathrm{D}^{\star\pm}(2010)$ meson for $x_\gamma^{\mathrm{OBS}} < 0.75$. The statistical, systematic and jet energy scale, Δ_{ES}, uncertainties are shown separately.*

Q^2 bin (GeV^2)	$d\sigma/dQ^2$	Δ_{stat}	Δ_{syst}	Δ_{ES}	($\mathrm{pb}/\mathrm{GeV}^2$)
0, 1	510.192	± 21.3	$^{+27.90}_{-61.68}$	$^{+37.98}_{-51.45}$	
1.5, 4.5	12.5261	± 2.9	$^{+1.874}_{-1.780}$	$^{+0.964}_{-1.26}$	
4.5, 10.5	3.39492	± 0.704	$^{+0.301}_{-0.421}$	$^{+0.261}_{-0.361}$	
10.5, 49	0.753599	± 0.140	$^{+0.0702}_{-0.0534}$	$^{+0.0.0648}_{-0.0788}$	
49, 5000	0.00671709	± 0.00188557	$^{+0.000219}_{-0.000895}$	$^{+0.000177}_{-0.000333}$	

Table 11.3: *Measured dijet cross-sections $d\sigma/dQ^2$ in the laboratory frame for events with an associated $\mathrm{D}^{\star\pm}(2010)$ meson for $x_\gamma^{\mathrm{OBS}} > 0.75$. The statistical, systematic and jet energy scale, Δ_{ES}, uncertainties are shown separately.*

Q^2 bin (GeV^2)	$d\sigma/dQ^2$	Δ_{stat}	Δ_{syst}	Δ_{ES}	($\mathrm{pb/GeV}^2$)
0, 1	821.617	$\pm$27.512	$^{+47.032}_{-61.942}$	$^{+74.782}_{-104.488}$	
1.5, 4.5	18.749	$\pm$3.400	$^{+1.943}_{-2.158}$	$^{+1.789}_{-2.399}$	
4.5, 10.5	4.796	$\pm$0.812	$^{+0.566}_{-0.468}$	$^{+0.430}_{-0.624}$	
10.5, 49	1.218	$\pm$0.172	$^{+0.1130}_{-0.0900}$	$^{+0.155}_{-0.111}$	
49, 5000	0.00802	$\pm$0.00207	$^{+0.000328}_{-0.00105}$	$^{+0.000418}_{-0.000256}$	

Table 11.4: *Measured dijet cross-sections $d\sigma/dQ^2$ in the laboratory frame for events with an associated $\mathrm{D}^{\star\pm}(2010)$ meson for $0.0 < x_\gamma^{\mathrm{OBS}} < 1.0$. The statistical, systematic and jet energy scale, Δ_{ES}, uncertainties are shown separately.*

Q^2 bin (GeV^2)	$d\sigma/dQ^2$	Δ_{stat}	Δ_{syst}	Δ_{ES}	($\mathrm{pb/GeV}^2$)
0, 1	287.407	$\pm$16.381	$^{+18.125}_{-16.242}$	$^{+26.159}_{-36.551}$	
1.5, 4.5	5.66727	$\pm$2.014	$^{+0.490}_{-1.193}$	$^{+0.541}_{-0.725}$	
4.5, 10.5	1.50451	$\pm$0.4288	$^{+0.511}_{-0.175}$	$^{+0.135}_{-0.196}$	
10.5, 49	0.452556	$\pm$0.0972	$^{+0.0650}_{-0.0227}$	$^{+0.0413}_{-0.0576}$	
49, 5000	0.00165009	$\pm$0.000894	$^{+0.000367}_{-0.000844}$	$^{+0.0000528}_{-0.0000859}$	

Table 11.5: *Measured dijet cross-sections $d\sigma/dQ^2$ in the photon-proton centre of mass frame for events with an associated $\mathrm{D}^{\star\pm}(2010)$ meson for $x_\gamma^{\mathrm{OBS}} < 0.75$. The statistical, systematic and jet energy scale, Δ_{ES}, uncertainties are shown separately.*

Q^2 bin (GeV^2)	$d\sigma/dQ^2$	Δ_{stat}	Δ_{syst}	Δ_{ES}	($\mathrm{pb/GeV}^2$)
0, 1	489.801	$\pm$20.65	$^{+38.3805}_{-6.1945}$	$^{+44.581}_{-62.29}$	
1.5, 4.5	12.9569	$\pm$2.914	$^{+2.883}_{-1.710}$	$^{+1.237}_{-1.658}$	
4.5, 10.5	3.52203	$\pm$0.721	$^{+0.451}_{-0.369}$	$^{+0.315}_{-0.459}$	
10.5, 49	0.74057	$\pm$0.142	$^{+0.0526}_{-0.0436}$	$^{+0.0.0675}_{-0.0943}$	
49, 5000	0.0049496	$\pm$0.00167	$^{+0.000386}_{-0.00130}$	$^{+0.000159}_{-0.000258}$	

Table 11.6: *Measured dijet cross-sections $d\sigma/dQ^2$ in the photon-proton centre of mass frame for events with an associated $\mathrm{D}^{\star\pm}(2010)$ meson for $x_\gamma^{\mathrm{OBS}} > 0.75$. The statistical, systematic and jet energy scale, Δ_{ES}, uncertainties are shown separately.*

Q^2 bin (GeV^2)	$d\sigma/dQ^2$	Δ_{stat}	Δ_{syst}	Δ_{ES}	($\mathrm{pb/GeV}^2$)
0, 1	777.21	$\pm$26.355	$^{+42.445}_{-17.383}$	$^{+70.74}_{-98.84}$	
1.5, 4.5	18.624	$\pm$3.542	$^{+2.924}_{-2.085}$	$^{+2.383}_{-1.778}$	
4.5, 10.5	5.027	$\pm$0.839	$^{+0.682}_{-0.408}$	$^{+0.451}_{-0.655}$	
10.5, 49	1.193	$\pm$0.172	$^{+0.0836}_{-0.0492}$	$^{+0.109}_{-0.152}$	
49, 5000	0.00660	$\pm$0.00189	$^{+0.000533}_{-0.00155}$	$^{+0.000211}_{-0.000344}$	

Table 11.7: *Measured dijet cross-sections $d\sigma/dQ^2$ in the photon-proton centre of mass frame for events with an associated $\mathrm{D}^{\star\pm}(2010)$ meson for $0.0 < x_\gamma^{\mathrm{OBS}} < 1.0$. The statistical, systematic and jet energy scale, Δ_{ES}, uncertainties are shown separately.*

Q^2 bin (GeV^2)	R	Δ_{stat}	Δ_{syst}	Δ_{ES}	($\mathrm{pb/GeV}^2$)
0, 1	0.6104	$\pm$0.0482	$^{+0.0338746}_{-0.0548105}$	$^{+0.0385}_{-0.0288}$	
1.5, 4.5	0.4968	$\pm$0.239	$^{+0.186684}_{-0.0860125}$	$^{+0.0372}_{-0.0299}$	
4.5, 10.5	0.4126	$\pm$0.169	$^{+0.0414597}_{-0.159011}$	$^{+0.0305}_{-0.0195}$	
10.5, 49	0.616	$\pm$0.187	$^{+0.0893771}_{-0.149159}$	$^{+0.0320}_{-0.00901}$	
49, 5000	0.194	$\pm$0.181	$^{+0.090592}_{-0.0477748}$	$^{+0.00287}_{-0.00691}$	

Table 11.8: *Measured ratio $R = \sigma(x_\gamma^{\mathrm{OBS}} < 0.75)/\sigma(x_\gamma^{\mathrm{OBS}} > 0.75)$ as a function of Q^2 for dijet events with an associated $\mathrm{D}^{\star\pm}(2010)$ meson in the laboratory frame.*

Q^2 bin (GeV^2)	R	Δ_{stat}	Δ_{syst}	Δ_{ES}	($\mathrm{pb/GeV}^2$)
0, 1	0.5868	$\pm$0.0473	$^{+0.0206}_{-0.0484}$	$^{+0.0370}_{-0.0277}$	
1.5, 4.5	0.4374	$\pm$0.220	$^{+0.175}_{-0.0609}$	$^{+0.0328}_{-0.0263}$	
4.5, 10.5	0.424	$\pm$0.171	$^{+0.0695}_{-0.168}$	$^{+0.0313}_{-0.0200}$	
10.5, 49	0.666	$\pm$0.202	$^{+0.0617}_{-0.162}$	$^{+0.0346}_{-0.00972}$	
49, 5000	0.351	$\pm$0.269	$^{+0.115}_{-0.0876}$	$^{+0.00517}_{-0.012}$	

Table 11.9: *Measured ratio $R = \sigma(x_\gamma^{\mathrm{OBS}} < 0.75)/\sigma(x_\gamma^{\mathrm{OBS}} > 0.75)$ as a function of Q^2 for dijet events with an associated $\mathrm{D}^{\star\pm}(2010)$ meson in the photon-proton centre of mass frame.*

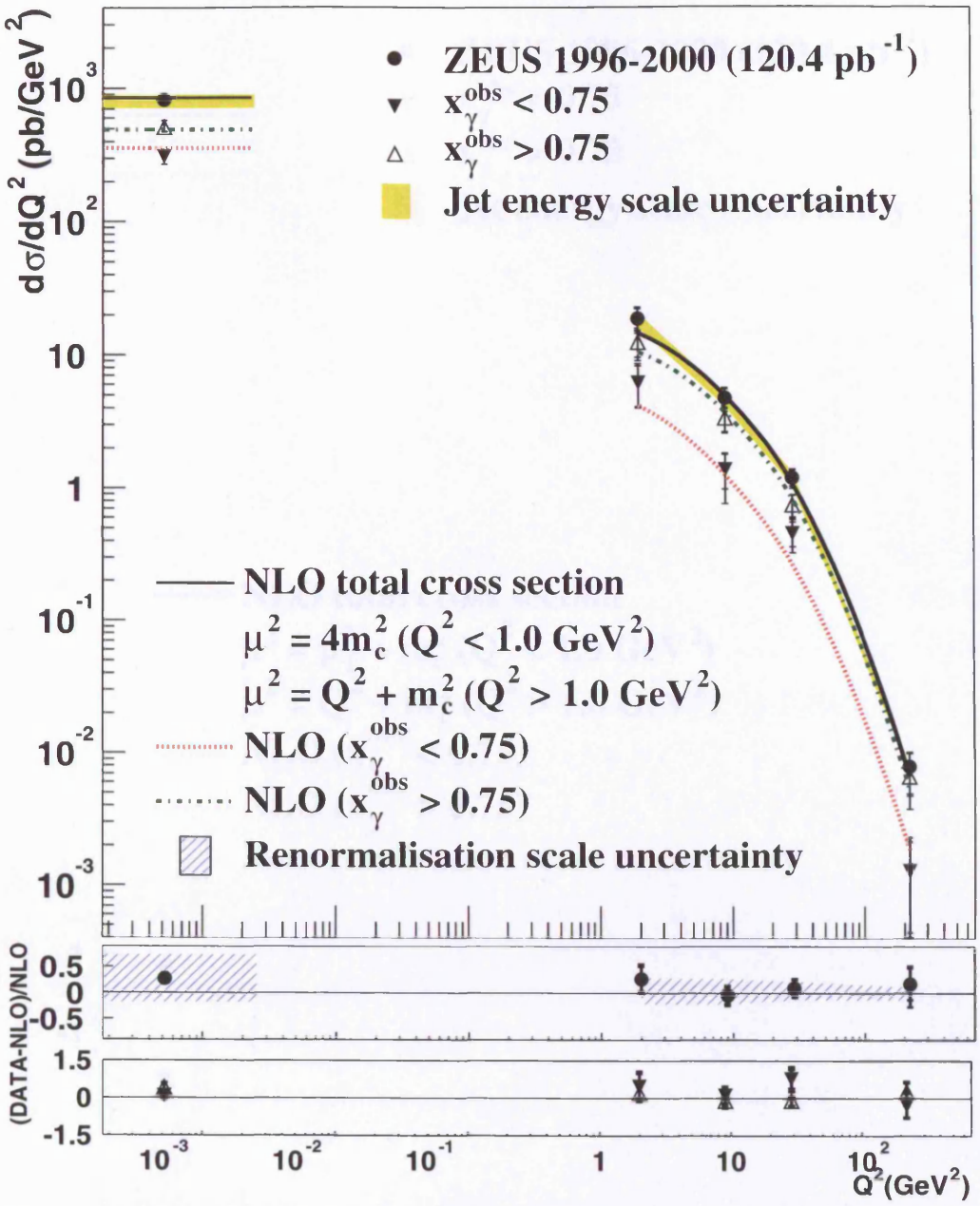

Figure 11.6: *Measured dijet cross-sections $d\sigma/dQ^2$ for $x_\gamma^{\mathrm{OBS}} > 0.75$ (upwards triangles) $d\sigma/dQ^2$ for $x_\gamma^{\mathrm{OBS}} < 0.75$ (downwards triangles) and $d\sigma/dQ^2$ for the whole x_γ^{OBS} region (black dots), for events with an associated $\mathrm{D}^{\star\pm}(2010)$ meson in the laboratory frame (top). The inner vertical bars represent the statistical uncertainties of the data, and the outer bars show the statistical and systematic uncertainties added in quadrature, except for that associated with the uncertainty in the absolute energy scale of the jets (shaded band). The NLO QCD calculations of FMNR (photoproduction) $(\mu^2 = 4m_c^2)$ and HVQDIS $(\mu^2 = Q^2 + m_c^2)$ are shown for each of the cross-sections. The relative difference of the measured cross sections to the NLO predictions are shown (middle) along with the theoretical uncertainty on the calculation (hatched band). The relative difference of the low and high x_γ^{OBS} measurements to the NLO predictions are also shown (bottom).*

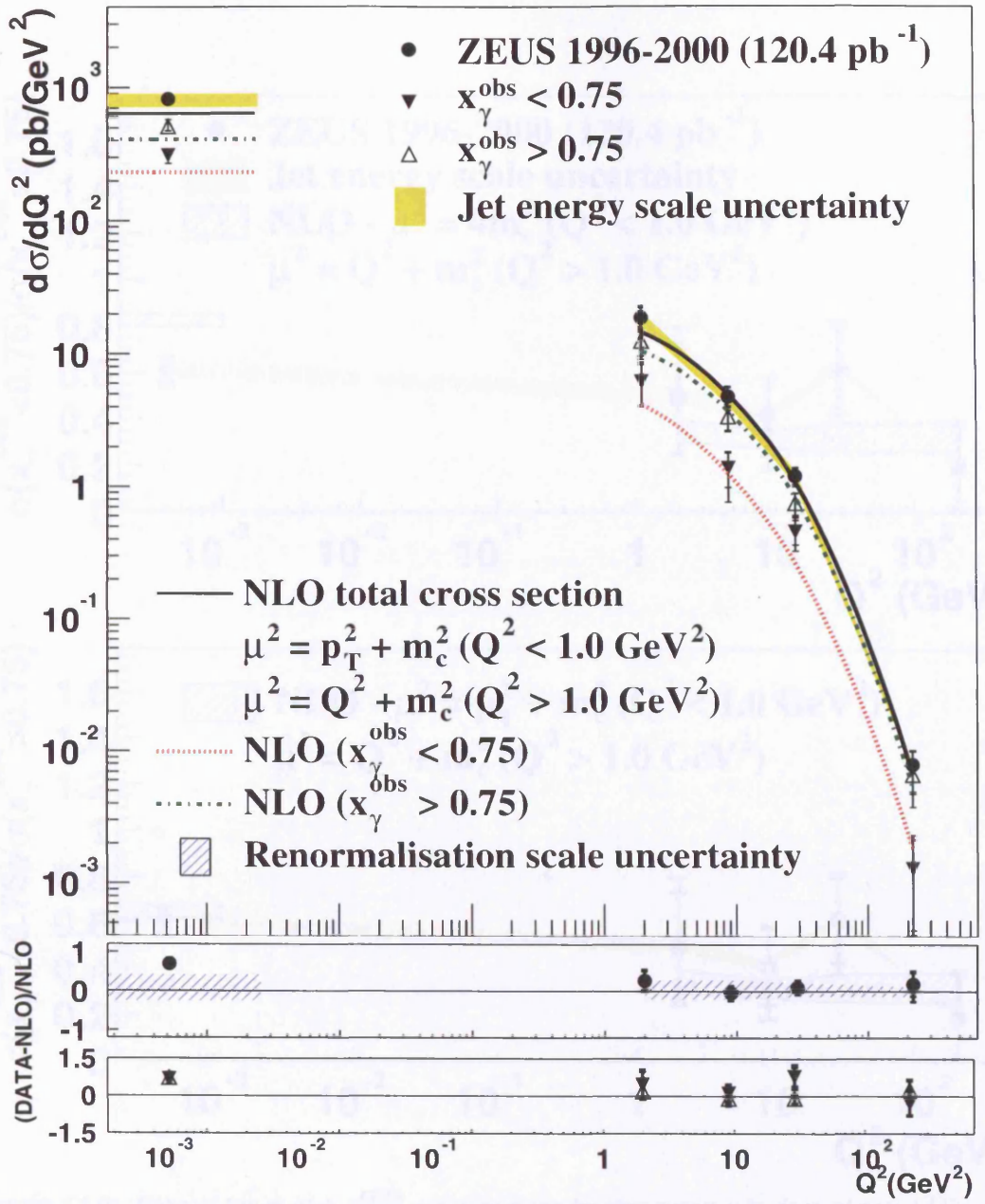

Figure 11.7: *Measured dijet cross-sections $d\sigma/dQ^2$ for $x_\gamma^{\mathrm{OBS}} > 0.75$ (upwards triangles) $d\sigma/dQ^2$ for $x_\gamma^{\mathrm{OBS}} < 0.75$ (downwards triangles) and $d\sigma/dQ^2$ for the whole x_γ^{OBS} region (black dots), for events with an associated $\mathrm{D}^{\star\pm}(2010)$ meson in the laboratory frame (top). The inner vertical bars represent the statistical uncertainties of the data, and the outer bars show the statistical and systematic uncertainties added in quadrature, except for that associated with the uncertainty in the absolute energy scale of the jets (shaded band). The NLO QCD calculations of FMNR (photoproduction) $(\mu^2 = p_T^2 + m_c^2)$ and HVQDIS $(\mu^2 = Q^2 + m_c^2)$ are shown for each of the cross-sections. The relative difference of the measured cross sections to the NLO predictions are shown (middle) along with the theoretical uncertainty on the calculation (hatched band). The relative difference of the low and high x_γ^{OBS} measurements to the NLO predictions are also shown (bottom).*

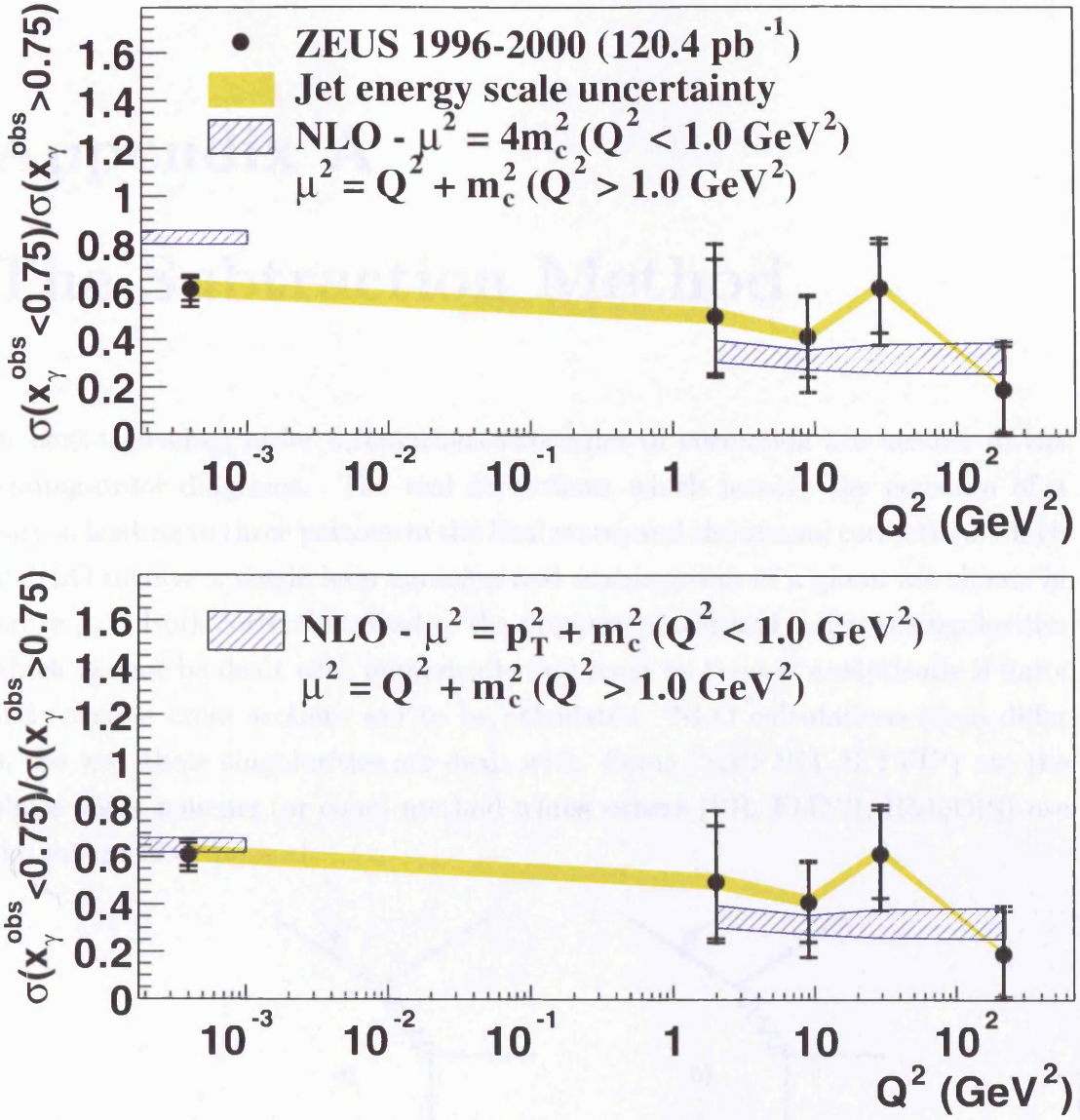

Figure 11.8: *Ratio of low to high x_γ^{OBS} cross sections for dijet events with an associated D^* in the laboratory frame (dots) compared to the NLO QCD calculations of FMNR (photoproduction) and HVQDIS (DIS). The inner vertical bars represent the statistical uncertainties on the data, and the outer bars show the statistical and systematic uncertainties added in quadrature, except for that associated with the uncertainty in the absolute energy scale of the jets (shaded band). The renormalisation and factorisation scale used were $\mu^2 = Q^2 + m_c^2$ in HVQDIS and either $\mu^2 = 4m_c^2$ (top) or $\mu^2 = p_T^2 + m_c^2$ (bottom) in FMNR. The hatched band represents the theoretical uncertainty on the calculations.*

Appendix A

The Subtraction Method

In next-to-leading order calculations two types of correction are needed to the leading-order diagrams. The real corrections which involve the emission of a parton leading to three partons in the final state, and the virtual corrections which at NLO involve a single loop emission and reabsorption of a gluon are shown in figure A.1. Both corrections lead to the presence of soft and collinear singularities which cannot be dealt with numerically and must be treated analytically if finite and sensible cross sections are to be calculated. NLO calculations often differ in the way these singularities are dealt with. Some (MEPJET,JETVIP) use the phase space splicing (or cone) method whilst others (FR, FMNR, HVQDIS) use the subtraction method.

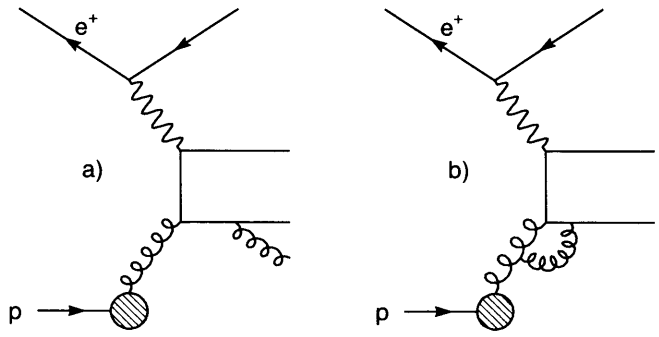

Figure A.1: *Examples of NLO QCD real (a) and virtual (b) corrections to the LO Feynmann diagrams.*

The phase space splicing method applies one or more cutoff parameters to separate regions of phase space which contain singularities from those that do not. The singular regions are then calculated analytically, and the remaining regions are integrated over numerically. The total phase space is then added together

such that all dependence on the unphysical cutoff parameters is removed. In practice this is achieved by choosing suitably small cutoff values, such that the final calculated cross sections have little dependence upon them. Several different approaches, using a variety of cutoff variables have been proposed [107–109].
The subtraction method takes as a start point the definition of the next-to-leading order cross section in terms of the two corrections to the leading-order Feynmann diagrams,

$$\sigma^{NLO} = \int_n d\sigma^{real} + \int_n d\sigma^{virt} \tag{A.1}$$

where σ^{real} and σ^{virt} are the cross sections for the real and virtual corrections and n is the number of partons in the final state (n=3 for real and n=2 for virtual correction).
A fake cross section, σ^A, is then added and subtracted from the above integral,

$$\sigma^{NLO} = \int_n d\sigma^{real} - d\sigma^A + \int_n d(\sigma^{virt} + \int_1 d\sigma^A) \tag{A.2}$$

where σ^A is chosen to have the same singularity structure as σ^{real}, in such a way that σ^{NLO} can be integrated over numerically, to give a finite cross-section. The cross section $d\sigma^A$ can be calculated from the dipole formalism, the details of which can be found in [110].

Appendix B

Error Analysis

B.1 Acceptance Corrections

The purity, P, efficiciency, E, and correction factor, C, defined in section 9.4 were defined in terms of the number of Monte Carlo simulated events detected in a given bin of Q^2 and x_γ^{OBS} (t), the number generated in a given bin (m) and the number both detected and generated in a given bin (u). The uncertainties on these quantities are not independent but correlated, and in order to calculate the errors on these quantities it is useful to redifine them in terms of the uncorrelated quantities a, b and c such that,

$$\#\ generated\ in\ bin = t = a + b\ ; \tag{B.1}$$

$$\#\ detected\ in\ bin = m = a + c\ ; \tag{B.2}$$

$$\#\ generated\ and\ detected\ in\ bin = u = a\ ; \tag{B.3}$$

where a is the number of events generated and detected in a given bin, b is the number of events generated in a bin but not detected in it, and c is the number of events detected in the bin but not generated in it. P, E and C can then be redifined,

$$P = \frac{a}{a+c} \tag{B.4}$$

$$E = \frac{a}{a+b} \tag{B.5}$$

$$C = \frac{a+b}{a+c} \tag{B.6}$$

The error on the purity can then be derived given the variance of the quantities a and c, V_a and V_c,

$$\begin{aligned}\delta P &= \left(\frac{\delta P}{\delta a}\right)^2 .V_a + \left(\frac{\delta P}{\delta c}\right)^2 .V_c \\ &= \left[\frac{1}{a+c} - \frac{a}{(a+c)^2}\right]^2 .V_a + \left[\frac{a}{(a+c)^2}\right]^2 .V_c \\ &= \frac{c^2.V_a^2 + a^2.V_c}{(a+c)^4}\end{aligned}$$

This can then be rewritten in terms of the initial qunatities t,m and u to give,

$$\delta P = \sqrt{\frac{m^2.V_u + u^2.V_m - 2.m.u.V_u}{m^2}} \tag{B.7}$$

where for the weighted events used for acceptence corrections in this thesis the variance is given by the sum of all weights squared $\sum w^2$.
The error on the efficiency, E and correction factor, C can be calculated using the same technique. The exact details are not given here, however the uncertainties are quoted as,

$$\delta E = \sqrt{\frac{t^2.V_u + u^2.V_t - 2.t.u.V_u}{t^4}} \tag{B.8}$$

$$\delta C = \sqrt{\frac{m^2.V_t + t^2.V_m - 2.m.t.V_u}{m^4}} \tag{B.9}$$

Bibliography

[1] ZEUS Collaboration,*A detector for HERA*,PRC 87-02
ZEUS Collaboration,*The ZEUS Detector*, DESY Status Report, (1993).

[2] N. Harnew et al., Nucl. Inst. Meth. **A 279**, 290 (1989);
B. Foster et al., Nucl. Phys. Proc. Suppl. **B 32**, 181 (1993);
B. Foster et al., Nucl. Inst. Meth. **A 338**, 254 (1994)

[3] R. Hall-Wilton et al., *The CTD Tracking Resolution* (unpublished).
ZEUS-99-024, (1999).

[4] M. Derrick et al., Nucl. Inst. Meth. **A 309**, 77 (1991);
A. Andersen et al., Nucl. Inst. Meth. **A 309**, 101 (1991);
A. Caldwell et al., Nucl. Inst. Meth. **A 321**, 356 (1992);
A. Bernstein et al., Nucl. Inst. Meth. **A 336**, 23 (1993).

[5] A. Bamberger et al., Nucl. Inst. Meth. **A 382**, 419 (1996).

[6] A. Bamberger et al., Nucl. Inst. Meth. **A 401**, 63 (1997).

[7] J. Andruszkow et al., *First measurement of HERA luminosity by ZEUS lumi monitor*, Preprint DESY-92-066, DESY, (1992);
ZEUS Coll., M. Derrick et al., Z. Phys **C 63**, 391 (1994);
J. Andruszkow et al., Acta Phys. Pol. **B32**, 2025 (2001).

[8] ZEUS Coll., R. Carlin et al., Nucl. Inst. Meth. **A 379**, 542 (1996).

[9] Proceeding of the workshop on 'Future Physics at HERA', eds. G. Inglemann, A. De Roeck and R. Klanner, DESY 1996.

[10] ZEUS Coll., *A Straw-Tube Tracker for ZEUS* (unpublished). ZEUS-98-046.

[11] ZEUS Coll., *A Microvertex Detector for ZEUS* (unpublished). ZEUS-97-006;
The ZEUS MVD Group, *Mechanical Design and Construction of the ZEUS Micro Vertex Detector* (unpublished). ZEUS-00-028;
D. Daneheim, *The silicon Strip Detectors of the ZEUS Microvertex Detector*, Diploma Thesis, DESY, 1999.

[12] B. J. West, *Charm and the Virtual Photon at HERA and a Global Tracking Trigger for ZEUS*, PhD. thesis, UCL (2001).

[13] A. Quadt, *Running Modes of the CTD-SLT and their impact on a Global Tracking SLT* (unpublished). ZEUS-97-077.

[14] R. P. Feynman, Phys. Rev. Lett. **23**, 1415 (1969).

[15] H. E. Frisk and F. Sciulli, Ann. Rev. Nucl. Part. Sci. **32**, 499 (1982).

[16] T. Eichten et al., Phys. Lett. **B 46**, 274 (1973).

[17] Tasso Coll., R. Brandelik et al., Phys. Lett. **B86**, 243 (1979).

[18] ZEUS Coll., J. Breitweg et al., *Measurement of the neutral current cross section and F_2 structure function for deep inelastic e^+p scattering at HERA*, Eur. Phys. J.C (2001).

[19] J. C. Collins, D. E. Soper and G. Sterman, Nucl. Phys. **B 261**, 104 (1985).

[20] V. N. Gribov and L. N. Lipatov, Sov. J. Nucl. Phys. **15**, 438 (1972);
Yu. L. Dokshitzer, Sov. Phys. JETP **46**, 641 (1977);
G. Altarelli and G. Parisi, Nucl. Phys. **B126**, 298 (1977).

[21] I. I. Balitsky and L. N. Lipatov, Sov. J. Nucl. Phys. **28**, 822 (1978);
E. A. Kuraev, L.N. Lipatov and V. S. Fadin, Sov. Phys. JETP **44**, 443 (1976).

[22] M. Ciafaloni, Nucl. Phys. **B 296**, 49 (1988);
S. Catani, F. Fiorani and G. Marchesini, Nucl. Phys. **B 336**, 18 (1990).

[23] C. F. von Weizsacker, Z. Phys. **88**, 612 (1934);
E.J. Williams, Phys. Rev. **45**, 729 (1934).

[24] ZEUS Coll., J Breitweg et al., Eur. Phys. J. **C 1**, 109 (1998).

[25] JADE Coll., W. Bartel et al.., Z. Phys. **C 24** (1984);
TASSO Coll., M. Althoff et al.., Z. Phys. **C 31** (1986);
TPC/Two-Gamma Coll., H. Aihara et al., Z. Phys. **C 34** (1987);
L3 Coll., M. Acciarri et al., Phys. Lett. **B 436** (1998);
ALEPH Coll., R. Barate et al., Comp. Phys. Comm. **B458** (1999);
L3 Coll., M. Acciarri et al., Phys. Lett. **B 447** (1999);
L3 Coll., M. Acciarri et al., Phys. Lett. **B 453** (1999).

[26] R.J. De Witt, L. M. Jones, J. D. Sullivan, D. E. Willen, H. W. Wyld, Phys. Rev. **D 19**, 2046 (1979).

[27] G. A. Schuler and T. Sjöstrand, Z. Phys. **C 68**, 607 (1995).

[28] G. A. Schuler and T. Sjöstrand, Phys. Lett. **B 376**, 193 (1996).

[29] M. H. Seymour, *Jets in QCD*, hep-ph/9506421, CERN-TH/95-176 (1995).

[30] P. de Jong, *Status of Uranium Calorimeter Reconstruction Software*, ZEUS Note 92-19 (1992);
M. De Kamps, *Gluon Momentum Fraction Measurements in the ZEUS Detector*, ZEUS Note 94-14.

[31] A. Savin, *Study of Calorimeter Noise in the 1996 data* (unpublished), ZEUS-98-007

[32] G. Briskin and A. Caldwell, *Comparison of CAL Energy for Electrons with CTD*, ZEUS Note 95-35;
M. Vreeswijk, Ph. D Thesis, University of Amsterdam (1996).

[33] R. Saunders, *A Measurement of Dijet Photoproduction at HERA using the ZEUS Detector.* Ph. D. Thesis, UCL (1997).

[34] J. Repond, *Jet Energy Corrections* (Unpublished). ZEUS-96-104.

[35] M. Wodarczyk, *Measurement of the* F_2 *Structure Function of the Proton at HERA from 1996 and 1997 ZEUS Data.*, PhD Thesis, Wisconsin, (1999).

[36] G. M. Briskin, Ph. D. Thesis, Tel Aviv University (1998).

[37] N. Tuning, *ZUFOs: Hadronic final state reconstruction with calorimeter, tracking and backsplash correction*, ZEUS Note 01-021 (2001).

[38] F. Abe et al, Phys. Rev. **D45**, 1448 (1992).

[39] F. Sciulli, B. Straub and L. Wai, ZEUS Note 95-140.

[40] P. J. Bussey, EUCELL, ZEUS PHANTOM Users Library.

[41] S. Catani, Yu. L. Dokshitzer and B. R. Webber, Phys. Lett. **B285** (1992) 291.
S. Catani, Yu. L. Dokshitzer and M. H. Seymour, B. R. Webber, Nucl. Phys. **B406** (1993) 187.

[42] M. Seymour, Preprint hep-ph/9707349, (1997).

[43] H. Abramowicz, A. Caldwell, R. Sinkus, *Neural network based electron identification in the ZEUS calorimeter*, Nucl. Inst. Meth., **A365**: 508 517, (1995).

[44] S. Bentvelsen, J. Engelen, P. Kooijman, in *Proc. Workshop on Physics at HERA*, Vol. 1, edited by W. Buchmüller, G. Ingelman (Proceedings of the Workshop, Hamburg 1991), p.23,
S. P. Baranov et al., in *Proc. Workshop on Physics at HERA*, Vol. 3, p1478, edited by W. Buchmüller, G. Ingelman (Proceedings of the Workshop, Hamburg 1991), p.23.

[45] F. Jacquet and A. Blondel, *proceedings of the study of an ep facility for Europe*, ed. U. Amaldi, DESY 79-48 p.391.

[46] R. Hagedorn, *Relativistic Kinematics*, W. A. Benjamin inc (1964).

[47] S.D. Ellis and D.E. Soper, Phys. Rev. **D 48**,3160 (1993).

[48] B. Pötter. *jetvip 2.1*, hep-ph/9911221.
S. Frixione, G. Ridolfi. Nucl. Phys. **B 507** 315 (1997).
M. Klassen, G. Kramer. Phys. Lett. **B 366** 385 (1996).

[49] R. Brun et al., GEANT3, Technical Report CERN-DD/EE/84-1, CERN (1987).

[50] G. Marchesini et al., HERWIG: *A monte carlo event generator for simulating hadron emission reactions with iterfering gluons.* Comp. Phys. Comm. **67**, 465 (1992).

[51] T. Sjöstrand, *High-energy physics event generation with* PYTHIA 5.7 *and* JETSET 7.4. COMP. Phys. Comm. **82**, 74 (1994).

[52] M. Glück, E. Reya and A. Vogt, *Photonic parton distributions.* Phys. Rev. **D 46**, 1973 (1992).

[53] A.D. Martin, R.G. Roberts and W.J. Stirling, *Parton distributions of the proton.* Phys. Rev. **D 50**, 6734 (1994).

[54] B.R. Webber, Nucl. Phys. **B 238**, 192 (1984).

[55] A. Anderson et al., *Parton fragmentation and string dynamics* Phys. Rep. **97**, 31 (1983).

[56] T. Sjöstrand, *The Lund Monte Carlo for jet fragmentation and* e^+e^- *physics:* JETSET Version 6.2. Comp. Phys. Comm. **39**, 347 (1986).

[57] T. Sjöstrand and M. Bengtsson, *The Lund Monte Carlo for jet fragmentation and* e^+e^- *physics:* JETSET *version 6.3: and update.* Comp. Phys. Comm. **43**, 367 (1987).

[58] T. Sjöstrand and M. van Zijl, Phys. Rev. **D36**, 2019 (1987).

[59] J. M. Butterworth, J. R. Forshaw and M. H. Seymour, Z. Phys. **C 72**, 637 (1996).

[60] G. A. Schuler and T. Sjöstrand, Phys. Lett. **B 300** (1993) 169.

[61] G. Corcella, I. G. Knowles, G. Marchesini, S. Moretti, K. Odagiri, P. Richardson, M.H. Seymour and B. R. Webber, *HERWIG 6.5.* JHEP 0101, 010 (2001), hep-ph/0011363, hep-ph/0210213.

[62] J.M. Butterworth and S. Butterworth, *Jetweb: A www interface and database for monte carlo tuning and validation.* **http://jetweb.hep.ucl.ac.uk**, Comp. Phys. Comm. **153/2**, 164 (2003), *(fit no. 692).*

[63] S. Frixione, Z. Kunszt and A. Signer, *Three jet cross sections to next-to-leading order.* Nucl. Phys. **B 467**, 399 (1996);
S. Frixione, *A general approach to jet cross-sections in QCD.* Nucl. Phys. **B 507**, 295 (1997).

[64] S. Frixione and G. Ridfolfi, *Jet photoproduction at HERA.* Nucl. Phys. **B 507**, 315 (1997).

[65] B.W. Harris and J.F. Owens, *Photoproduction of jets at HERA in next-to-leading order QCD.* Phys. Rev. **D 56**, 4007 (1997).

[66] B.W. Harris and J.F. Owens, *Jet photoproduction and the structure of the photon.* Phys. Rev. **D 57**, 5555 (1998).

[67] M. Klassen and G. Kramer, *Inclusive two-jet production at HERA: Direct and resolved cross sections in next-to-leading order QCD.* Z. Phys. **C 76**, 67 (1997).

[68] M. Klassen, T. Kleinwort and G. Kramer, *Inclusive jet production in γp and $\gamma\gamma$ processes: Direct and resolved photon cross sections in next-to-leading order QCD.* Eur. Phys. J. direct **C1**, 1 (1998).

[69] P. Aurenche et al., *NLO Monte Carlo approach in 1 or 2 jet photoproduction.* Eur. Phys. J. **C 17**, 413 (2000).

[70] B.W. Harris, M. Klassen and J. Vossebeld, *Detailed comparison of next-to-leading order predictions for jet photoproduction at HERA, Proc. Workshop on Monte Carlo Generators for HERA physics,* T.A. Doyle et al. (ed.), p. 171. DESY, Hamburg, Germany (1999). Also in preprint DESY-PROC-1999-02 (hep-ph/9905348), available on **http://www.desy.de/ heramc/**.

[71] R.K. Ellis, D.A. Ross and A.E. Terrano, *The perturbative calculation of jet structure in e^+e^- annihilation.* Nucl. Phys. **B 178**, 421 (1981).

[72] D. Graudenz, *Disaster++ version 1.0,* Preprint hep-ph/9710244, 1997.

[73] S. Catani and M.H. Seymour, *A general algorithm for calculating jet cross-sections in NLO QCD.* Nucl. Phys. **B 485**, 291 (1997).

[74] H. Lai et al., *Improved parton distributions from global analysis of recent deep inelastic scattering and inclusive jet data.* Phys. Rev. **D 55**, 1280 (1997).

[75] G. Ingelman, *et. al.* "Future physics at HERA. Proceedings, Workshop, Hamburg, Germany, September 25, 1995-May 31, 1996. Vol. 1, 2," DESY-96-235

[76] J. Breitweg *et al.* , "Measurement of open beauty production in photoproduction at HERA," Eur. Phys. J. C **18** (2001) 625 [arXiv:hep-ex/0011081]. C. Adloff *et al.*, "Measurement of open beauty production at HERA," Phys. Lett. B **467** (1999) 156 [Erratum-ibid. B **518** (2001) 331]

[77] S. Chekanov *et al.* , "Dijet angular distributions in photoproduction of charm at HERA," Phys. Lett. B **565** (2003) 87

[78] R. K. Ellis, P. Nason, Nucl. Phys., **B312** (1989) 551.

[79] S. Dawson, P. Nason, Nucl. Phys., **B303** (1988) 607.

[80] S. Frixione et al., Phys. Lett., **B348** (1995) 633.
S. Frixione et al., Nucl. Phys., **B454** (1995) 3.

[81] B.A. Kneihl et al., Zeits. f. Phys. **C76** (1997) 677.
J. Binnewies et al., DESY 97-241, hep-ph/9712482, Phys. Rev. D (1998).

[82] J. Binnewies et al., Zeits. f. Phys. **C76** (1997) 677.

[83] M. Cacciari, M. Greco, Phys. Rev., **D55** (1997) 7134.
M. Cacciari, M. Greco, S. Rolli, A. Tanzini, Phys. Rev. **D55** (1997) 2736.

[84] M. Aivazis, J. C. Collins, F. I. Olness, and W. Tung, Phys. Rev. **D50**, 3102 (1994), hep-ph/9312319.

[85] S. Frixione et al., "Heavy Quark Productions", hep-ph/9702287.

[86] G. Bellini, Proc. of Les Rencontres de Physique de la vallee d'Acoste, La Thuille, 1994.

[87] E691 Collab., J. C. Anjos et al., Phys. Rev. Lett., **62** (1989) 513.
E691 Collab., J. C. Anjos et al., Phys. Rev. Lett., **65** (1990) 2503.

[88] E. M. Levin, A. D. Martin, M.G. Ryskin, T, Teubner Zeits. f. Phys. **C74**, 671-685 (1997).

[89] S. Chekanov *et al.*, "Measurement of D*+- production in deep inelastic e+-p scattering at HERA," Phys. Rev. D **69** (2004) 012004.

[90] B.W. Harris and J. Smith, Phys. Rev., **D 57**, 2806 (1998).

[91] M. Cacciari, S. Frixione and P. Nason, JHEP **0103** 006 (2001).

[92] J. Breitweg *et al.*, "Measurement of inclusive D*+- and associated dijet cross sections in photoproduction at HERA," Eur. Phys. J. C **6** (1999) 67.

[93] S. Nussinov, Phys. Rev. Lett. **35**, 1672 (1975).
G.J. Feldman et al., Phys. Rev. Lett., **38** (1977) 1313.

[94] EMC Collaboration, M. Arneodo et. al., Z. Phys. **C 32**, (1986) 1.

[95] P. A. Nylander, ZEUS Coll., *A Systematic Method for Unbinned Fitting and Statistical Analysis*, (unpublished). ZEUS-97-096.

[96] "Proceedings of DIS04 Workshop", (to be published).

[97] K. Hagiwara *et al.*, "Review Of Particle Physics," Phys. Rev. D **66** (2002) 010001.

[98] G. Ingelman, J. Rathsman and G. A. Schuler, "AROMA 2.2 - A Monte Carlo Generator for Heavy Flavour Events in *ep* Collisions," Comput. Phys. Commun. **101** (1997) 135.

[99] H. Jung, "The CCFM Monte Carlo generator CASCADE," Comput. Phys. Commun. **143** (2002) 100.

[100] S. Frixione, M. Mangano, P. Nason, G. Ridoflfi, Nucl. Phys. **B 412** (1994) 225.

[101] M. Mangano, P. Nason, G. Ridoflfi, Nucl. Phys. **B373**, (1992) 295.

[102] P. Aurenche, J. P. Guillet and M. Fontannaz, Z. Phys. **C 64** (1994) 621.

[103] B. W. Harris and J. Smith, Nucl. Phys. **B 452**, 109 (1995), hep-ph/9503484.

[104] C. Peterson et al., Phys. Rev. **D 27** (1983) 105.

[105] P. Nason and C. Oleari, Phys. Lett. **B 447** (1999) 327.
P. Nason and C. Oleari, Nucl. Phys. **B 565** (2000) 245.

[106] L. Gladilin, Preprint hep-ex/9912064, (1999).

[107] M. Klasen and G. Kramer, Z. Phys. **C72**, 107 (1996).

[108] B.W. Harris, M. Klasen and J. Vossebeld, hep-ph/9905348.

[109] P. Aurenche, L. Bourhis, M. Fontannaz and J.Ph. Guillet, Proceedings of the Workshop "Future Physics at HERA", 570 (1996).

[110] S. Catani and M. H. Seymour, "Jet cross sections at next-to-leading order," Acta Phys. Polon. B **28** (1997) 863.

[111] ZEUS Coll. "Charm Production in DIS Using HERA II data", proceeding from ICHEP04. (unpublished)